

JCMT HARP CO 3-2 Observations of Molecular Outflows in W5

Adam Ginsburg^{1*}, John Bally¹, and Jonathan P. Williams²

¹Center for Astrophysics and Space Astronomy, University of Colorado 389 UCB, Boulder, CO 80309-0389

²Institute for Astronomy University of Hawaii 2680 Woodlawn Dr. Honolulu, HI 96822

1 June 2011

ABSTRACT

New JCMT HARP CO 3-2 observations of the W5 star forming complex are presented, totaling an area of ~ 12000 arcmin 2 with sensitivity better than 0.1 K per 0.4 km s $^{-1}$ channel. We discovered 55 CO outflow candidates, of which 40 are associated with W5 and 15 are more distant than the Perseus arm. Most of the outflows are located on the periphery of the W5 HII region. However, two outflows clusters are > 5 pc from the ionization fronts, indicating that their driving protostars formed without directly being triggered by the O-stars in W5. We compare the derived outflow properties to those in Perseus and find that the total W5 outflow mass is surprisingly low given the cloud masses. The outflow mass deficiency in the more massive W5 cloud ($M(\text{H}_2) \sim 5 \times 10^4 M_\odot$) can be explained if ionizing radiation dissociates molecules as they break out of their host cloud cores. Although CO J=3-2 is a good outflow tracer, it is likely to be a poor mass tracer because of sub-thermal line excitation and high opacity, which may also contribute to the outflow mass discrepancy. It is unlikely that outflows could provide the observed turbulent energy in the W5 molecular clouds even accounting for undetected outflow material. Many cometary globules have been observed with velocity gradients from head to tail, displaying strong interaction with the W5 HII region and exhibiting signs of triggered or revealed star formation in their heads. Because it is observed face-on, W5 is an excellent region to study feedback effects, both positive and negative, of massive stars on star formation.

Key words: ISM: jets and outflows — ISM: kinematics and dynamics — ISM: individual: W5 — stars: formation

1 INTRODUCTION

Galactic-scale shocks such as spiral density waves promote the formation of giant molecular clouds (GMCs) where massive stars, star clusters, and OB associations form. The massive stars in such groups can either disrupt the surrounding medium or promote further star formation. While ionizing and soft UV radiation, stellar winds, and eventually supernova explosions destroy clouds in the immediate vicinity of massive stars, as the resulting bubbles age and decelerate, they can also trigger further star formation. In the “collect and collapse” scenario (e.g. Elmegreen & Lada 1977), gas swept-up by expanding bubbles can collapse into new star-forming clouds. In the “radiation-driven implosion” model (Bertoldi & McKee 1990; Klein et al. 1983), pre-existing clouds may be compressed by photo-ablation pressure or by the increased pressure as they are overrun by an expand-

ing shell. In some circumstances, forming stars are simply exposed as low-density gas is removed by winds and radiation from massive stars. These processes may play significant roles in determining the efficiency of star formation in clustered environments (Elmegreen 1998).

Feedback from low mass stars may also control the shape of the stellar initial mass function in clusters (Adams & Fatuzzo 1996; Peters et al. 2010). Low mass young stars generate high velocity, collimated outflows that contribute to the turbulent support of a gas clump, preventing the clump from forming stars long enough that it is eventually blown away by massive star feedback. It is therefore important to understand the strength of low-mass protostellar feedback relative to other feedback mechanisms.

Outflows are a ubiquitous indicator of the presence of ongoing star formation (Reipurth & Bally 2001). CO outflows are an indicator of ongoing embedded star formation at a younger stage than optical outflows because shielding from the interstellar radiation field is required for CO to

* adam.ginsburg@colorado.edu

survive. Although Herbig-Haro shocks and H₂ knots reveal the locations of the highest-velocity segments of these outflows, CO has typically been thought of as a “calorimeter” measuring the majority of the mass and momentum ejected from protostars or swept up by the ejecta (Bachiller 1996).

The W5 star forming complex in the outer galaxy is a prime location to study massive star formation and triggering. The bright-rimmed clouds in W5 have been recognized as good candidates for ongoing triggering by a number of groups (Lefloch et al. 1997; Thompson et al. 2004; Karr & Martin 2003). The clustering properties were analyzed by Koenig et al. (2008) using Spitzer infrared data, and a number of significant clusters were discovered. The whole W5 complex may be a product of triggering, as it is located on one side of the W4 chimney thought to be created by multiple supernovae during the last \sim 10 MYr (Oey et al. 2005, Figure 1).

Following Koenig et al. (2008), we adopt a distance to W5 of 2 kpc based on the water-maser parallax distance to the neighboring W3(OH) region (Hachisuka et al. 2006). As with W3, the W5 cloud is substantially ($\approx 1.5 \times$) closer than its kinematic distance would suggest ($v_{LSR}(-40 \text{ km s}^{-1}) \approx 3 \text{ kpc}$). Given this distance, Koenig et al. (2008) derived a total gas mass of $6.5 \times 10^4 M_\odot$ from a $2 \mu\text{m}$ extinction map.

The W5 complex was mapped in the ^{12}CO 1-0 emission line by the Five College Radio Astronomy Observatory (FCRAO) using the SEQUOIA receiver array (Heyer et al. 1998). The same array was used to map W5 in the ^{13}CO 1-0 line (C. Brunt, private communication). Some early work searched for outflows in W5 (Bretherton et al. 2002), but the low-resolution CO 1-0 data only revealed a few, and only one was published. The higher resolution and sensitivity observations presented here reveal many additional outflows.

While W5 is thought to be associated with the W3/4/5 complex, there are other infrared sources in the same part of the sky that are not obviously associated with W5. Some of these have been noted to be in the outer arm (several kpc behind W5) by Digel et al. (1996) and Snell et al. (2002).

In section 2, we present the new and archival data used in our study. In section 3, we discuss the outflow detection process and compare outflow detectability in W5 to that in Perseus. In section 4, we discuss the physical properties of the outflows and their implications for star formation in the W5 complex. In section 5, we briefly describe the outer-arm outflows discovered.

2 OBSERVATIONS

2.1 JCMT HARP CO 3-2

CO J=3-2 345.79599 GHz data were acquired at the 15 m James Clerk Maxwell Telescope (JCMT) using the HARP array on a series of observing runs in 2008. On 2-4 January, 2008, ~ 800 square arcminutes were mapped. During the run, τ_{225} , the zenith opacity at 225 GHz measured using the Caltech Submillimeter Observatory tipping radiometer, ranged from 0.1 to 0.4 ($0.4 < \tau_{345\text{GHz}} < 1.6$ ¹). Additional areas were mapped on 4-7 August, 16-20 and 31 October,

¹ <http://docs.jach.hawaii.edu/JCMT/SCD/SN/002.2/node5.html>

and 1 and 12-15 Nov 2008 in similar conditions. A total of ~ 3 square degrees (12000 arcmin^2) in the W5 complex were mapped (a velocity-integrated mosaic is shown in Figure 2).

HARP is a 16 pixel SIS receiver array acting as a front-end to the ACSIS digital auto-correlation spectrometer. In January 2008, 14 of the 16 detectors were functional. In the 2nd half of 2008, 12 of 16 were functional, necessitating longer scans to achieve similar S/N.

In January 2008, a single spectral window centered at 345.7959899 with bandwidth 1.0 GHz and channel width 488 kHz (0.42 km s^{-1}) was used. In August 2008 and later, we used 250 MHz bandwidth and 61 kHz (0.05 km s^{-1}) channel width. At this frequency, the beam FWHM is $14''$ (0.14 pc at a distance of 2 kpc)².

A raster mapping strategy was used. In 2008, the array was shifted by 1/2 of an array spacing ($58.2''$) between scans. Data was sampled at a rate of 0.6s per integration. Two perpendicular scans were used for each field observed. Most fields were $10 \times 10'$ and took ~ 45 minutes. When only 12 receptors were available, 1/4 array stepping ($29.1''$) was used with a sample rate of 0.4s per integration.

Data were reduced using the SMURF package within the STARLINK software distribution³. The SMURF command MAKECUBE was used to generate mosaics of contiguous sub-fields. The data were gridded on to cubes with $6''$ pixels and smoothed with a $\sigma = 2$ -pixel gaussian, resulting in a map FWHM resolution of $18''$ (0.17 pc). A linear fit was subtracted from each spectrum over emission-free velocities (generally -60 to -50 and -20 to -10 km s^{-1}) to remove the baseline. The final map RMS was $\sigma_{T_A^*} \sim 0.06 - 0.11 K$ in 0.42 km s^{-1} channels.

The sky reference position (off position) in January 2008 was J2000 2:31:04.069 +62:59:13.81. In later epochs, off positions closer to the target fields were selected from blank sky regions identified in January 2008 in order to increase observing efficiency. A main-beam efficiency $\eta_{mb} = 0.60$ was used as per the JCMT website to convert measurements to T_{mb} , though maps and spectra are presented in the original T_A^* units.

2.2 FCRAO Outer Galaxy Survey

The FCRAO Outer Galaxy Survey (OGS) observed the W5 complex in ^{12}CO (Heyer et al. 1998) and ^{13}CO 1-0 (C. Brunt, private communication). The ^{13}CO data cube achieved a mean sensitivity of 0.35 K per 0.13 km s^{-1} channel, or 0.6 K km s^{-1} integrated. The ^{13}CO cube was integrated over all velocities and resampled to match the BGPS map using the MONTAGE⁴ package. The FWHM beam size was $\theta_B = 50''$ (0.48 pc). The integrated ^{12}CO data cube, with a sensitivity $\sigma = 1K \text{ km s}^{-1}$, is displayed with region name identifications in Figure 3.

² http://docs.jach.hawaii.edu/JCMT/OVERVIEW/tel_overview/

³ <http://starlink.jach.hawaii.edu/>

⁴ <http://montage.ipac.caltech.edu/>

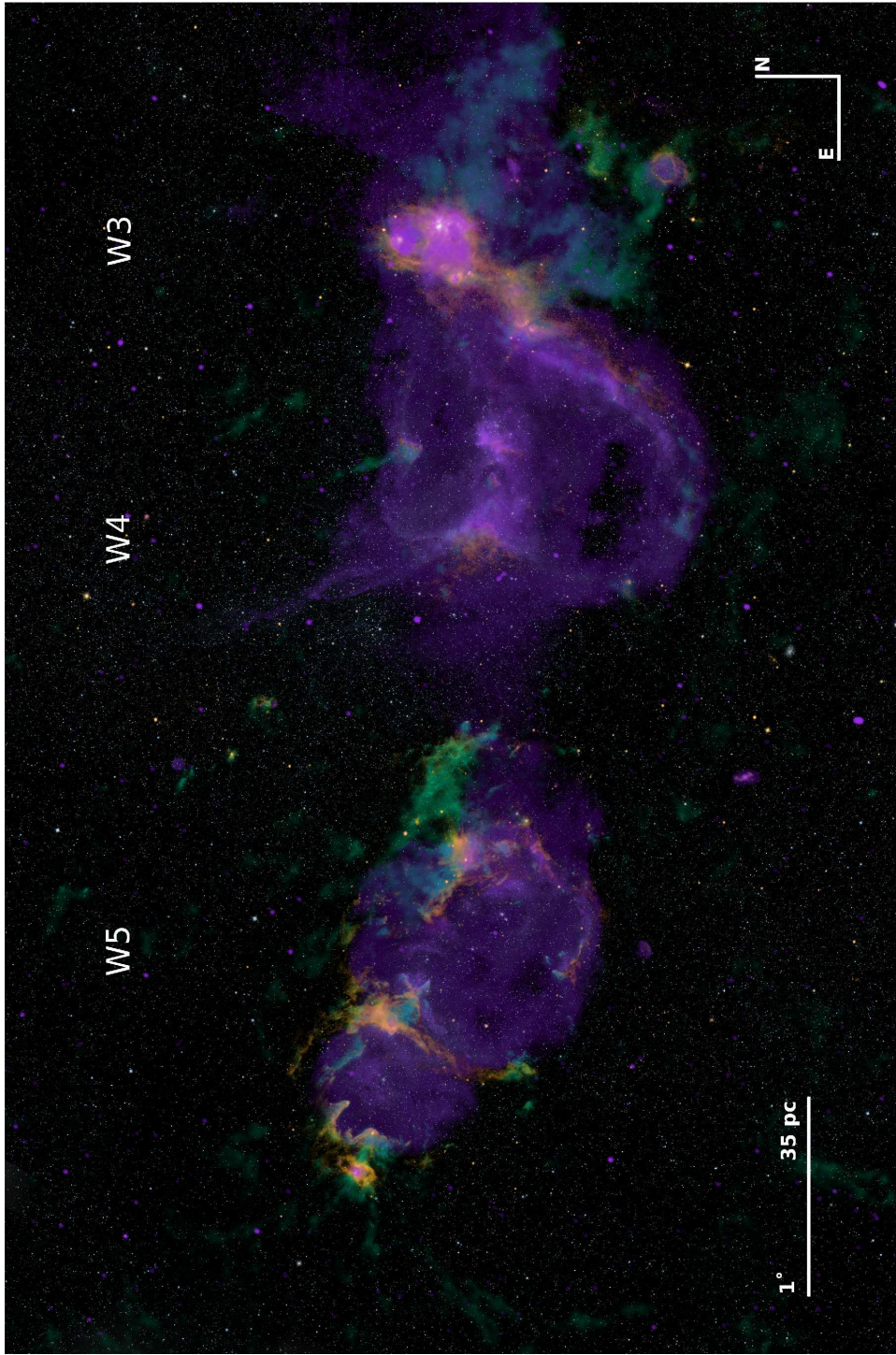


Figure 1. An overview of the W3/4/5 complex (also known as the “Heart and Soul Nebula”) in false color. Orange shows $8 \mu\text{m}$ emission from the Spitzer and MSX satellites. Purple shows 21 cm continuum emission from the DRAO CGPS (Taylor et al. 2003); the DSS R image was used to set the display opacity of the 21 cm continuum as displayed (purely for aesthetic purposes). The green shows JCMT ^{12}CO 3-2 along with FCRAO ^{12}CO 1-0 to fill in gaps that were not observed with the JCMT. The image spans $\sim 7^\circ$ in galactic longitude. This overview image shows the hypothesized interaction between the W4 superbubble and the W3 and W5 star-forming regions (Oey et al. 2005).

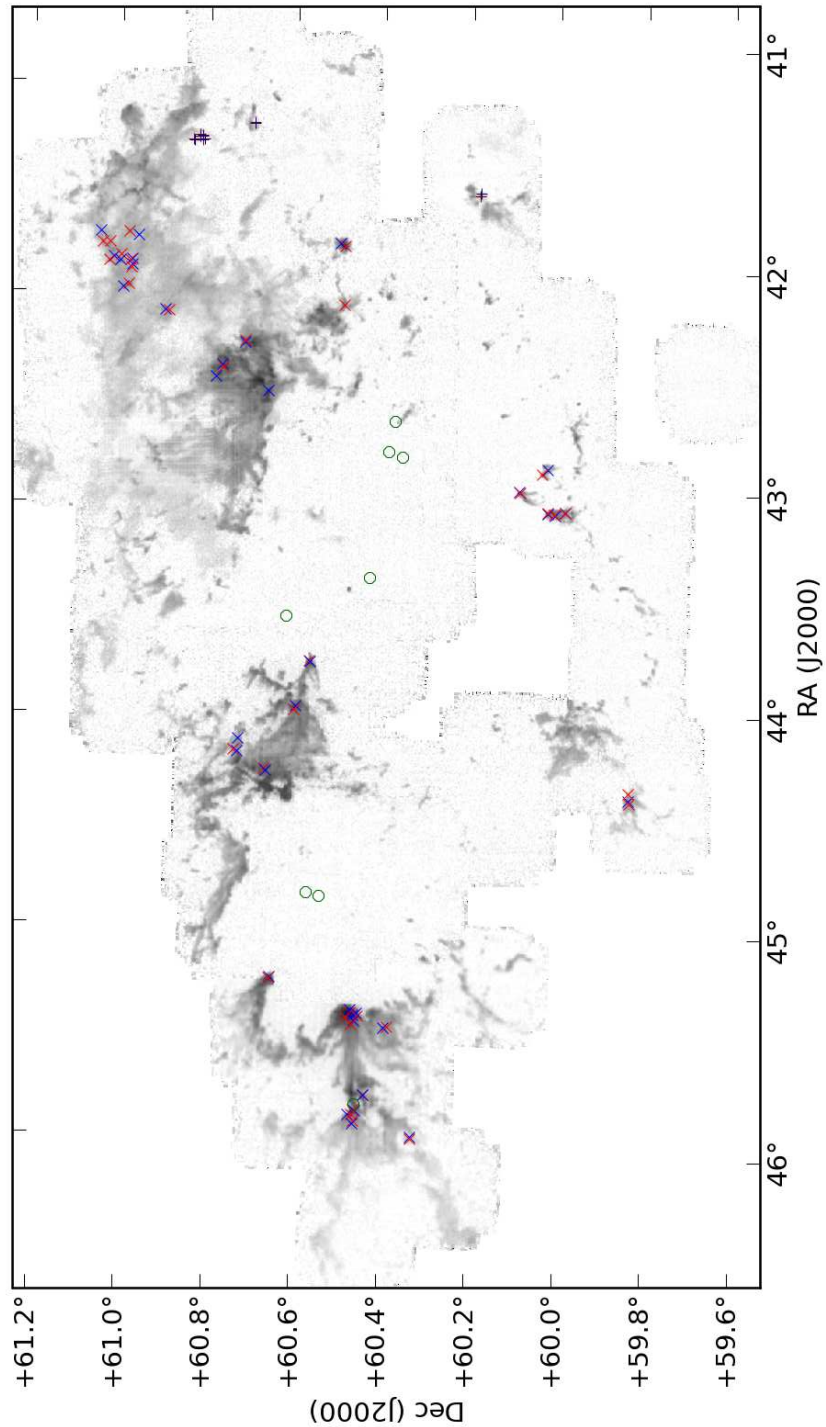


Figure 2. A mosaic of the CO 3-2 data cube integrated from -20 to -60 km s⁻¹. The grayscale is linear from 0 to 150 K km s⁻¹. The red and blue X's mark the locations of redshifted and blueshifted outflows. Dark red and dark blue plus symbols mark outflows at outer arm velocities. Green circles mark the location of all known B0 and earlier stars in the W5 region from SIMBAD.

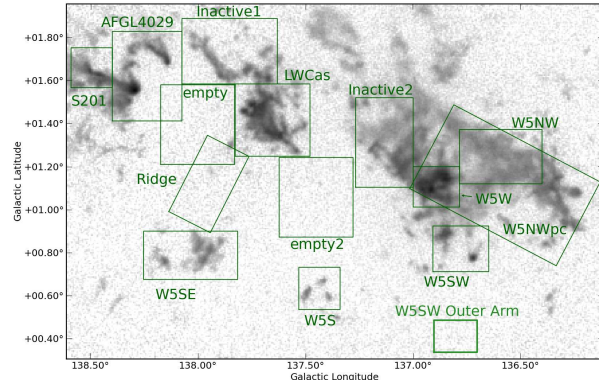


Figure 3. Individual region masks overlaid on the FCRAO ^{12}CO integrated image. The named regions, S201, AFGL4029, LWCas, W5NW, W5W, W5SE, W5S, and W5SW, were all selected based on the presence of outflows within the box. The inactive regions were selected from regions with substantial CO emission but without outflows. The ‘empty’ regions have essentially no CO emission within them and are used to place limits on the molecular gas within the east and west ‘bubbles’. W5NWpc is compared directly to the Perseus molecular cloud in Section 3.1.1

2.3 Spitzer

Spitzer IRAC and MIPS 24 μm images from Koenig et al. (2008) were used for morphological comparison. The reduction and extraction techniques are detailed in their paper.

3 ANALYSIS

3.1 Outflow Detections

Outflows were identified in the CO data cubes by manually searching through position-velocity space for line wings using STARLINK’s GAIA display software. Outflow candidates were identified by high velocity wings inconsistent with the local cloud velocity distribution, which ranged from a width of 3 km s^{-1} to 7 km s^{-1} . Once an outflow candidate was identified in the position-velocity diagrams, the velocity range over which the wing showed emission in the position-velocity diagram (down to $T_A^* = 0$) was integrated over to create a map from which the approximate outflow size and position was determined (e.g. Figures 4 and 5).

Unlike Curtis et al. (2010) and Hatchell & Dunham (2009), we did not use an ‘objective’ outflow identification method because of the greater velocity complexity and poorer spatial resolution of our observations. The outflow selection criteria in these papers requires the presence of a sub-mm clump in order to identify a candidate driving source (and therefore a targeted region in which to search for outflows), making a similar objective identification impossible for our survey. As discussed later in Section 4, the regions associated with outflows have wide lines and many are double-peaked. Additionally, many smaller areas associated with outflows have collections of gaussian-profiled clumps that are not connected to the cloud in position-velocity diagrams but are not outflows. In particular, W5 is pockmarked by dozens of small cometary globules that are sometimes spatially coincident with the clouds but slightly offset in velocity.

While Arce et al. (2010) described the benefits of 3D visualization using isosurface contours, we found that the

varying signal-to-noise across large-scale ($\sim 500 \text{ pixel}^2$) regions with significant extent in RA/Dec and limited velocity dynamic range made this method difficult for W5. There were many low-intensity outflows that were detectable by careful searches through position-velocity space that are not as apparent using isosurface methods. Out of the 55 outflows reported here, only 14⁵ would be considered obvious, high-intensity, high-velocity flows from their spectra alone; the rest could not be unambiguously detected without a search through position-velocity space.

In the majority of sources, the individual outflow lobes were unresolved, although some showed hints of position-velocity gradients at low significance and in many the red and blue flows are spatially separated. Only Outflow 1’s lobes were clearly resolved (Figure 4). Some of most suggestive gradients occurred where the outflow merged with its host molecular cloud in position-velocity space, making the gradient difficult to distinguish (e.g., Outflow 12, Figure 6). Bipolar pairs were selected when there were red and blue flows close to one another. The classification of a bipolar flow was either ‘yc’ (yes - confident), ‘yu’ (yes - unconfident), or ‘n’ (no) in Table 2. This identification is discussed in the captions for each outflow figure in the online supplement. The AFGL 4029 region has many red and blue lobes but confusion prevented pairing.

In cases where only the red- or blue-shifted lobe was visible, the surrounding pixels were searched for lower-significance and lower-velocity counterparts. For cases in which emission was detected, a candidate counterflow was identified and incorporated into the catalog. However, in 12 cases, the counterflow still evaded detection, either because of confusion or because the counterflow is not present in CO.

The outflow positions are overlaid on the CO 3-2 image in Figure 2 to provide an overview of where star formation is most active. The figures in Section 5.2 show outflow locations overlaid on small-scale images.

⁵ Outflows 15, 20, 24, the cluster of outflows 26-32, 47, 48, 52, and 53 could all have readily been detected by pointed single-dish measurements.

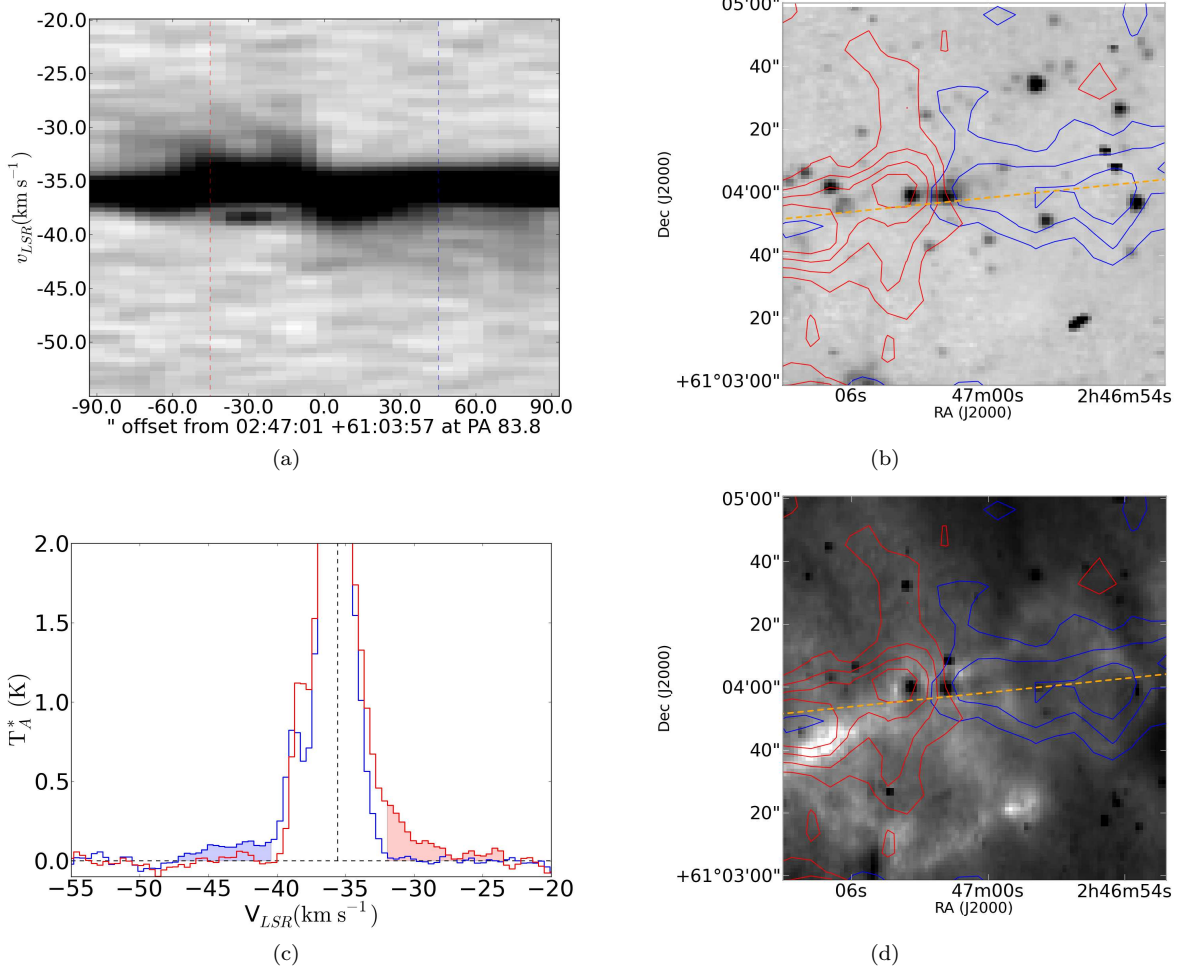


Figure 4. Position-velocity diagrams (a), spectra (c), and contour overlays of Outflow 1 on Spitzer 4.5 μm (b) and 8 μm (d) images. This outflow is clearly resolved and bipolar. (a): Position-velocity diagram of the blue flow displayed in arcsinh stretch from $T_A^* = 0$ to 3 K. Locations of the red and blue flows are indicated by vertical dashed lines. The location of the position-velocity cut is indicated by the orange dashed line in panels (b) and (d), although the position-velocity cut is longer than those cut-out images. (b) Spitzer 4.5 μm image displayed in logarithmic stretch from 30 to 500 MJy sr $^{-1}$. (c): Spectrum of the outflow integrated over the outflow aperture and the velocity range specified with shading. The velocity center (vertical dashed line) is determined by fitting a gaussian to the ^{13}CO spectrum in an aperture including both outflow lobes. In the few cases in which ^{13}CO 1-0 was unavailable, a gaussian was fit to the ^{12}CO 3-2 spectrum. (d): Contours of the red and blue outflows superposed on the Spitzer 8 μm image displayed in logarithmic stretch. The contours are generated from a total intensity image integrated over the outflow velocities indicated in panel (c). The contours in both panels (b) and (d) are displayed at levels of 0.5, 1, 1.5, 2, 3, 4, 5, 6 K km s $^{-1}$ ($\sigma \approx 0.25$ K km s $^{-1}$). The contour levels and stretches specified in this caption apply to all of the figures in the supplementary materials except where otherwise noted.

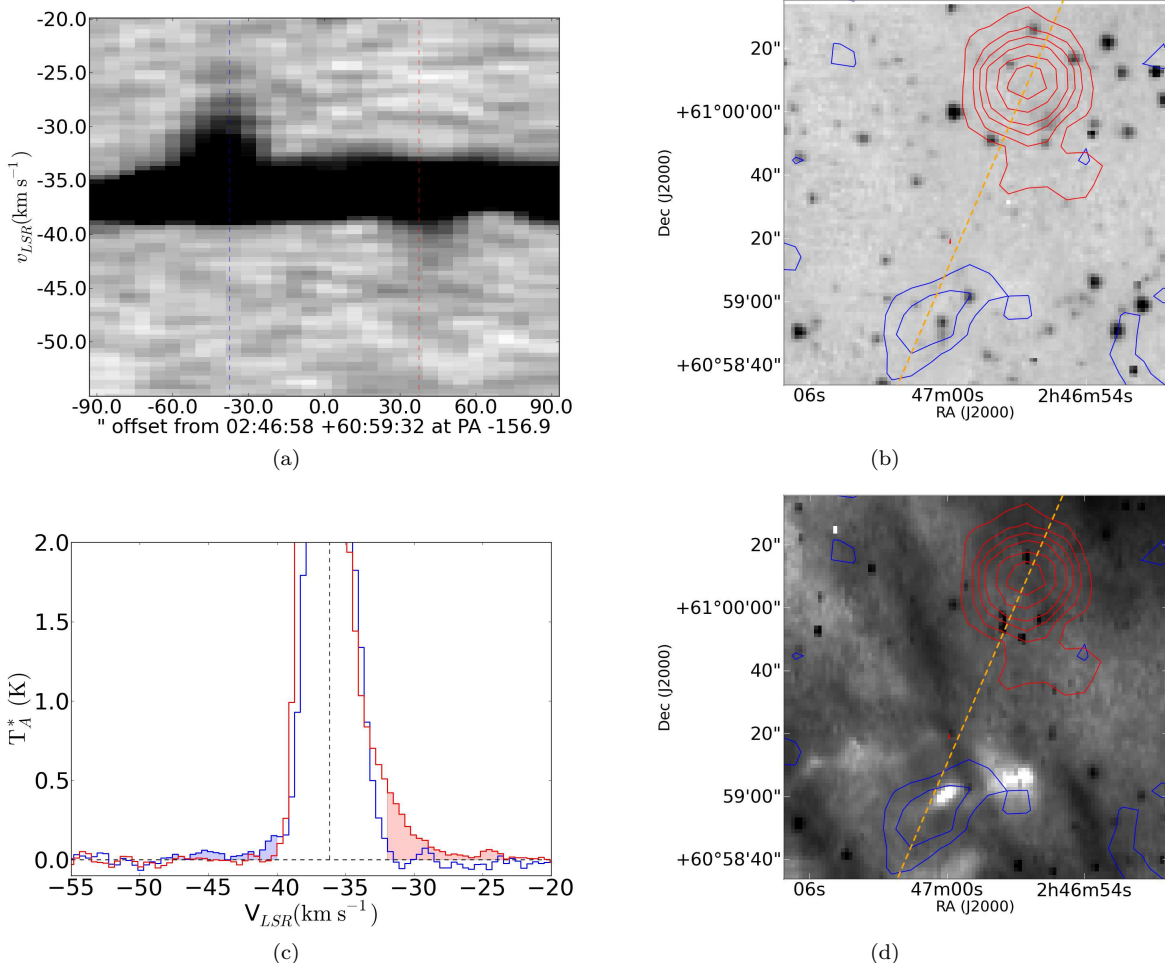


Figure 5. Position-velocity diagram, spectra, and contour overlays of Outflow 2 (see Figure 4 for a complete description). While the two lobes are widely separated, there are no nearby lobes that could lead to confusion, so we regard this pair as a reliable bipolar outflow identification.

Because our detection method involved searching for high-velocity outflows by eye, there should be no false detections. However, it is possible that some of these outflows are generated by mechanisms other than protostellar jets and winds since we have not identified their driving sources.

One possible alternative driving mechanism is a photoevaporation flow, which could be accelerated up to the sound speed of the ionized medium, $c_{II} \approx 10$ km s $^{-1}$. Gas accelerating away from the cloud would not be detected as an outflow because it would be rapidly ionized. However, gas driven inward would be accelerated and remain molecular. It could exhibit red and / or blue flows depending on the line of sight orientation. While there are viable candidates for this form of outflow impersonator, such flows can only have peak velocities $v \lesssim c_{II}/4 \approx 2.5$ km s $^{-1}$ in the strong adiabatic shock limit, so that any gas seen with higher velocity tails are unlikely to be radiation-driven.

Another plausible outflow impostor is the high-velocity tail in a turbulent distribution. However, for a typical molecular cloud, the low temperatures would require very high mach-number shocks ($\mathcal{M} \gtrsim 10$ assuming $T_{cloud} \sim 20$ K and $v_{flow} \sim 3$ km s $^{-1}$) that in idealized turbulence should be rare and short-lived. It is not known how frequent such

high-velocity excursions will be in non-ideal turbulence with gravity (A. Goodman, P. Padoan, private communication). Finally, it is less likely for turbulent intermittency to have nearly coincident red and blue lobes, so intermittency can be morphologically excluded in most cases.

3.1.1 Comparison to Perseus CO 3-2 observations

We used the HARP CO 3-2 cubes from Hatchell et al. (2007) to evaluate our ability to identify outflows. We selected an outflow that was well-resolved and unconfused, L1448, and evaluated it at both the native sensitivity of the Hatchell et al. (2007) observations and degraded in resolution and sensitivity to match our own. We focus on L1448 IRS2, labeled Outflow 30 in Hatchell et al. (2007). Figure 7 shows a comparison between the original quality and degraded data.

Integrating over the outflow velocity range, we measure each lobe to be about $1.6' \times 0.8'$ (0.14×0.07 pc). Assuming a distance to Perseus of 250 pc (e.g. Enoch et al. 2006), we smooth by a factor of 8 by convolving the cube with a FWHM = 111'' gaussian, then downsample by the same factor of 8 to achieve 6'' square pixels at 2 kpc. The resulting noise was reduced because of the spatial and spectral

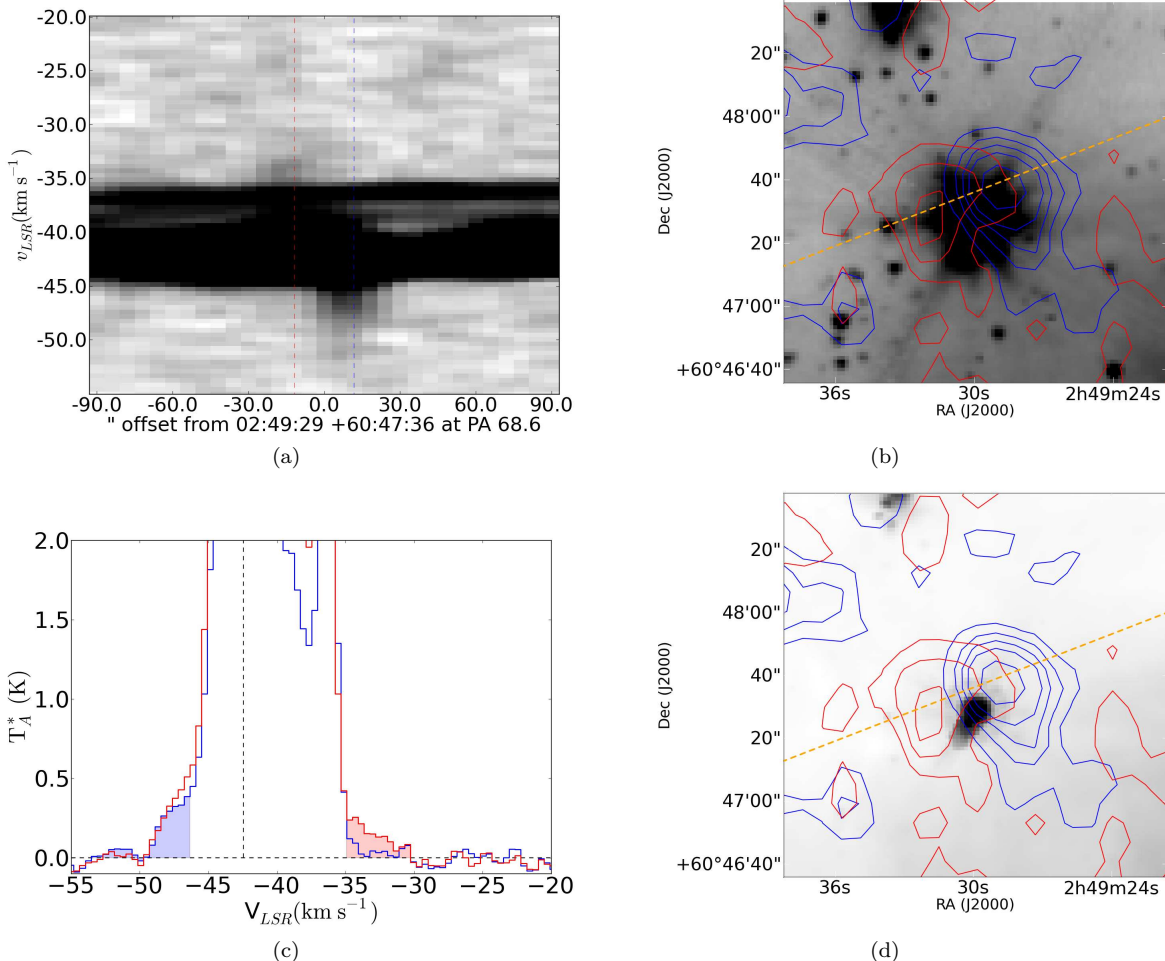


Figure 6. Position-velocity diagram, spectra, and contour overlays of Outflow 12. Much of the red outflow is lost in the complex velocity profile of the molecular cloud(s), but it is high enough velocity to still be distinguished.

smoothing and was measured to be ≈ 0.05 K in 0.54 km s $^{-1}$ channels, which is comparable to the sensitivity in our survey. It is still possible to distinguish the outflows from the cloud in position-velocity space. Each lobe is individually unresolved (long axis $\sim 12''$ compared to our beam FWHM of $18''$), but the two are separated by $\gtrsim 20''$ and therefore an overall spatial separation can still be measured. Because they are just barely unresolved at this distance, the lobes' surface brightnesses are approximately the same at 2 kpc as at 250 pc; if this outflow were seen at a greater distance it would appear fainter.

Hatchell et al. (2007) detected 4 outflows within this map, plus an additional confused candidate. We note an additional grouping of outflowing material in the north-middle of the map (centered on coordinate 150×150 in Figure 7). In the smoothed version, only three outflows are detected in the blue and two in the red, making flow-counterflow association difficult. The north-central blueshifted component appears to be the counterpart of the red flow when smoothed, although it is clearly the counterpart of the northwest blue flow in the full-resolution image.

We are therefore able to detect any outflows comparable to L1448 (assuming a favorable geometry), but are likely to see clustered outflows as single or possibly extended lobes

and will count fewer lobes than would be detected at higher resolution. Additionally, it is clear from this example that two adjacent outflows with opposite polarity are not necessarily associated, and therefore the outflows' source(s) may not be between the two lobes.

In order to determine overall detectability of outflows compared to Perseus, we compare to Curtis et al. (2010) in Figure 8. Out of 29 outflows in their survey with measured 'lobe lengths', 22 (71%) were smaller than $128''$ which would be below our $18''$ resolution if observed at 2 kpc. Even the largest lobes (HRF26R, HRF28R, HRF44B) would only extend $\sim 60''$ at 2 kpc. Each lobe in the largest outflow in our survey, Outflow 1, is $\sim 80''$ ($660''$ at 250pc), but no other individual outflow lobes in W5 are clearly resolved. However, as seen in Figure 8, many bipolar lobes are *separated* by more than the telescope resolution, and the overall lobe separation distribution (as opposed to the lobe length, which is mostly unmeasured in our sample) in W5 is quite similar to the separation distribution in Perseus. The 2-sample KS test gives a 25% probability that they are drawn from the same distribution (the null hypothesis that they are drawn from the same distribution cannot be rejected).

On average, the Curtis et al. (2010) outflow velocities are similar to ours (Figure 9). We detect lower velocity out-

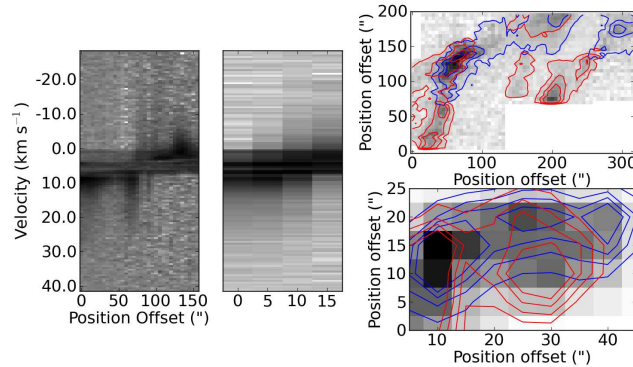


Figure 7. Comparison of L1448 seen at a distance of 250 pc (left) versus 2 kpc (middle) with sensitivity 0.5 K and 0.05K per 0.5 km s⁻¹ channel respectively. *Far Left:* Position-velocity diagram (log scale) of the outflow L1448 IRS2 at its native resolution and velocity. L1448 IRS2 is the rightmost outflow in the contour plots. The PV diagram is rotated 45° from RA/Dec axes to go along the outflow axis. *Middle Left:* Position-velocity diagram (log scale) of the same outflow smoothed and rebinned to be eight times more distant. *Top Right:* The integrated map is displayed at its native resolution (linear scale). The red contours are of the same data integrated from 6.5 to 16 km s⁻¹ and the blue from -6 to 0 km s⁻¹. Contours are at 1,3, and 5 K km s⁻¹ ($\sim 6, 18, 30\sigma$). Axes are offsets in arcseconds. Because we are only examining the relative detectability of outflows at two distances, we are not concerned with absolute coordinates. *Bottom Right:* The same map as it would be observed at eight times greater distance. Axes are offsets in arcseconds assuming the greater distance. Contours are integrated over the same velocity range as above, but are displayed at levels 0.25, 0.50, 0.75, 1.00 K km s⁻¹ ($\sim 12, 24, 48, 60\sigma$). The entire region is detected at high significance, but dominated by confusion. It is still evident that the red and blue lobes are distinct, but they are each unresolved.

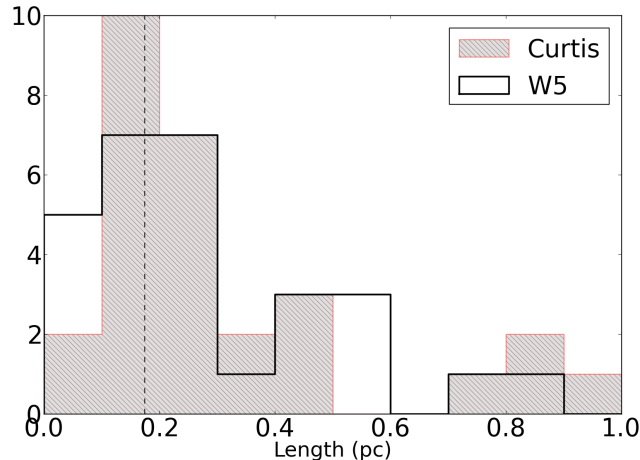


Figure 8. Histogram of the measured outflow lobe separations. The grey hatched region shows Curtis et al. (2010) values. The vertical dashed line represents the spatial resolution of our survey. The two distributions are similar.

flows because we do not set a strict lower velocity limit criterion. We do not detect the highest velocity outflows most likely because of our poorer sensitivity to the faint high-velocity tips of outflows, although it is also possible that no high-velocity ($v > 20 \text{ km s}^{-1}$) flows exist in the W5 region. Note that the histogram compares quantities that are not directly equivalent: the outflows in Curtis et al. (2010) and our own data are measured out to the point at which the outflow signal is lost, while the ‘region’ velocities are full-width half-max (FWHM) velocities.

Finally, we use the detectability of outflows in Perseus to inform our expectations in W5. Since it appears that we can detect outflows from low-mass protostars with sub-stellar to $\sim 30L_\odot$ luminosities at the distance of W5 and these objects should be the most numerous in a standard initial mass function, the distribution of physical properties in W5 outflows should be similar to those in Perseus. However, because W5 is a somewhat more massive cloud ($M_{W5} \approx 5M_{\text{Perseus}}^6$), we might expect the high-end of the distribution to extend to higher values of outflow mass, momentum, and energy. Since we will likely see clustered outflows confused into a smaller number of distinct lobes, we expect a bias towards higher values of the derived quantities but a lower detection rate.

3.1.2 Velocity, Column Density, and Mass Measurements

Throughout this section, we assume that the CO lines are optically thin and thermally excited. The measured properties are presented in Table 2. These assumptions are likely to be invalid, so we also discuss the consequences of applying ‘typical’ optical depth corrections to the derived quantities. Because we do not measure optical depths and the optical depth correction for CO 3-2 is less well quantified than for CO 1-0 (Curtis et al. 2010; Cabrit & Bertout 1990)⁷, we only present the uncorrected measurements in Table 3.

The outflow velocity ranges were measured by examining both RA-velocity and Dec-velocity diagrams interactively using the STARLINK GAIA data cube viewing tool. The velocity limits are set to include all outflow emission that is distinguishable from the cloud (i.e. the velocity at which outflow lobes dominate over the gaussian wing of the cloud emission) down to zero emission. An outflow size (or lobe size, following Curtis et al. 2010) was determined by integrating over the blue and red velocity ranges and creating an elliptical aperture to include both peaks; the position and size therefore have approximately beam-sized ($\approx 18''$) accuracy. The integrated outflow maps are shown as red and blue contours in Figure 5. The velocity center was computed

⁶ M_{W5} is estimated from ^{13}CO . We also estimate the total molecular mass in W5 using the X-factor and acquire $M_{W5} = 5.0 \times 10^4 M_\odot$, in agreement with Karr & Martin (2003), who estimated a molecular mass of 4.4×10^4 from ^{12}CO using the same X-factor. Koenig et al. (2008) estimated a total gas mass of 6.5×10^4 from a 2MASS extinction map. The total molecular mass in Perseus is $M_{\text{Perseus}} \sim 10^4$ (Bally et al. 2008)

⁷ In Curtis et al. (2010), this correction factor ranged from 1.8 to 14.3; Arce et al. (2010) did not enumerate the optical depth correction they used but it is typically around 7 (Cabrit & Bertout 1990).

by fitting a gaussian to the FCRAO ^{13}CO spectrum averaged over the elliptical aperture.

The column density is estimated from ^{12}CO J=3-2 assuming local thermal equilibrium (LTE) and optically thin emission using the equation $N(\text{H}_2) = 5.3 \times 10^{18} \eta_{mb}^{-1} \int T_A^*(v) dv$ for $T_{ex} = 20 \text{ K}$. The derivation is given in the Appendix. The column density in the lobes is likely to be dominated by low-velocity gas and therefore our dominant uncertainty may be missing low-velocity emission rather than poor assumptions about the optical depth.

The scalar momentum and energy were computed from

$$p = M \frac{\sum T_A^*(v)(v - v_c)\Delta v}{\sum T_A^*(v)\Delta v} \quad (1)$$

$$E = \frac{M}{2} \frac{\sum T_A^*(v)(v - v_c)^2 \Delta v}{\sum T_A^*(v)\Delta v} \quad (2)$$

where v_c is the ^{13}CO 1-0 centroid velocity. The same assumptions used in determining column density are applied here.

We estimate an outflow lifetime by taking half the distance between the red and blue outflow centroids divided by the maximum measured velocity difference ($\Delta v_{max} = (v_{max,red} - v_{max,blue})/2$), $\tau_{flow} = L_{flow}/(2\Delta v_{max})$, where L_{flow} refers to the length of the flow. This method assumes that the outflow inclination is 45° ; if it is more parallel to the plane of the sky, we overestimate the age, and vice-versa. The momentum flux is then $\dot{P} = p/\tau$. Similarly, we compute a mass loss rate by dividing the total outflow mass by the dynamical age, which yields what is likely a lower limit on the mass loss rate (if the lifetime is underestimated, the mass loss rate is overestimated, but the outflow mass is always a lower limit because of optical depth and confusion effects).

The dynamical ages are highly suspect since the red and blue lobes are often unresolved or barely resolved, and diffuse emission averaged with the lobe emission can shift the centroid position. Additionally, it is not clear what portion of the outflow corresponds to the centroid: the bow shock or the jet could both potentially dominate the outflow emission. Curtis et al. (2010) discuss the many ways in which the dynamical age can be in error. Our mass loss rates are similar to those in Perseus *without* correcting our measurements for optical depth, while our outflow masses are an order of magnitude lower. It therefore appears that our dynamical age estimates must be too low, since we have no reason to expect protostars in W5 to be undergoing mass loss at a greater rate than those in Perseus. However, given more reliable dynamical age estimates from higher resolution observations of shock tracers, the mass loss rates could be corrected and compared to other star-forming regions.

Because the emission was assumed to be optically thin, the mass, column, energy, and momentum measurements we present are strictly lower limits. While some authors have computed correction factors to ^{12}CO 1-0 optical depths (e.g. Cabrit & Bertout 1990), the corrections are different for the 3-2 transition (1.8 to 14.3, Curtis et al. 2010). Additionally, CO 3-2 may require a correction for sub-thermal excitation because of its higher critical density (the CO 3-2 critical density is 27 times higher than CO 1-0; see Appendix A for modeling of this effect).

Additionally, most of the outflow mass is at the lowest distinguishable velocities in typical outflows (e.g. Arce et al.

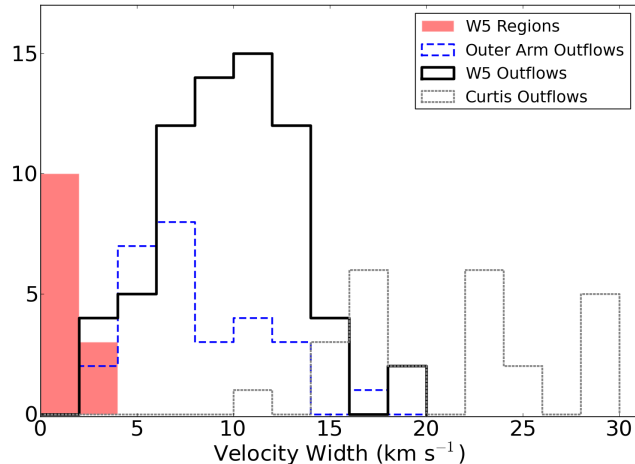


Figure 9. Histogram of the outflow line widths. *Black lines:* histogram of the measured outflow widths (half-width zero-intensity, measured from the fitted central velocity of the cloud to the highest velocity with non-zero emission). *Blue dashed lines:* outflow half-width zero-intensity (HWZI) for the outer arm (non-W5) sample. *Solid red shaded:* The measured widths (HWHM) of the sub-regions as tabulated in Table 1. *Gray dotted:* Outflow v_{max} (HWZI) values for Perseus from Curtis et al. (2010).

2010). It is therefore plausible that in the more turbulent W5 region, a greater fraction of the outflow mass is blended with the cloud and therefore not included in mass, momentum, and energy measurements. This omission could be greater than the underestimate due to poor opacity assumptions.

The total mass of the W5 outflows is $M_{tot} \approx 1.5 M_{\odot}$, substantially lower, even with an optical depth correction of $10\times$, than the $163 M_{\odot}$ reported in Perseus (Arce et al. 2010). Arce et al. (2010) also include a correction factor of 2.5 to account for higher temperatures in outflows and a factor of 2 to account for emission blended with the cloud. The temperature correction is inappropriate for CO 3-2 (see Appendix A, Figure A1), but the resulting total outflow mass in W5 with an optical depth correction and a factor of 2 confusion correction is about $30 M_{\odot}$. In order to make our measurements consistent with a mass of $160 M_{\odot}$, a density upper limit in the outflowing gas of $n(\text{H}_2) < 10^{3.5} \text{ cm}^{-3}$ is required, since a lower gas density results in greater mass for a given intensity (see Appendix A, Figure A2). However, we expect the total outflow mass in W5 to be greater than in Perseus because of the greater cloud mass, implying that the density in the flows must be even lower, or additional corrections are needed.

The total outflow momentum is $p_{tot} \approx 10.9 M_{\odot} \text{ km s}^{-1}$, versus a quoted $517 M_{\odot} \text{ km s}^{-1}$ in Perseus (Arce et al. 2010). Arce et al. (2010) included inclination and dissociative shock corrections for the momentum measurements on top of the correction factors already applied to the mass. If these corrections are removed from the Perseus momentum total (except for optical depth, which is variable in their data and therefore cannot be removed), the uncorrected outflow momentum in Perseus would be about $74 M_{\odot} \text{ km s}^{-1}$. The W5 outflow momentum, if corrected with a ‘typical’ optical depth in the range 7-14, would match or exceed this value. If an additional CO 3-2 excitation correction (in the range 1-20) is applied, the W5 outflow momentum would significantly exceed that in Perseus.

Assuming a turbulent line width $\Delta v \sim 3 \text{ km s}^{-1}$ (approximately the smallest FWHM line-width observed), the

total turbulent momentum in the ambient cloud is $p = M_{tot} \Delta v = 1.3 \times 10^5 M_{\odot} \text{ km s}^{-1}$, which is $\sim 10^5$ times the measured outflow momentum - the outflows detected in our survey cannot be the sole source of the observed turbulent line widths, even if corrected for optical depth and missing mass.

Table 1 presents the turbulent momentum for each sub-region computed by multiplying the measured velocity width by the integrated ^{13}CO mass. Even if the outflow measurements are orders of magnitude low because of optical depth, cloud blending, sub-thermal excitation, and other missing-mass considerations, outflows contribute negligibly to the total momentum of high velocity gas in W5. This result is unsurprising, as there are many other likely sources of energy in the region such as stellar wind bubbles and shock fronts between the ionized and molecular gas. Additionally, in regions unaffected by feedback from the HII region (e.g. W5NW), cloud-cloud collisions are a possible source of energy.

Figure 10 displays the distribution of measured properties and compares them to those derived in the COMPLETE (Arce et al. 2010) and Curtis et al. (2010) HARP CO 3-2 surveys of Perseus. Our derived masses are substantially lower than those in Arce et al. (2010) even if corrected for optical depth, but our momenta are similar to the CPOC (COMPLETE Perseus Outflow Candidate) sample and our energies are higher, indicating a bias towards detecting mass at high velocities. The bias is more heavily towards high velocities than the CO 1-0 used in Arce et al. (2010). The discrepancy between our values and those of Arce et al. (2010) and Curtis et al. (2010) can be partly accounted for by the optical depth correction applied in those works: ^{13}CO was used to correct for opacity at low velocities, where most of the outflow mass is expected. Those works may also have been less affected by blending because of the smaller cloud line widths in Perseus.

The momentum flux and mass loss rate are compared to the values derived in Perseus by Hatchell et al. (2007) and Curtis et al. (2010) in Figures 11 and 12. Both of our

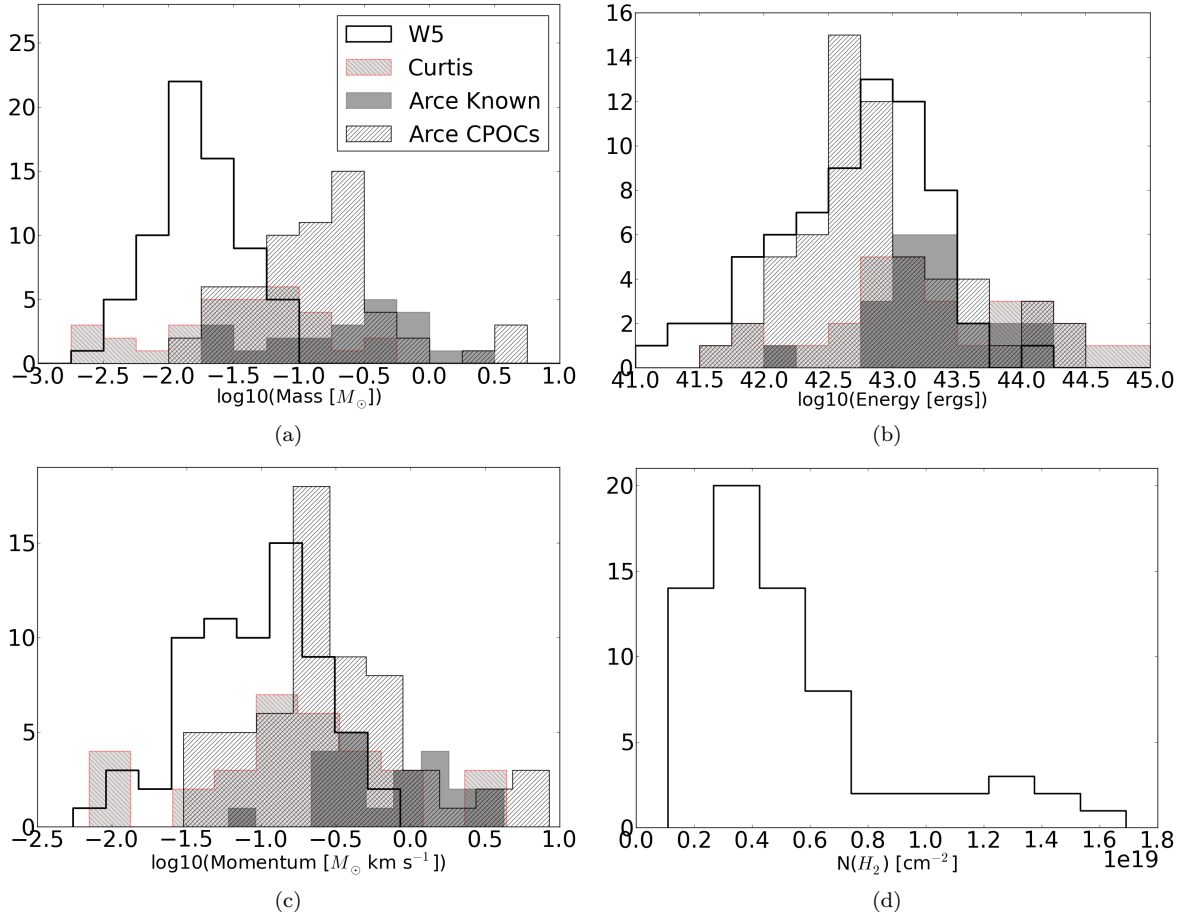


Figure 10. Histograms of outflow physical properties. The solid unfilled lines are the W5 outflows (this paper), the forward-slash hashed lines show Arce et al. (2010) CPOCs, the dark gray shaded region shows Arce et al. (2010) values for known outflows in Perseus, and the light gray, backslash-hashed regions show Curtis et al. (2010) CO 3-2 outflow properties. The outflow masses measured in Perseus are systematically higher partly because both surveys corrected for line optical depth using ^{13}CO . The medians of the distributions are $0.017, 0.044, 0.33$, and $0.14 M_\odot$ for W5, Curtis, Arce Known, and Arce CPOCs respectively, which implies that an optical depth and excitation correction factor of 2.5-20 would be required to make the distributions agree (although W5, being a more massive region, might be expected to have more massive and powerful outflows). It is likely that CO 3-2 is sub-thermally excited in outflows, and CO outflows may be destroyed by UV radiation in the W5 complex while they easily survive in the lower-mass Perseus region, which are other factors that could push the W5 mass distribution lower.

values are computed using the dynamical timescale τ_d measured from outflow lobe separation, while the Hatchell et al. (2007) values are derived using a more direct momentum-flux measurement in which the momentum flux contribution of each pixel in the resolved outflow map is considered. The derived momentum fluxes (Figure 11) are approximately consistent with the Curtis et al. (2010) Perseus momentum fluxes; Curtis et al. (2010) measure momentum fluxes in a range $1 \times 10^{-6} < \dot{P} < 7 \times 10^{-4} M_\odot \text{ km s}^{-1} \text{ yr}^{-1}$, higher than our measured $6 \times 10^{-7} < \dot{P} < 1 \times 10^{-4} M_\odot \text{ km s}^{-1} \text{ yr}^{-1}$ by approximately the opacity correction they applied. As seen in Figure 11, the Hatchell et al. (2007) momentum flux measurements in Perseus cover a much lower range $6 \times 10^{-8} < \dot{P} < 2 \times 10^{-5} M_\odot \text{ km s}^{-1} \text{ yr}^{-1}$ and are not consistent with our measurements. This disagreement is most likely because of the difference in method. The W5 outflows exhibit substantially higher mass-loss rates and momentum fluxes if we assume a factor of 10 opacity correction, as

expected from our bias toward higher-velocity, higher-mass flows.

3.2 Structure of the W5 molecular clouds: A thin sheet?

The W5 complex extends $\sim 1.6^\circ \times 0.7^\circ$ within 20° of parallel with the galactic plane. At the assumed distance of 2 kpc, it has a projected length of ~ 60 pc (Figure 2). In the $8 \mu\text{m}$ band (Figure 1), the region appears to consist of two blown-out bubbles with $\sim 10 - 15$ pc radii centered on $\ell = 138.1, b = 1.4$ and $\ell = 137.5, b = 0.9$. While the bubbles are filled in with low-level far-infrared emission, there is no CO detected down to a $3 - \sigma$ limit of 3.0 K km s^{-1} ($^{12}\text{CO } 1-0$), 2.4 K km s^{-1} ($^{12}\text{CO } 3-2$, excepting a few isolated clumps), and 1.5 K km s^{-1} ($^{13}\text{CO } 1-0$). Using the X-factor (the CO-to-H₂ conversion factor) for ^{12}CO $N(\text{H}_2) = 3.6 \times 10^{20} \text{ cm}^{-2}/(\text{K km s}^{-1})$, we derive an upper limit $N(\text{H}_2) < 1.1 \times 10^{21} \text{ cm}^{-2}$, or $A_V \lesssim 0.6$. Individual

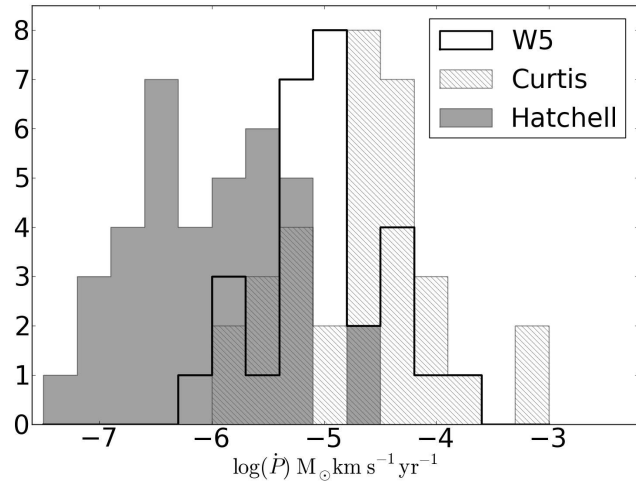


Figure 11. Histogram of the measured outflow momentum fluxes. The black thick line shows our data, the grey shaded region shows the Hatchell et al. (2007) data, and the hatched region shows Curtis et al. (2010) values. Our measurements peak squarely between the two Perseus JCMT CO 3-2 data sets, although the Curtis et al. (2010) results include an opacity correction that our data do not, suggesting that our results are likely consistent with Curtis et al. (2010) but inconsistent with the Hatchell et al. (2007) direct measurement method.

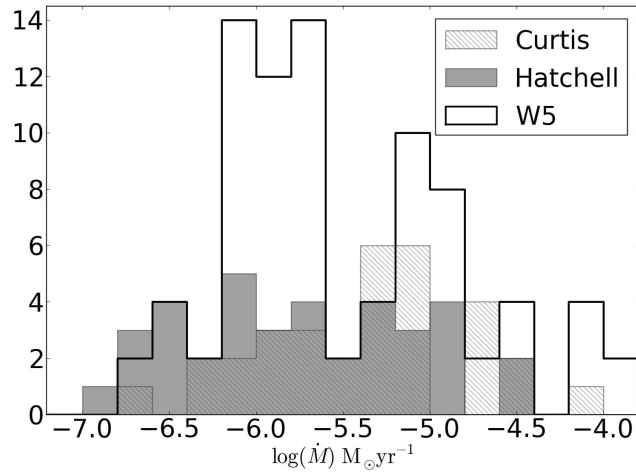


Figure 12. Histogram of the measured mass loss rate. The black thick line shows our data, while the grey shaded region shows the Hatchell et al. (2007) data, which is simply computed by $\dot{M} = \dot{P} \times 10/5 \text{ km s}^{-1}$, where the factor of 10 is a correction for opacity. Our mass loss rates are very comparable to those of Hatchell et al. (2007), but different methods were used so the comparison may not be physically meaningful. Curtis et al. (2010) (hatched) used a dynamical time method similar to our own and also derived similar mass loss rates, although their mass measurements have been opacity-corrected using the ^{13}CO 3-2 line. Because our mass loss rates agree reasonably with Perseus, but our outflow mass measurements are an order of magnitude low, we believe our dynamical age estimates to be too small.

‘wisps’ and ‘clumps’ of CO can sometimes be seen, particularly towards the cloud edges, but in general the bubbles are absent of CO gas.

Given such low column limits, the W5 cloud must be much smaller along the line of sight than its ~ 50 pc size projected on the sky. Alternately, along the line-of-sight, the columns of molecular gas are too low for CO to self-shield, and it is therefore destroyed by the UV radiation of W5’s O-stars. In either case, there is a significant excess of molecular gas in the plane of the sky compared to the line of sight, which makes W5 an excellent location to perform unobscured observations of the star formation process. The implied thin geometry of the W5 molecular cloud may therefore be similar to the bubbles observed by Beaumont & Williams (2010), but on a larger scale.

There is also morphological evidence supporting the face-on hypothesis. In the AFGL 4029 region (Section 4.2) and all along the south of W5, there are ridges with many individual cometary ‘heads’ pointing towards the O-stars that are unconfused along the line of sight. This sort of separation would not be expected if we were looking through the clouds towards the O-stars. W5W, however, presents a counterexample in which there are two clouds along the line of sight that may well be masking a more complex geometry.

4 SUB-REGIONS

Individual regions were selected from the mosaic for comparison. All regions with multiple outflows and indicators of star formation activity were named and included as regions for analysis. Additionally, three “inactive” regions were selected based on the presence of ^{13}CO emission but the lack of outflows in the ^{12}CO 3-2 data. Finally, two regions devoid of CO emission were selected as a baseline comparison and to place upper limits on the molecular gas content of the east and west ‘bubbles’. The regions are identified on the integrated ^{13}CO image in Figure 3.

Average spectra were taken of each “region” within the indicated box. Gaussians were fit to the spectrum to determine line-widths and centers (Figure 13, Table 1). Gaussian fits were necessary because in many locations there are at least two velocity components, so the second moment (the “intensity-weighted dispersion”) is a poor estimator of line width. Widths ranged from $v_{FWHM} = 2.3$ to 6.2 km s $^{-1}$ (Figure 9).

4.1 Sh 2-201

Sh 2-201 is an HII region and is part of the same molecular cloud as the bright-rimmed clouds in W5E, but it does not share a cometary shape with these clouds (Figure 14). Instead, it is internally heated and has its own ionizing source (Felli et al. 1987). The AFGL 4029 cloud edge is at a projected distance of ~ 7 pc from the nearest exposed O-star, and the closest illuminated point in the Spitzer 8 and 24 μm maps is at a projected distance of ~ 5 pc. The star forming process must therefore have begun before radiation driven shocks from the W5 O-stars could have impacted the cloud.

4.2 AFGL 4029

AFGL 4029 is a young cluster embedded in a cometary cloud (Figure 15). There is one clear bipolar outflow and 6 single-lobed flows that cannot be unambiguously associated with an opposite direction counterpart. The cluster is mostly unresolved in the data presented here and is clearly the most active CO clump in W5. It contains a cluster of at least 30 B-stars (Deharveng et al. 1997). The outflows from this region have a full width $\Delta v \approx 30$ km s $^{-1}$, which is entirely inconsistent with a radiation-driven inflow or outflow since it is greater than the sound speed in the ionized medium.

The northeast cometary cloud is strongly affected by the W5 HII region. It has an outflow in the head of the cloud (Figure 16), and the cloud shows a velocity gradient with distance from the HII region. The polarity of the gradient suggests that the cometary cloud must be on the far side of the ionizing O-star along the line of sight assuming that the HII region pressure is responsible for accelerating the cloud edge.

4.3 W5 Ridge

The W5 complex consists of two HII region bubbles separated by a ridge of molecular gas (Figure 17). This ridge contains the LW Cas optical nebula, a reflection nebula around the variable star LW Cas, on its east side and an X-shaped nebula on the west. The east portion of LW Cas Nebula is bright in both the continuum and CO J=3-2 but lacks outflows (see Figure 17). The east portion also has the highest average peak antenna temperature, suggesting that the gas temperature in this region is substantially higher than in the majority of the W5 complex (higher spatial densities could also increase the observed T_A , but the presence of nearby heating sources make a higher temperature more plausible). It is possible that high gas temperatures are suppressing star formation in the cloud. Alternately, the radiation that is heating the gas may destroy any outflowing CO, which is more likely assuming the two Class I objects identified in this region by Koenig et al. (2008) are genuine protostars.

The ridge is surprisingly faint in HI 21 cm emission compared to the two HII regions (Figure 18) considering its 24 μm surface brightness. The integrated HI intensity from -45 to -35 km s $^{-1}$ is ~ 800 K km s $^{-1}$, whereas in the HII region bubble it is around 1000 K km s $^{-1}$. The CO-bright regions show lower levels of emission similar to the ridge at 700-800 K km s $^{-1}$. However, the ridge contains no CO gas and very few young stars (Figure 7 in Koenig et al. 2008). It is possible that the ridge contains cool HI but has very low column-densities along the direction pointing towards the O-stars, in which case the self-shielding is too little to prevent CO dissociation. This ridge may therefore be an excellent location to explore the transition from molecular to atomic gas under the influence of ionizing radiation in conditions different from high-density photodissociation (photon-dominated) regions.

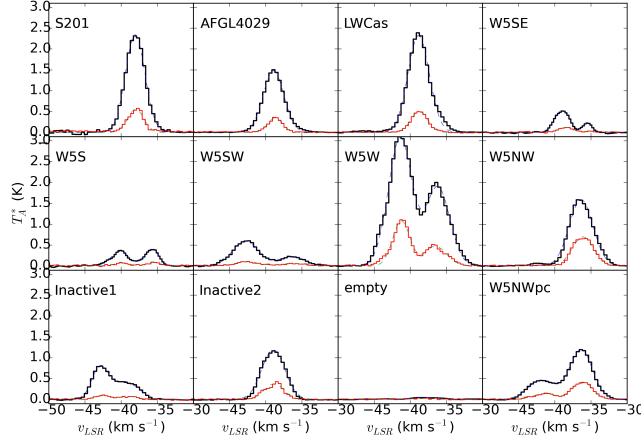
We examine Outflow 20 as a possible case for pressure-driven implosion (radiation, RDI, or gas pressure, PDI) by examining the relative timescales of the outflow driving source and the HII-region-driven compression front. A typical molecular outflow source (Class 0 or I) has a lifetime of $\sim 5 \times 10^5$ years (Evans et al. 2009). Given that there

Table 1. Gaussian fit parameters of sub-regions

Region	Velocity 1 (km s ⁻¹)	Width 1 (FWHM, km s ⁻¹)	Amplitude 1 (K)	Velocity 2 (km s ⁻¹)	Width 2 (FWHM, km s ⁻¹)	Amplitude 2 (K)
S201	-38.04	3.149	2.35	-	-	-
AFGL4029	-38.91	3.3605	1.48	-	-	-
LWCas	-38.83	3.478	2.33	-	-	-
W5W	-41.37	3.8775	3.07	-36.16	3.8305	1.90
W5NW	-36.37	3.854	1.6	-	-	-
W5NWpc	-36.37	3.713	1.19	-41.81	4.3475	0.47
W5SW	-42.78	4.136	0.6	-36.34	4.183	0.22
W5S	-40.15	2.914	0.34	-35.76	2.2795	0.40
Inactive1	-42.91	2.6555	0.75	-39.38	4.2065	0.42
Inactive2	-38.94	3.7365	1.2	-	-	-
empty	-37.81	5.217	0.04	-	-	-

¹³ CO fits	¹³ CO mass (M _⊙)	¹³ CO momentum (M _⊙ km s ⁻¹)	¹³ CO energy (ergs)
S201	1300	3500	8.9×10 ⁴⁶
AFGL4029	2600	6100	1.4×10 ⁴⁷
LWCas	3700	10000	2.7×10 ⁴⁷
W5W	4500	13000	3.5×10 ⁴⁷
W5NW	5300	18000	6.3×10 ⁴⁷
W5NWpc	15000	50000	1.6×10 ⁴⁸
W5SW	790	3000	1.1×10 ⁴⁷
W5S	320	790	1.9×10 ⁴⁶
Inactive1	1400	3500	8.7×10 ⁴⁶
Inactive2	3100	9900	3.2×10 ⁴⁷
empty	340	1600	7.8×10 ⁴⁶

8

**Figure 13.** Spatially averaged spectra of the individual regions analyzed. ¹²CO 3-2 is shown by thick black lines and ¹³CO 1-0 is shown by thin red lines. Gaussian fits are overplotted in blue and green dashed lines, respectively. The fit properties are given in Table 1.

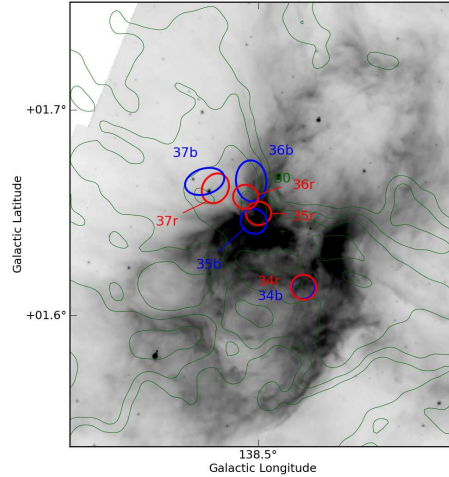


Figure 14. Small scale map of the Sh 2-201 region plotted with CO 3-2 contours integrated from -60 to -20 km s^{-1} at levels $3, 7.2, 17.3, 41.6$, and 100 K km s^{-1} . The IRAC $8 \mu\text{m}$ image is displayed in inverted log scale from 800 to 8000 MJy sr^{-1} . Contours of the CO 3-2 cube integrated from -60 to -20 km s^{-1} are overlaid at logarithmically spaced levels from 3 to 100 K km s^{-1} ($3.0, 7.2, 17.3, 41.6, 100$; $\sigma \approx 0.7 \text{ K km s}^{-1}$). The ellipses represent the individual outflow lobe apertures mentioned in Section 3.1.2.

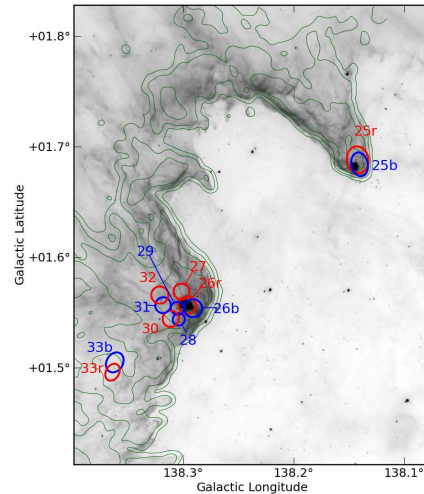


Figure 15. Small scale map of the AFGL 4029 region plotted with CO 3-2 contours integrated from -60 to -20 km s^{-1} at levels $3, 7.2, 17.3, 41.6$, and 100 K km s^{-1} . The IRAC $8 \mu\text{m}$ image is displayed in inverted log scale from 800 to 8000 MJy sr^{-1} . Contours of the CO 3-2 cube integrated from -60 to -20 km s^{-1} are overlaid at logarithmically spaced levels from 3 to 100 K km s^{-1} ($3.0, 7.2, 17.3, 41.6, 100$; $\sigma \approx 0.7 \text{ K km s}^{-1}$). Outflows 26-32 are ejected from a forming dense cluster. A diagram displaying the kinematics of the northern cometary cloud is shown in Figure 16.

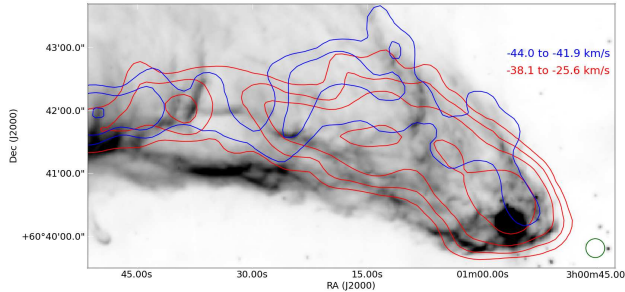


Figure 16. The northeast cometary cloud. Contours are shown at 0.5,1,2, and 5 K km s^{-1} integrated over the ranges -44.0 to -41.9 km s^{-1} (blue) and -38.1 to -35.6 km s^{-1} (red). There is a velocity gradient across the tail, suggesting that the front edge is being pushed away along the line of sight.

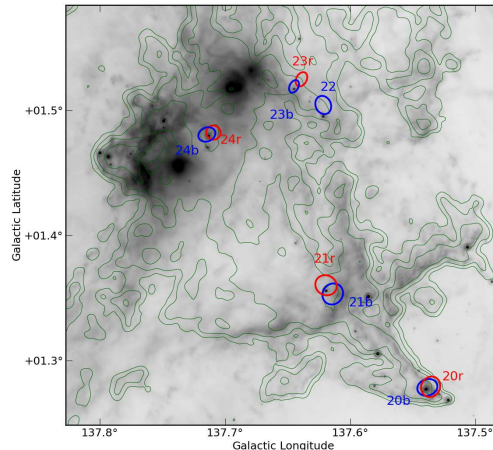


Figure 17. Small scale map of the LW Cas nebula plotted with CO 3-2 contours integrated from -60 to -20 km s^{-1} at levels 3,7,2,17,3,41,6, and 100 K km s^{-1} . The feature containing outflows 20 and 21 is the X-shaped ridge referenced in Section 4.3. This sub-region is notable for having very few outflows associated with the most significant patches of CO emission. The gas around it is heated on the left side by the O7V star HD 18326 ($D_{proj} = 8.5 \text{ pc}$), suggesting that this gas could be substantially warmer than the other molecular clouds in W5.

is an active outflow at the head of this cloud, we use 0.5 MYr as an upper limit. The approximate distance from this source to the cloud front behind it is $\sim 3.3 \text{ pc}$. If we assume the cloud front has been pushed at a constant speed $v \leq c_{II} \approx 10 \text{ km s}^{-1}$, we derive a lower limit on its age of 0.3 MYr. While these limits allow for the protostar to be older than the compression front by up to 0.2 MYr, it is likely that the compression front moved more slowly (e.g., 3 km s^{-1} if it was pushed by a D-type shock front) and that the protostar is not yet at the end of its lifetime - it is very plausible that this source was born in a radiation-driven implosion.

4.4 Southern Pillars

There are 3 cometary clouds that resemble the “elephant trunk” nebula in IC 1396 (Figure 19). Each of these pillars contains evidence of at least one outflow in the head of the cloud (see the supplementary materials, outflows 16-19 and 38) These pillars are low-mass and isolated; there is no other outflow activity in southern W5. However, because of the

bright illumination on their northern edges and robust star formation tracers, these objects present a reasonable case for triggered star formation by the RDI mechanism.

The kinematics of these cometary clouds suggest that they have been pushed in different directions by the HII region (Figure 19). The central cometary cloud (Figure 19b) has two tails. The southwest tail emission peaks around -39.5 km s^{-1} and the southeast tail peaks at -41.5 km s^{-1} , while the head is peaked at an intermediate -40.5 km s^{-1} . These velocity shifts suggest that the gas is being accelerated perpendicular to the head-tail axis and that the southeast tail is on the back side of the cometary head, while the southwest tail is on the front side. The expanding HII region is crushing this head-tail system.

The southeast cometary cloud (Figure 19a) peaks at -35.0 km s^{-1} . There are no clearly-separated CO tails as in the central cloud, but there is a velocity shift across the tail, in which the west (right) side is blueshifted compared to the east (left) side, which is the opposite sense from the central cometary cloud.

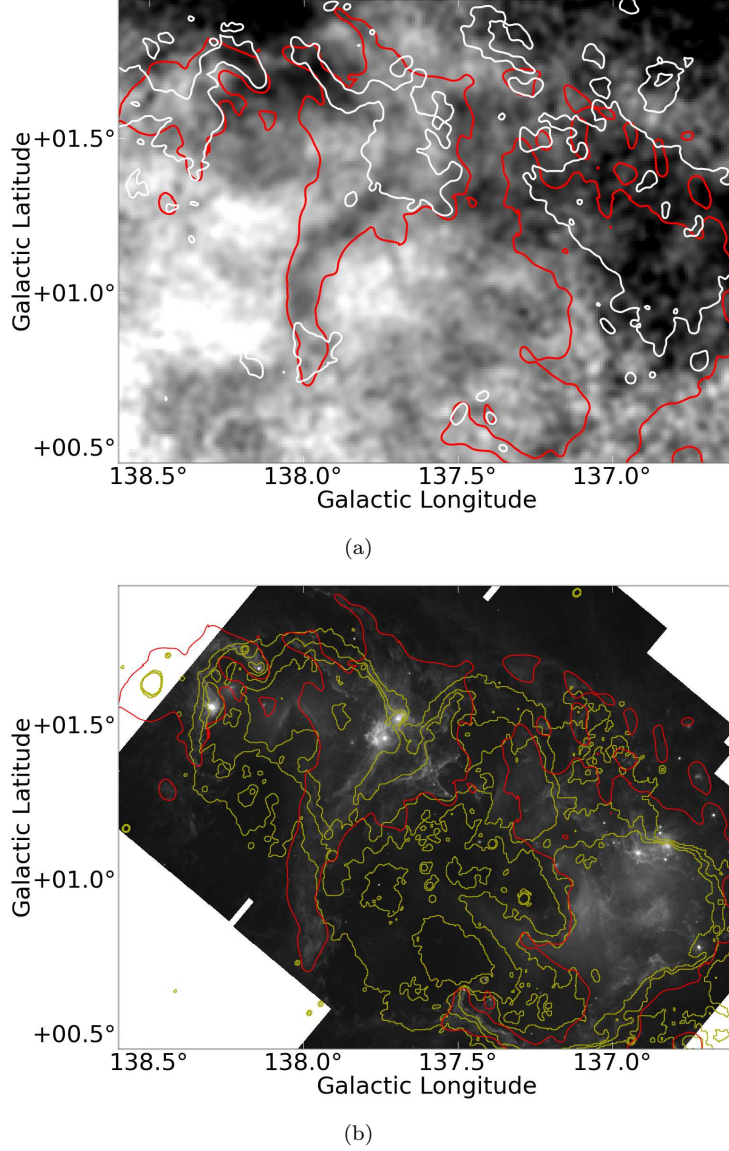


Figure 18. *Top:* The DRAO 21 cm HI map integrated from -45 to -35 km s⁻¹ displayed in grayscale from 700 (black) to 1050 (white) K km s⁻¹ with IRAS 100 μm contours (red, 40 MJy sr⁻¹) and ¹²CO 1-0 contours integrated over the same range (white, 4 K km s⁻¹) overlaid. The ridge of IRAS 100 μm emission at $\ell = 138.0$ coincides with a relative lack of HI emission at these velocities, suggesting either that there is less or colder gas along the ridge. *Bottom:* The Spitzer 24 μm map with 21 cm continuum contours at 6, 8, and 10 MJy sr⁻¹ overlaid. The IRAS contours are also overlaid to provide a reference for comparing the two figures and to demonstrate that the HII region abuts the cold-HI area. The moderate excess of continuum emission implies a somewhat higher electron density along the line of sight through the ridge.

The southwest cometary cloud (Figure 19c) peaks at -40.3 km s^{-1} and has weakly defined tails similar to the central cloud. Both of its tails are at approximately the same velocity (-42.5 km s^{-1}).

The kinematics of these tails provide some hints of their 3D structure and location in the cloud. Future study to compare the many cometary flows in W5 to physical models and simulations is warranted. Since these flows are likely at different locations along the line of sight (as required for their different velocities), analysis of their ionized edges may allow for more precise determination of the full 3D structure of the clouds relative to their ionizing sources.

4.5 W5 Southeast

The region identified as W5SE has very little star formation activity despite having significant molecular gas ($M_{^{13}\text{CO}} \sim 800 M_\odot$). While there are two outflows and two Class I objects (Koenig et al. 2008) in the southeast of the two clumps ($\ell = 138.15, b = 0.77$, Figure 20), the main clump ($\ell = 138.0, b = 0.8$) has no detected outflows. The CO emission is particularly clumpy in this region, with many independent, unresolved clumps both in position and velocity. In the 8 and 24 micron Spitzer images, it is clear that these clouds are illuminated from the northwest. This region represents a case in which the expanding HII region has impacted molecular gas but has not triggered additional star formation. The high clump-to-clump velocity dispersion observed in this region may be analogous to the W5S cometary clouds (Section 4.4) but without condensed clumps around which to form cometary clouds.

4.6 W5 Southwest

There is an isolated clump associated with outflows in the southwest part of W5 (Figure 21) at $v_{LSR} \sim -45 \text{ km s}^{-1}$. While this clump is likely to be associated with the W5 region, it shows little evidence of interaction with the HII region. If it is eventually impacted by the expanding ionization front (i.e. if it is within the W5 complex), this clump will be an example of “revealed”, not triggered, star formation.

The other source in W5SW is a cometary cloud with a blueshifted head and redshifted tail (Figure 22; Outflow 13). The head contains a redshifted outflow; no blueshifted counterpart was detected (the velocity gradient displayed in Figure 22 is smaller than the outflow velocity and is also redshifted away from the head). The lack of a blueshifted counterpart may be because the flow is blowing into ionized gas where the CO is dissociated.

Because of its evident interaction with the HII region, this source is an interesting candidate for a non-protostellar outflow impersonator. However, because the head is blueshifted relative to the tail, we can infer that the head has been accelerated towards us by pressure from the HII region, implying that it is in the foreground of the cloud. Given this geometry, a radiation-driven flow would appear blueshifted, not redshifted, as the detected flow is. Additionally, the outflow is seen as fast as 7.5 km s^{-1} redshifted from the cloud, which is a factor of 2 too fast to be driven by radiation in a standard D-type shock. Finally, the

outflow velocity is much greater than seen in a simulation of a cometary cloud by Gritschneider et al. (2010), while the head-to-tail velocity gradient is comparable.

4.7 W5 West / IC 1848

There is a bright infrared source seen in the center of W5W (IRAS 02459+6029; Figure 23), but the nearest CO outflow lobe is $\approx 1 \text{ pc}$ away. The nondetection may be due to confusion in this area: there are two layers of CO gas separated by $\sim 5 \text{ km s}^{-1}$, so low-velocity outflow detection is more difficult. Unlike the rest of the W5 complex, this region appears to have multiple independent confusing components along the line of sight (Figure 13), and therefore the CO data provide much less useful physical information (multiple components are also observed in the ^{13}CO data, ruling out self-absorption as the cause of the multiple components).

4.8 W5 NW

The northwest cluster containing outflows 1-8 is at a slightly different velocity ($\sim -35 \text{ km s}^{-1}$) than the majority of the W5 cloud complex ($\sim -38 \text{ km s}^{-1}$; Figure 24), but it shares contiguous emission with the neighboring W5W region. It contains many outflows and therefore is actively forming stars (Figure 25). However, this cluster exhibits much lower CO brightness temperatures and weaker Spitzer 8 μm emission than the “bright-rimmed clouds” seen near the W5 O-stars. We therefore conclude that the region has not been directly impacted by any photoionizing radiation from the W5 O-stars.

The lack of interaction with the W5 O-stars implies that the star formation in this region, though quite vigorous, has not been directly triggered. Therefore not all of the current generation of star formation in W5 has been triggered on small or intermediate scales (e.g., radiation-driven implosion). Even the “collect and collapse” scenario seems unlikely here, as the region with the most outflows also displays some of the smoothest morphology (Figures 2 and 25); in “collect and collapse” the expansion of an HII region leads to clumping and fragmentation, and the spaces between the clumps should be relatively cleared out.

5 DISCUSSION

5.1 Comparison to other outflows

The outflow properties we derive are similar to those in the B0-star forming clump IRAS 05358+3543 ($M \approx 600 M_\odot$ Ginsburg et al. 2009), in which CO 3-2 and 2-1 were used to derive outflow masses in the range $0.01\text{--}0.09 M_\odot$. However, some significantly larger outflows, up to 1.6 pc in one direction were detected, while the largest resolved outflow in our survey was only 0.8 pc (one direction).

As noted in Section 3.1.1, the total molecular mass in W5 is larger than Perseus, $M_{\text{W5}} \sim 4.5 \times 10^4 M_\odot$ while $M_{\text{Perseus}} \sim 10^4 M_\odot$ (Bally et al. 2008). The length distribution of outflows (Figure 8) is strikingly similar, while other physical properties have substantially different mean values with or without correction factors included.

The W5NW region is more directly comparable to

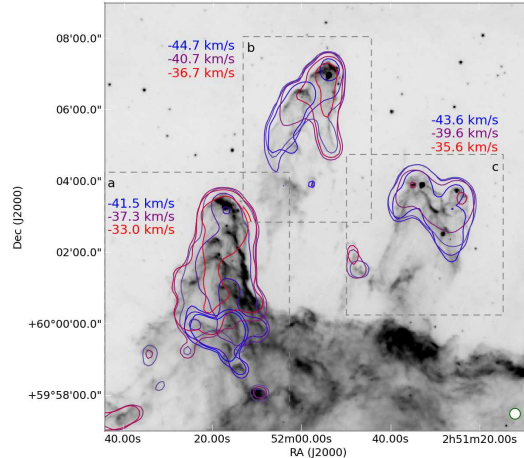


Figure 19. CO 3-2 contours overlaid on the Spitzer 8 μm image of the W5S cometary clouds described in Section 4.4. Contours are color-coded by velocity and shown for 0.84 km s^{-1} channels at levels of 1 K (a, b) and 0.5 K (c). The velocity ranges plotted are (a) -41.5 to -33.0 km s^{-1} (b) -44.7 to -36.7 km s^{-1} (c) -43.6 to -35.6 km s^{-1} . The labels show the minimum, maximum, and middle velocities to guide the eye. The grey boxes indicate the regions selected for CO contours; while there is CO emission associated with the southern 8 μm emission, we do not display it here. The velocity gradients are discussed in Section 4.4.

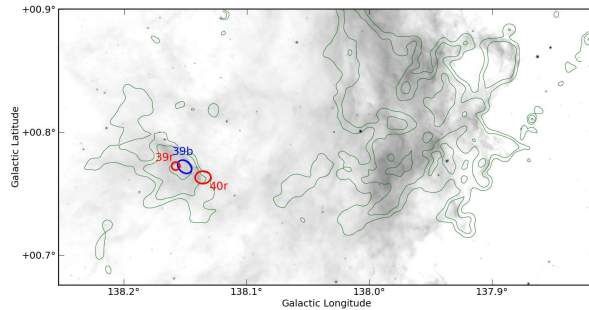


Figure 20. Small scale map of the W5 SE region showing the star-forming clump containing outflows 39 and 40 and the non-star-forming clump at $\ell = 138.0, b = 0.8$. CO 3-2 contours integrated from -60 to -20 km s^{-1} are displayed at levels 3, 7.2, 17.3, 41.6, and 100 K km s^{-1} .

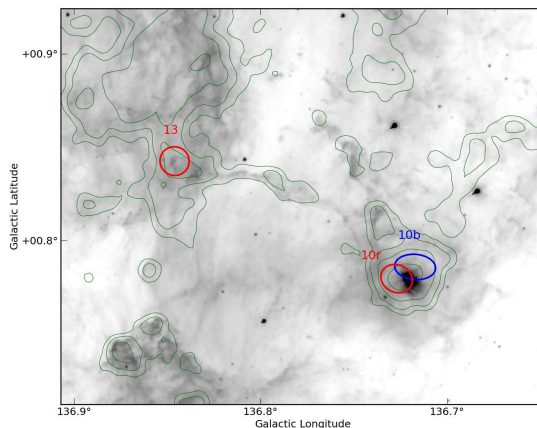


Figure 21. Small scale map of the W5 SW region plotted with CO 3-2 contours integrated from -60 to -20 km s^{-1} at levels 3, 7.2, 17.3, 41.6, and 100 K km s^{-1} . Outflow 13 is at the head of a cometary cloud (Figure 22) and therefore has clearly been affected by the expanding HII region, but the region including bipolar Outflow 10 shows no evidence of interaction with the HII region.

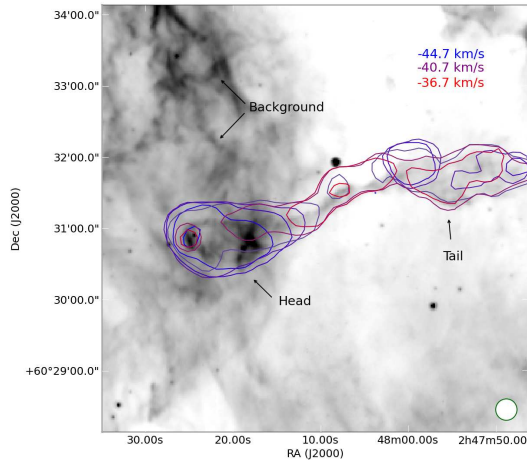


Figure 22. The cometary cloud in the W5 Southwest region (Outflow 13). Contours are shown at 1 K for 0.84 km s⁻¹ wide channels from -37.2 km s⁻¹ (blue) to -30.5 km s⁻¹ (red). The head is clearly blueshifted relative to the tail and contains a spatially unresolved redshifted outflow.

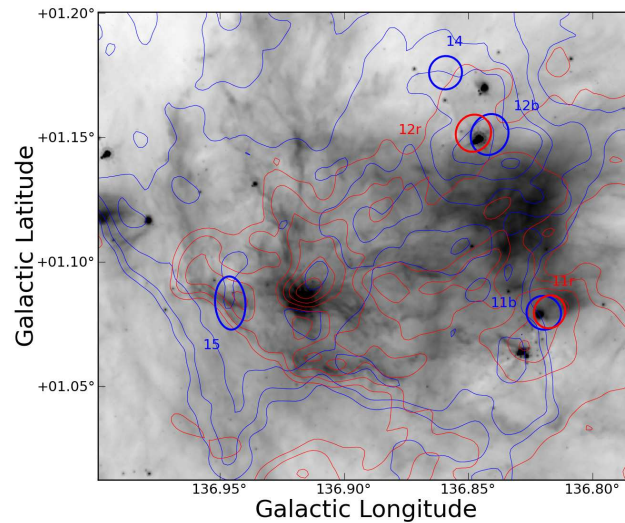


Figure 23. Small scale map of the W5 W region. The IRAC 8 μm image is displayed in inverted log scale from 800 to 8000 MJy sr⁻¹. Contours of the CO 3-2 cube integrated from -50 to -38 km s⁻¹ (blue) and -38 to -26 km s⁻¹ (red) are overlaid at levels 5,10,20,30,40,50,60 K km s⁻¹ $\sigma \approx 0.5$ K km s⁻¹. The lack of outflow detections is partly explained by the two spatially overlapping clouds that are adjacent in velocity.

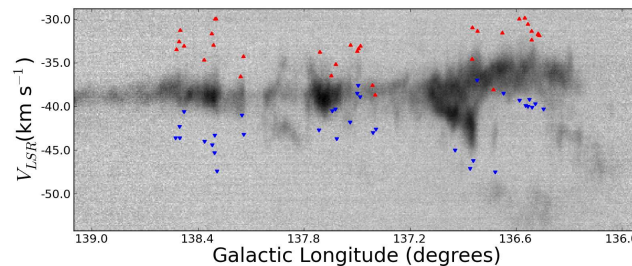


Figure 24. Integrated longitude-velocity diagram of the W5 complex from $b = 0.25$ to $b = 2.15$ in ^{12}CO 1-0 from the FCRAO OGS. The W5NW region is seen at a distinct average velocity around $\ell = 136.5$, $v_{\text{LSR}} = -34$ km s⁻¹. The red and blue triangles mark the longitude-velocity locations of the detected outflows. In all cases, they mark the low-velocity start of the outflow.

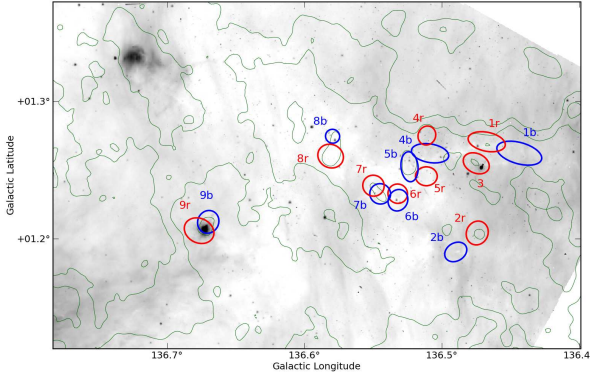


Figure 25. Small scale map of the W5 NW region plotted with CO 3-2 contours integrated from -60 to -20 km s^{-1} at levels 3, 7, 2, 17, 3, 41, 6, and 100 K km s^{-1} . Despite its distance from the W5 O-stars, $D_{proj} \approx 20$ pc, this cluster is the most active site of star formation in the complex as measured by outflow activity.

Perseus, with a total mass of $\sim 1.5 \times 10^4 M_\odot$ (Table 1) and a similar size. In Figure 3, we show both the W5NW region, which contains all of the identified outflows, and the W5NWpc region, which is a larger area intended to be directly comparable in both mass and spatial scale to the Perseus molecular cloud. The W5NWpc region contains more than an order of magnitude more turbulent energy than the Perseus complex ($E_{turb,Per} = 1.6 \times 10^{46}$ ergs, Arce et al. 2010) despite its similar mass. Even the smaller W5NW region has $\sim 5\times$ more turbulent energy than the Perseus complex, largely because of the greater average line width ($\sigma_{FWHM,W5NW} \approx 3.5$ km s^{-1}). As with the whole of W5, there is far too much turbulent energy in W5NW to be provided by outflows alone, implying the presence of another driver of turbulence.

Figure 26 shows the W5NWpc region and Perseus molecular cloud on the same scale, though in two different emission lines. The Perseus cloud contains many more outflows and candidates (70 in Perseus vs. 13 in W5NWpc) despite a much larger physical area surveyed in W5. While it is likely that many of the W5W outflows will break apart into multiple flows at higher resolution, it does not seem likely that each would break apart into 5 flows, as would be required to bring the numbers into agreement. Since the highest density of outflows in Perseus is in the NGC 1333 cloud, it may be that there is no equivalently evolved region in W5NWpc. The W5W region may be comparably massive, but it is also confused and strongly interacting with the W5 HII region - either star formation is suppressed in this region, or outflows are rendered undetectable. In the latter case, the most likely mechanisms for hiding outflows are molecular dissociation by ionizing radiation and velocity confusion.

Another possibility highlighted in Figure 26 is that the W5NW region is interacting with the W4 bubble. The cloud in the top right of Figure 26 is somewhat cometary, has higher peak brightness temperature, and is at a slightly different velocity (-45 km s^{-1}) than W5NW. The velocity difference of ~ 8 km s^{-1} could simply be two clouds physically unassociated along the line of sight, or could indicate the presence of another expanding bubble pushing two sheets of gas away from each other. Either way, the northwest por-

tion of the W5NW region is clumpier than the area in which the outflows were detected, and it includes no outflow detections.

5.2 Star Formation Activity

CO outflows are an excellent tracer of ongoing embedded star formation (e.g. Shu et al. 1987). We use the locations of newly discovered outflows to qualitatively describe the star formation activity within the W5 complex and evaluate the hypothesis that star formation has been triggered on small or intermediate scales.

Class 0/I objects are nearly always associated with outflows in nearby star-forming regions (e.g. Perseus Curtis et al. 2010; Hatchell et al. 2007). However, Koenig et al. (2008) detected 171 Class I sources in W5 using Spitzer photometry. Since our detection threshold for outflow appears to be similar to that in Perseus (Section 3.1.1), the lower number of outflow detections is surprising, especially considering that some of the detected outflows are outside the Spitzer-MIPS field (MIPS detections are required for Class I objects, and flows 1-4 are outside that range) or are in the outer arm (flows 39-54). Additionally, we should detect outflows from Class 0 objects that would not be identified by Spitzer colors.

There are a number of explanations for our detection deficiency. The Class I objects detected within the HII region “bubble” most likely have outflows in which the CO is dissociated similar to jet systems in Orion (e.g. HH46/47, a pc-scale flow in which CO is only visible very near the protostar; Chernin & Masson 1991; Stanke et al. 1999). This hypothesis can be tested by searching for optical and infrared jets associated with these objects, which presumably have lower mass envelopes and therefore less extinction than typical Class I objects. Additionally, there are many outflow systems that are likely to be associated with clusters of outflows rather than individual outflows as demonstrated in Section 3.1.1, where we were able to identify fewer outflows when ‘observing’ the Perseus objects at a greater distance. There are 24 sources in the Koenig et al. (2008) Class I catalog within $15''$ (one JCMT beam at 345 GHz) of another, and in many cases there are multiple Koenig et al. (2008)

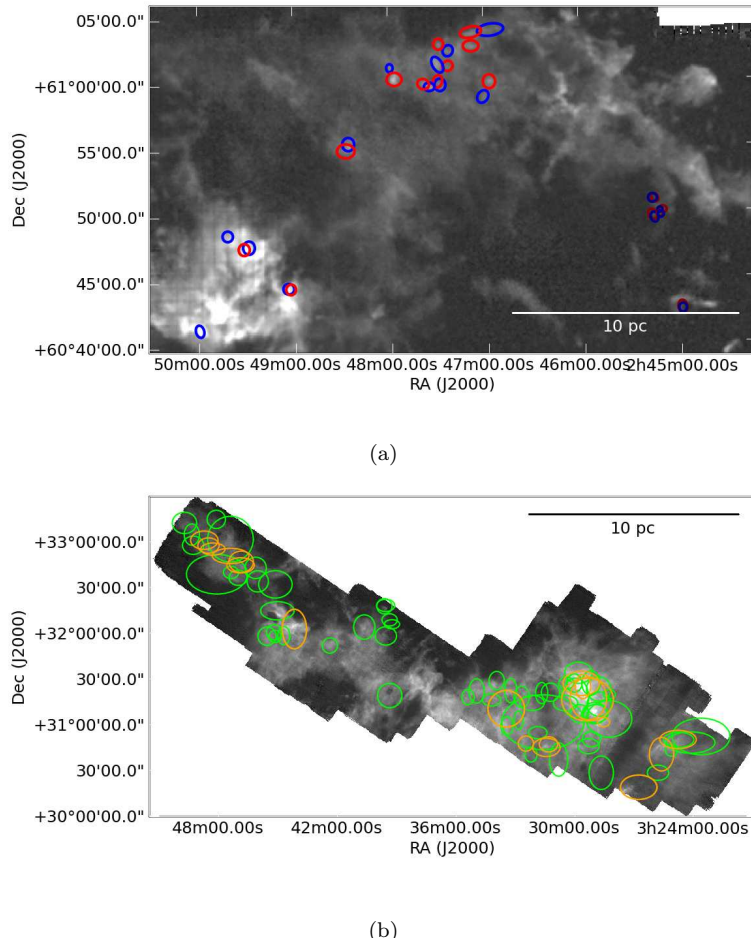


Figure 26. (a) An integrated CO 3-2 image of the W5W/NW region with ellipses overlaid displaying the locations and sizes of outflows. The dark red and blue ellipses in the lower right are associated with outer-arm outflows. W5W is the bottom-left, CO-bright region. W5NW is the top-center region containing the cluster of outflows. (b) An integrated CO 1-0 image of the Perseus molecular cloud from the COMPLETE survey (Arce et al. 2010). Note that the spatial scale is identical to that of (a) assuming that W5 is 8 times more distant than Perseus. The green ellipses represent Arce et al. (2010) CPOCs while the orange represent known outflows from the same paper.

Class I sources within the contours of a single outflow system.

5.3 Evaluating Triggering

In the previous section, we discussed in detail the relationship between each sub-region and the HII region. Some regions are observed to be star-forming but not interacting with the HII region (W5NW, Sh 2-201), while others are interacting with the HII region but show no evidence or reduced evidence of star formation (W5SE, W5W, LW Cas). At the very least, there is significant complexity in the triggering mechanisms, and no one mechanism or size scale is dominant. If we were to trust outflows as unbiased tracers of star formation, we might conclude that the majority of star formation in W5 is untriggered (spontaneous), but such a conclusion is unreliable because both radiatively triggered star formation and “revealed” star formation may not exhibit molecular outflows (although ionized atomic outflows should still be visible around young stars formed through these scenarios).

In Section 4.3, we analyzed a particular case in which the RDI mechanism could plausibly have crushed a cloud to create the observed protostar. It is not possible to determine whether interaction with the HII region was a necessary precondition for the star’s formation, but it at least accelerated the process. The other cometary clouds share this property, but in total there are only 5 cometary clouds with detected outflows at their tips, indicating that this mechanism is not the dominant driver of star formation in W5.

The ‘collect and collapse’ scenario might naively be expected to produce an excess of young stars at the interaction front between the HII region and the molecular cloud. However, because such interactions naturally tend to form instabilities, this scenario produces cloud morphologies indistinguishable from those of RDI. There is not an obvious excess of sources associated with cloud edges over those deep within the clouds (e.g., Figure 2). We therefore cannot provide any direct evidence for this triggering scenario.

The overall picture of W5 is of two concurrent episodes of massive-star formation that have lead to adjacent blown-out bubbles. Despite the added external pressure along the

central ridge, it is relatively deficient in both star formation activity and dense gas, perhaps because of heating by the strong ionizing radiation field. The lack of star formation along that central ridge implies that much of the gas was squeezed and heated, but it was not crushed into gravitationally unstable fragments. While some star formation may have been triggered in W5, there is strong evidence for pre-existing star formation being at least a comparable, if not the dominant, mechanism of star formation in the complex.

6 OUTFLOW SYSTEMS BEYOND W5

Fifteen outflows were detected at velocities inconsistent with the local W5 cloud velocities. Of these, 8 are consistent with Perseus arm velocities ($v_{LSR} > -55 \text{ km s}^{-1}$) and could be associated with different clouds within the same spiral arm. The other 7 have central velocities $v_{LSR} < -55 \text{ km s}^{-1}$ and are associated with the outer arm identified in previous surveys (e.g. Digel et al. 1996). The properties of these outflows are given in Tables 4 and 5; the distances listed are kinematic distances assuming $R_0 = 8.4 \text{ kpc}$ and $v_0 = 254 \text{ km s}^{-1}$ (Reid et al. 2009).

Of these outflows, all but one are within 2' of an IRAS point source. Outflow 54 is the most distant in our survey at a kinematic distance $d = 7.5 \text{ kpc}$ ($v_{lsr} = -75.6 \text{ km s}^{-1}$) and galactocentric distance $D_G = 14.7 \text{ kpc}$. It has no known associations in the literature.

Outflows 41 - 44 are associated with a cloud at $v_{LSR} \sim -62 \text{ km s}^{-1}$ known in the literature as LDN 1375 and associated with IRAS 02413+6037. Outflows 53 and 55 are at a similar velocity and associated with IRAS 02598+6008 and IRAS 02425+6000 respectively. All of these sources lie roughly on the periphery of the W5 complex.

Outflows 45 - 52 are associated with a string of IRAS sources and HII regions to the north of W5 and have velocities in the range $-55 < v_{LSR} < -45$. They therefore could be in the Perseus arm but are clearly unassociated with the W5 complex. Outflows 45 and 46 are associated with IRAS 02435+6144 and they may also be associated with the Sharpless HII region Sh 2-194. Outflows 47 and 48 are associated with IRAS 02461+6147, also known as AFGL 5085. Outflows 49 and 50 are nearby but not necessarily associated with IRAS 02475+6156, and may be associated with Sh 2-196. Outflows 51 and 52 are associated with IRAS 02541+6208.

7 CONCLUSIONS

We have identified 40 molecular outflow candidates in the W5 star forming region and an additional 15 outflows spatially coincident but located in the outer arm of the Galaxy.

- The majority of the CO clouds in the W5 complex are forming stars. Star formation is not limited to cloud edges around the HII region. Because star formation activity is observed outside of the region of influence of the W5 O-stars, it is apparent that direct triggering by massive star feedback is not responsible for all of the star formation in W5.

- The W5 complex is seen nearly face-on as evidenced by a strict upper limit on the CO column through the center of

the HII-region bubbles. It is therefore an excellent region to study massive star feedback and revealed and triggered star formation.

- Outflows contribute negligibly to the turbulent energy of molecular clouds in the W5 complex. This result is unsurprising near an HII region, but supports the idea that massive star forming regions are qualitatively different from low-mass star-forming regions in which the observed turbulence could be driven by outflow feedback. Even in regions far separated from the O-stars, there is more turbulence and less energy injection from outflows than in, e.g., Perseus.

- Despite detecting a significant number of powerful outflows, the total outflowing mass detected in this survey ($\sim 1.5 M_\odot$ without optical depth correction, perhaps 10–20 M_\odot when optical depth is considered) was somewhat smaller than in Perseus, a low to intermediate mass star forming region with $\sim 1/6$ the molecular mass of W5.

- The low mass measured may be partly because the CO 3-2 line is sub-thermally excited in outflows. Therefore, while CO 3-2 is an excellent tracer of outflows for detection, it does not serve as a ‘calorimeter’ in the same capacity as CO 1-0.

- Even considering excitation and optical depth corrections, it is likely that the mass of outflows in W5 is less than would be expected from a simple extrapolation from Perseus based on cloud mass. CO is likely to be photodissociated in the outflows when they reach the HII region, accounting for the deficiency around the HII region edges. However, in areas unaffected by the W5 O-stars such as W5NW, the deficiency may be because the greater turbulence in the W5 clouds suppresses star formation or hides outflows.

- Velocity gradients across the tails of many cometary clouds have been observed, hinting at their geometry and confirming that the outflows seen from their heads must be generated by protostars within.

- Outflows have been detected in the Outer Arm at galactocentric distances $\gtrsim 12 \text{ kpc}$. These represent some of the highest galactocentric distance star forming regions discovered to date.

8 ACKNOWLEDGEMENTS

We thank the two anonymous referees for their assistance in refining this document. We thank Devin Silvia for a careful proofread of the text. This work has made use of the APLpy plotting package (<http://aplpy.sourceforge.net>), the pyregion package (<http://leejjoon.github.com/pyregion/>), the agpy code package (<http://code.google.com/p/agpy/>), IPAC’s Montage (<http://montage.ipac.caltech.edu/>), the DS9 visualization tool (<http://hea-www.harvard.edu/RD/ds9/>), the pyspeckit spectroscopic analysis toolkit (<http://pyspeckit.bitbucket.org>), and the STARLINK package (<http://starlink.jach.hawaii.edu/>). IRAS data was acquired through IRSA at IPAC (<http://irsa.ipac.caltech.edu>). DRAO 21 cm data was acquired from the Canadian Astronomical Data Center (<http://cadcwww.hia.nrc.ca/cgps/>). The authors are supported by the National Science Foundation through NSF grant AST-0708403. This research has made use of the SIMBAD database, operated at CDS, Strasbourg, France.

Facilities: JCMT, VLA

REFERENCES

- Adams, F. C. & Fatuzzo, M. 1996, ApJ, 464, 256
- Arce, H. G., Borkin, M. A., Goodman, A. A., Pineda, J. E., & Halle, M. W. 2010, The Astrophysical Journal, 715, 1170
- Bachiller, R. 1996, ARA&A, 34, 111
- Bally, J., Walawender, J., Johnstone, D., Kirk, H., & Goodman, A. 2008, The Perseus Cloud, ed. Reipurth, B., 308–+
- Beaumont, C. N. & Williams, J. P. 2010, ApJ, 709, 791
- Bertoldi, F. & McKee, C. F. 1990, ApJ, 354, 529
- Bourke, T. L. et al. 1997, ApJ, 476, 781
- Bretherton, D. E., Moore, T. J. T., & Ridge, N. A. 2002, in Hot Star Workshop III: The Earliest Phases of Massive Star Birth, Vol. 267, 347
- Cabrit, S. & Bertout, C. 1990, ApJ, 348, 530
- Chernin, L. M. & Masson, C. R. 1991, ApJ, 382, L93
- Curtis, E. I., Richer, J. S., Swift, J. J., & Williams, J. P. 2010, MNRAS, 1304
- Cyganowski, C. J., Brogan, C. L., Hunter, T. R., & Churchwell, E. 2009, ApJ, 702, 1615
- Deharveng, L., Zavagno, A., Cruz-Gonzalez, I., Salas, L., Caplan, J., & Carrasco, L. 1997, A&A, 317, 459
- Digel, S. W., Lyder, D. A., Philbrick, A. J., Puche, D., & Thaddeus, P. 1996, ApJ, 458, 561
- Elmegreen, B. G. 1998, in Astronomical Society of the Pacific Conference Series, Vol. 148, Origins, ed. C. E. Woodward, J. M. Shull, & H. A. Thronson Jr., 150–+
- Elmegreen, B. G. & Lada, C. J. 1977, ApJ, 214, 725
- Enoch, M. L. et al. 2006, ApJ, 638, 293
- Evans, N. J. et al. 2009, ApJS, 181, 321
- Felli, M., Hjellming, R. M., & Cesaroni, R. 1987, A&A, 182, 313
- Garden, R. P., Hayashi, M., Hasegawa, T., Gatley, I., & Kaifu, N. 1991, ApJ, 374, 540
- Ginsburg, A. G., Bally, J., Yan, C., & Williams, J. P. 2009, ApJ, 707, 310
- Goldsmith, P. F. 1972, ApJ, 176, 597
- Gritschneider, M., Burkert, A., Naab, T., & Walch, S. 2010, ApJ, 723, 971
- Hachisuka, K. et al. 2006, ApJ, 645, 337
- Hatchell, J. & Dunham, M. M. 2009, 0904.1163
- Hatchell, J., Fuller, G. A., & Richer, J. S. 2007, Astronomy and Astrophysics, 472, 187
- Heyer, M. H., Brunt, C., Snell, R. L., Howe, J. E., Schloerb, F. P., & Carpenter, J. M. 1998, ApJS, 115, 241
- Karr, J. L. & Martin, P. G. 2003, Astrophysical Journal, 595, 900
- Klein, R. I., Sandford, II, M. T., & Whitaker, R. W. 1983, ApJ, 271, L69
- Koenig, X. P., Allen, L. E., Gutermuth, R. A., Hora, J. L., Brunt, C. M., & Muzerolle, J. 2008, Astrophysical Journal, 688, 1142
- Lada, C. J. & Fich, M. 1996, ApJ, 459, 638
- Lefloch, B., Lazareff, B., & Castets, A. 1997, Astronomy and Astrophysics, 324, 249
- Muenter, J. 1975, Journal of Molecular Spectroscopy, 55, 490, is always cited for $\mu = 0.122$ debye.
- Oey, M. S., Watson, A. M., Kern, K., & Walth, G. L. 2005, Astronomical Journal, 129, 393
- Peters, T., Banerjee, R., Klessen, R. S., Low, M. M., Galvn-Madrid, R., & Keto, E. R. 2010, The Astrophysical Journal, 711, 1017
- Reid, M. J. et al. 2009, ArXiv e-prints
- Reipurth, B. & Bally, J. 2001, Annual Review of Astronomy and Astrophysics, 39, 403
- Shu, F. H., Adams, F. C., & Lizano, S. 1987, ARA&A, 25, 23
- Snell, R. L., Carpenter, J. M., & Heyer, M. H. 2002, ApJ, 578, 229
- Stanke, T., McCaughrean, M. J., & Zinnecker, H. 1999, A&A, 350, L43
- Taylor, A. R. et al. 2003, AJ, 125, 3145
- Thompson, M. A., White, G. J., Morgan, L. K., Miao, J., Fridlund, C. V. M., & Huldtgren-White, M. 2004, Astronomy and Astrophysics, 414, 1017
- van der Tak, F. F. S., Black, J. H., Schöier, F. L., Jansen, D. J., & van Dishoeck, E. F. 2007, A&A, 468, 627
- Wilson, T. L., Rohlfs, K., & Hüttemeister, S. 2009, Tools of radio astronomy (Springer)

Table 2: CO 3-2 Outflow Measured Properties

Outflow Number	Latitude	Longitude	Ellipse Major "	Ellipse Minor "	Ellipse PA °	Velocity center (km s ⁻¹)	Velocity min (km s ⁻¹)	Velocity max (km s ⁻¹)	$\int T_A^* dv$ (K km s ⁻¹)	Bipolar? ^a
1b	136.4437	1.2622	60	27	342	-36.1	-47.6	-40.3	1.0	yc
1r	136.4674	1.2705	49	24	346	-36.1	-31.9	-23.4	1.5	yc
2b	136.4899	1.1904	30	23	299	-35.7	-48.0	-39.7	0.7	yc
2r	136.4743	1.2042	31	28	332	-35.7	-31.7	-23.0	1.3	yc
3	136.475	1.2548	35	25	332	-31.8	-31.8	-26.8	1.3	n
4b	136.5038	1.2623	26	22	35	-36.2	-44.1	-40.1	0.8	yu
4r	136.5109	1.2751	25	22	332	-36.2	-32.4	-28.6	0.9	yu
5r	136.5126	1.2453	24	22	10	-35.3	-31.4	-28.8	0.8	yu
5b	136.5236	1.2524	39	22	3	-35.3	-45.0	-39.2	1.4	yu
6b	136.532	1.228	28	25	332	-35.3	-44.8	-40.0	0.4	yc
6r	136.5327	1.2333	28	20	318	-35.3	-30.6	-24.0	1.0	yc
7b	136.5453	1.2318	24	19	332	-34.9	-47.5	-39.9	1.7	yc
7r	136.5506	1.2383	27	23	314	-34.9	-29.9	-22.7	1.3	yc
8b	136.5799	1.2755	18	14	332	-34.5	-41.5	-39.3	0.6	yc
8r	136.581	1.2601	34	30	332	-34.5	-29.6	-23.9	1.4	yc
9b	136.67	1.2123	30	27	332	-35.0	-44.5	-38.5	1.4	yc
9r	136.6766	1.2059	40	31	332	-35.0	-31.6	-26.7	0.3	yc
10b	136.7172	0.7859	39	24	353	-42.8	-52.6	-47.5	3.3	yc
10r	136.7271	0.7797	31	26	332	-42.8	-38.1	-33.1	4.1	yc
11b	136.8195	1.082	25	24	331	-34.2	-40.7	-37.0	3.1	yc
11r	136.8173	1.0799	24	22	331	-34.2	-31.4	-20.4	1.5	yc
12b	136.8414	1.1512	30	26	332	-40.4	-53.3	-46.2	1.5	yc
12r	136.8479	1.1517	27	25	332	-40.4	-34.6	-30.1	0.9	yc
13	136.8461	0.8426	28	27	332	-31.0	-31.0	-23.5	1.0	n
14	136.8591	1.176	24	23	332	-47.1	-54.5	-47.1	0.8	n
15	136.9443	1.0841	28	18	348	-45.0	-55.0	-45.0	3.1	n
16b	137.3929	0.5977	23	18	333	-40.7	-47.0	-42.6	0.7	yu
16r	137.3981	0.6121	22	19	357	-40.7	-38.7	-35.2	1.9	yu
17b	137.4084	0.6762	20	18	293	-40.3	-57.9	-43.0	2.3	yc
17r	137.412	0.6775	20	18	308	-40.3	-37.6	-30.4	1.1	yc
18b	137.4925	0.6289	16	15	333	-35.5	-39.2	-37.6	1.1	yc
18r	137.4908	0.6292	18	17	307	-35.5	-33.4	-31.0	2.0	yc
19b	137.4815	0.6409	20	17	1	-36.0	-41.9	-38.9	1.3	yc
19r	137.4798	0.6404	20	16	301	-36.0	-33.1	-25.9	0.7	yc
20r	137.5368	1.2792	24	21	332	-37.4	-33.0	-22.5	5.2	yc
20b	137.539	1.279	27	23	17	-37.4	-52.0	-41.8	3.4	yc
21b	137.6152	1.3543	31	28	322	-39.5	-52.0	-43.7	4.5	yc
21r	137.6169	1.3585	31	18	4	-39.5	-35.2	-30.0	1.2	yc
22	137.6213	1.506	27	21	293	-40.3	-46.0	-40.3	2.1	n
23b	137.6389	1.5251	21	14	331	-38.5	-42.5	-40.5	1.6	yc
23r	137.6449	1.5194	19	12	331	-38.5	-36.5	-32.0	1.9	yc
24r	137.7094	1.4824	20	20	331	-38.2	-33.8	-25.4	4.2	yc
24b	137.7146	1.4809	25	19	292	-38.2	-50.0	-42.7	4.4	yc
25b	138.1398	1.6858	39	26	282	-38.8	-49.5	-43.2	0.6	yc
25r	138.142	1.6884	43	35	11	-38.8	-34.3	-27.5	1.7	yc
26b	138.2913	1.5538	29	29	355	-38.7	-52.0	-47.4	1.2	yc
26r	138.2966	1.5564	28	28	330	-38.7	-30.0	-20.0	4.2	yc
27	138.3017	1.5689	26	25	330	-30.0	-30.0	-22.0	1.8	n
28	138.3042	1.5437	20	19	330	-43.3	-46.1	-43.3	1.4	n
29	138.3053	1.5537	22	20	330	-45.3	-51.6	-45.3	2.5	n
30	138.3115	1.5443	26	26	330	-33.0	-33.0	-29.2	1.2	n
31	138.3184	1.5566	26	25	330	-44.4	-49.1	-44.4	1.1	n

Continued on next page

Outflow Number	Latitude	Longitude	Ellipse Major "	Ellipse Minor "	Ellipse PA °	Velocity center (km s ⁻¹)	Velocity min (km s ⁻¹)	Velocity max (km s ⁻¹)	$\int T_A^* dv$ (K km s ⁻¹)	Bipolar? ^a
32	138.3213	1.5658	27	27	330	-31.7	-31.7	-27.0	1.4	n
33b	138.3618	1.5073	28	26	330	-39.4	-49.5	-44.0	1.3	yc
33r	138.3642	1.4959	29	21	330	-39.4	-34.7	-25.8	2.0	yc
34r	138.4779	1.6137	22	21	330	-36.9	-33.1	-29.1	0.5	yc
34b	138.4768	1.6142	21	20	330	-36.9	-43.6	-40.6	0.8	yc
35r	138.4998	1.6496	22	20	4	-37.5	-31.3	-24.1	1.4	yc
35b	138.5021	1.6458	23	21	330	-37.5	-49.5	-43.6	1.3	yc
36b	138.5034	1.6654	35	26	5	-37.5	-50.4	-42.3	1.2	yc
36r	138.5061	1.6576	22	21	330	-37.5	-32.6	-26.7	1.4	yc
37r	138.5208	1.6618	27	22	330	-38.5	-33.5	-31.4	0.6	yc
37b	138.5241	1.6667	23	23	18	-38.5	-47.0	-43.6	0.6	yc
38b	137.4983	0.6062	16	15	333	-36.1	-39.2	-38.5	0.8	yc
38r	137.4977	0.6055	15	14	307	-36.1	-33.7	-32.5	0.5	yc
39b	138.1506	0.7724	23	16	321	-38.8	-45.3	-41.0	2.0	yc
39r	138.1591	0.7713	17	13	304	-38.8	-36.6	-34.7	0.7	yc
40	138.1356	0.7634	22	18	4	-36.0	-36.0	-27.6	2.2	n

Measured properties of the outflows.

^a Is the outflow part of a bipolar pair? yc = yes, confident; yu = yes, uncertain; n = no

Outflow Number	Mass (M_{\odot})	Momentum ($M_{\odot} \text{km s}^{-1}$)	Energy (10^{42} ergs)	Dynamical Age (10^4 years)
-------------------	-------------------------	--	-----------------------------	-------------------------------------

1b	0.034	0.26	21.1	7.0
1r	0.04	0.24	17.3	7.0
2b	0.011	0.07	4.9	5.4
2r	0.025	0.17	13.0	5.4
3	0.025	0.12	5.8	-
4b	0.01	0.06	4.0	7.2
4r	0.011	0.04	1.8	7.2
5r	0.01	0.04	2.0	4.5
5b	0.025	0.14	8.0	4.5
6b	0.007	0.04	3.0	1.7
6r	0.013	0.09	6.8	1.7
7b	0.017	0.13	10.5	2.4
7r	0.018	0.13	9.7	2.4
8b	0.003	0.02	0.9	4.9
8r	0.032	0.2	13.2	4.9
9b	0.025	0.13	7.2	3.9
9r	0.009	0.04	1.8	3.9
10b	0.068	0.41	25.7	3.9
10r	0.074	0.45	28.0	3.9
11b	0.042	0.17	7.2	0.7
11r	0.017	0.09	5.9	0.7
12b	0.026	0.14	8.7	1.8
12r	0.014	0.13	12.7	1.8
13	0.016	0.1	5.8	-
14	0.01	0.06	4.1	-
15	0.036	0.24	17.3	-
16b	0.006	0.03	1.2	11.1
16r	0.018	0.05	1.3	11.1
17b	0.019	0.12	9.4	1.4
17r	0.009	0.03	0.7	1.4
18b	0.006	0.02	0.5	1.4
18r	0.013	0.04	1.0	1.4
19b	0.011	0.05	2.4	0.7
19r	0.005	0.01	0.2	0.7
20r	0.059	0.5	46.3	0.5
20b	0.047	0.33	26.6	0.5
21b	0.086	0.58	41.4	1.7
21r	0.014	0.08	4.3	1.7
22	0.027	0.1	4.3	-
23b	0.011	0.03	0.9	4.5
23r	0.01	0.03	1.0	4.5
24r	0.037	0.3	26.1	1.7
24b	0.047	0.28	18.3	1.7
25b	0.014	0.09	6.8	1.0
25r	0.056	0.35	23.0	1.0
26b	0.023	0.24	26.1	1.1
26r	0.072	0.85	106.0	1.1
27	0.026	0.09	4.5	-
28	0.012	0.07	4.6	-
29	0.024	0.06	2.1	-
30	0.018	0.12	8.0	-

Outflow Number	Mass (M_{\odot})	Momentum ($M_{\odot} \text{km s}^{-1}$)	Energy (10^{42} ergs)	Dynamical Age (10^4 years)
31	0.016	0.03	0.7	-
32	0.023	0.18	14.5	-
33b	0.022	0.14	10.1	3.0
33r	0.026	0.2	16.1	3.0
34r	0.005	0.03	1.7	0.7
34b	0.007	0.03	1.2	0.7
35r	0.013	0.12	11.6	1.3
35b	0.014	0.12	11.0	1.3
36b	0.025	0.19	15.8	2.7
36r	0.014	0.1	6.8	2.7
37r	0.008	0.04	1.6	2.1
37b	0.007	0.06	4.2	2.1
38b	0.005	0.01	0.4	0.9
38r	0.002	0.01	0.1	0.9
39b	0.017	0.07	2.8	7.5
39r	0.004	0.01	0.3	7.5
40	0.019	0.08	3.5	-

Derived properties of the outflows in the optically thin limit. Typical optical depth corrections for ${}^{12}\text{CO}$ 3-2 are in the range 7-14 (Curtis et al.

Table 4. Outer Arm CO 3-2 Outflows - Measured Properties

Outflow Number	Latitude	Longitude	Ellipse Major ''	Ellipse Minor ''	Ellipse PA °	Kinematic Distance (pc)	R_G^a (pc)	Velocity center (km s^{-1})	Velocity min	Velocity max	$\int T_A^* dv$ (K km s^{-1})
41r	136.364	0.9606	25	18	2	5510	13000	-61.8	-59.2	-56.5	0.5
41b	136.3634	0.9568	23	17	353	5510	13000	-61.8	-71.6	-64.3	3.0
42r	136.3522	0.9786	20	14	2	5500	12900	-62.1	-59.8	-57.6	0.6
42b	136.3548	0.9798	20	19	332	5500	12900	-62.1	-67.8	-64.4	0.5
43r	136.3495	0.9612	17	15	63	5510	13000	-61.8	-59.0	-56.1	0.8
43b	136.353	0.9621	12	12	333	5510	13000	-61.8	-66.3	-64.6	1.0
44r	136.3554	0.9576	13	13	23	5500	12900	-61.8	-59.0	-55.4	2.1
44b	136.3545	0.9567	14	14	333	5500	12900	-61.8	-68.0	-64.5	2.0
45r	136.1219	2.0816	34	25	297	3750	11400	-46.5	-43.1	-40.5	0.6
45b	136.1233	2.0803	35	25	306	3750	11400	-46.5	-57.3	-50.0	1.9
46	136.1166	2.0983	26	25	332	3790	11400	-50.2	-52.6	-50.2	0.5
47b	136.3857	2.2687	34	27	332	3220	11000	-42.0	-55.0	-46.7	3.5
47r	136.3861	2.267	35	23	304	3220	11000	-42.0	-37.3	-25.1	5.0
48b	136.374	2.2628	29	21	332	3250	11000	-43.2	-51.4	-47.0	1.5
48r	136.3736	2.2615	29	22	332	3250	11000	-43.2	-39.5	-22.2	8.9
49r	136.4663	2.4678	29	23	290	3610	11300	-45.7	-42.2	-33.0	2.2
49b	136.4661	2.4693	31	23	292	3610	11300	-45.7	-52.2	-49.1	0.9
50b	136.5087	2.5108	31	25	332	3380	11100	-43.5	-48.5	-46.5	0.8
50r	136.5118	2.5083	28	23	10	3380	11100	-43.5	-40.6	-37.5	1.0
51b	137.058	2.9858	28	23	293	4350	11900	-51.8	-55.5	-53.0	0.8
51r	137.0567	2.9864	34	25	8	4350	11900	-51.8	-50.6	-40.9	3.5
52r	137.0662	2.9999	37	26	43	4390	12000	-52.2	-49.1	-41.0	7.8
52b	137.0683	3.0013	38	29	15	4390	12000	-52.2	-65.8	-55.2	4.1
53b	138.6143	1.5611	26	26	330	5450	13000	-59.7	-71.1	-61.7	5.5
53r	138.6158	1.563	25	23	330	5450	13000	-59.7	-57.6	-54.5	1.3
54r	136.382	0.8392	29	20	343	7480	14700	-75.6	-73.2	-68.9	2.6
54b	136.3824	0.838	20	17	332	7480	14700	-75.6	-83.1	-77.9	2.0
55b	136.7623	0.4548	27	16	343	5230	12700	-60.9	-65.2	-62.7	5.4
55r	136.7579	0.4522	24	18	343	5230	12700	-60.9	-59.0	-53.2	6.0

9

^aGalactocentric Radius

9 ONLINE-ONLY SUPPLEMENT

In this supplement, we present position-velocity diagrams, contour overlays on infrared images, and integrated spectra for all of the outflows identified in the survey. The overlays are on Spitzer 4.5 μm and 8 μm images except where otherwise noted; the exceptions are because the CO 3-2 survey covered a larger area than the Spitzer survey. The contours are displayed at levels 0.5, 1, 1.5, 2, 3, 4, 5, 6 K km s^{-1} except where otherwise noted. The typical noise level in the contoured CO maps is $\sigma \approx 0.25$ K km s^{-1} .

Table 5. Outer Arm CO 3-2 Outflows - Derived Properties

Outflow Number	Mass (M_{\odot})	Momentum ($M_{\odot} \text{km s}^{-1}$)	Energy (10^{42} ergs)	Dynamical Age (10^4 years)	Momentum Flux $10^{-6} M_{\odot} \text{km s}^{-1} \text{yr}^{-1}$
41r	0.037	0.11	3.5	3.6	30.2
41b	0.196	0.96	54.6	3.6	30.2
42r	0.029	0.06	1.3	4.3	3.9
42b	0.03	0.11	3.9	4.3	3.9
43r	0.033	0.13	5.1	7.3	2.9
43b	0.024	0.08	2.8	7.3	2.9
44r	0.062	0.21	7.9	1.8	27.7
44b	0.067	0.28	12.6	1.8	27.7
45r	0.037	0.18	8.6	1.2	62.3
45b	0.126	0.55	28.3	1.2	62.3
46	0.028	0.1	3.7	-	-
47b	0.187	1.32	101.0	0.6	553.0
47r	0.232	1.84	164.0	0.6	553.0
48b	0.054	0.33	20.8	0.4	754.0
48r	0.341	2.4	229.0	0.4	754.0
49r	0.106	0.77	62.7	1.4	71.1
49b	0.047	0.22	10.8	1.4	71.1
50b	0.037	0.14	5.5	3.8	7.4
50r	0.038	0.14	5.5	3.8	7.4
51b	0.058	0.13	3.0	1.0	152.0
51r	0.303	1.33	72.7	1.0	152.0
52r	0.829	4.3	250.0	1.4	479.0
52b	0.472	2.5	150.0	1.4	479.0
53b	0.626	3.16	194.0	4.7	73.2
53r	0.124	0.31	8.5	4.7	73.2
54r	0.461	1.24	37.5	1.8	135.0
54b	0.212	1.14	64.0	1.8	135.0
55b	0.411	1.66	68.0	7.5	28.3
55r	0.404	0.47	6.6	7.5	28.3

10

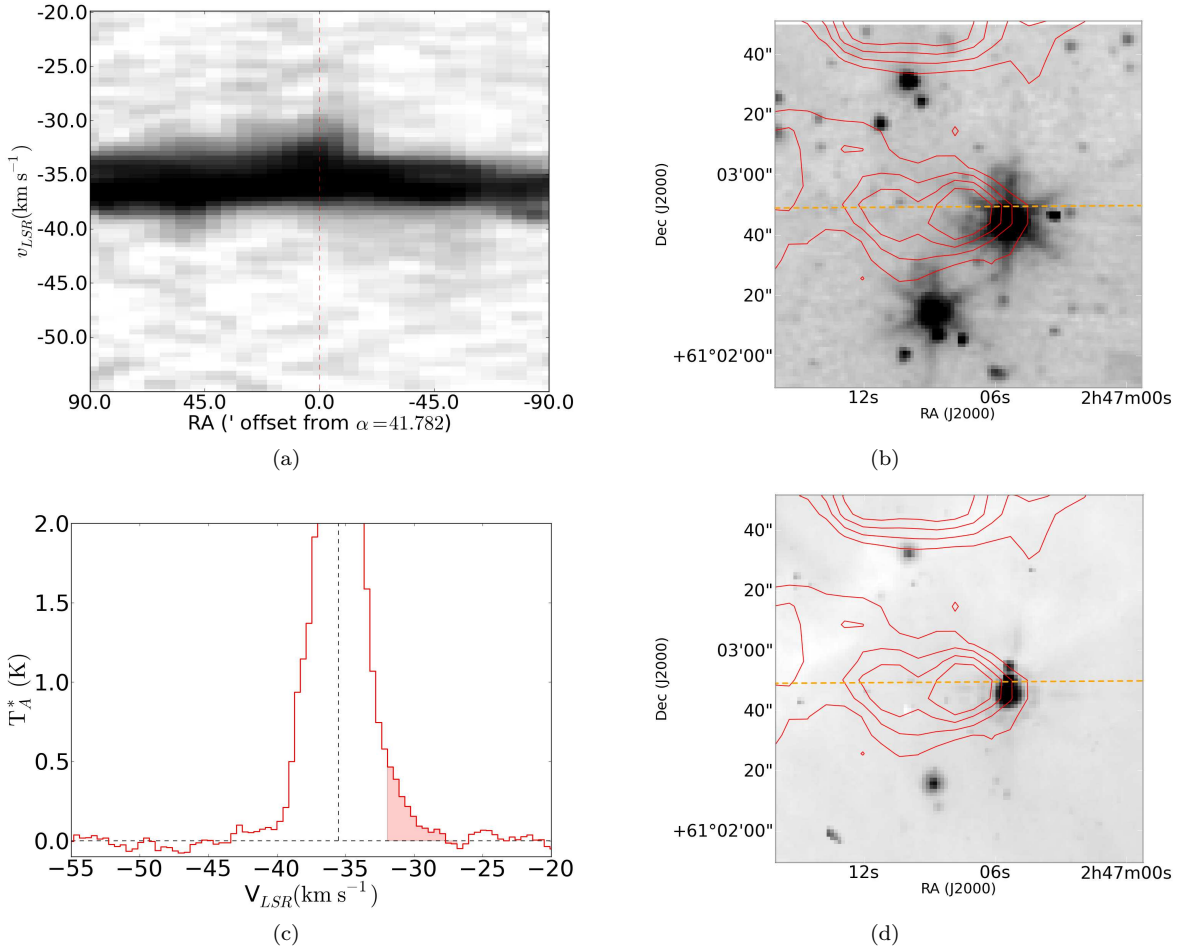


Figure 27. Position-velocity diagrams, spectra, and contour overlays of Outflow 3. No blue counterpart to this flow was identified, although it is possible that the blue lobe in Outflow 4 is actually associated with this source.

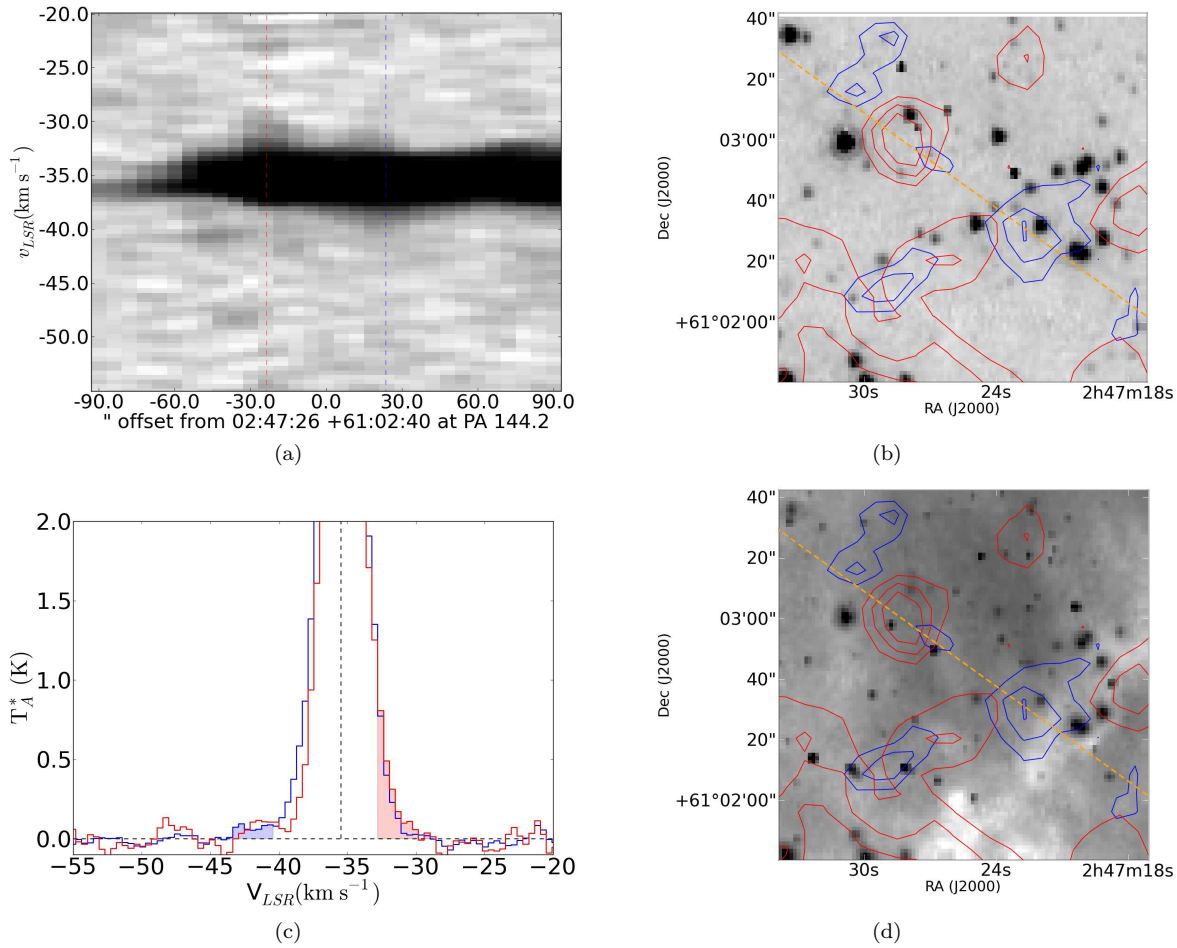


Figure 28. Position-velocity diagrams, spectra, and contour overlays of Outflow 4. While the red outflow is prominent and clear in the contours, the blue outflow is faint and somewhat spread out. This outflow pair is somewhat confused with outflows 3 and 5, which all seem to come from a cluster. Contours are shown at levels 0.5, 0.75, 1, 1.5, 2, 3, 4, 5, 6 K km s $^{-1}$ (blue) and 1, 1.5, 2, 3, 4, 5, 6 K km s $^{-1}$ (red).

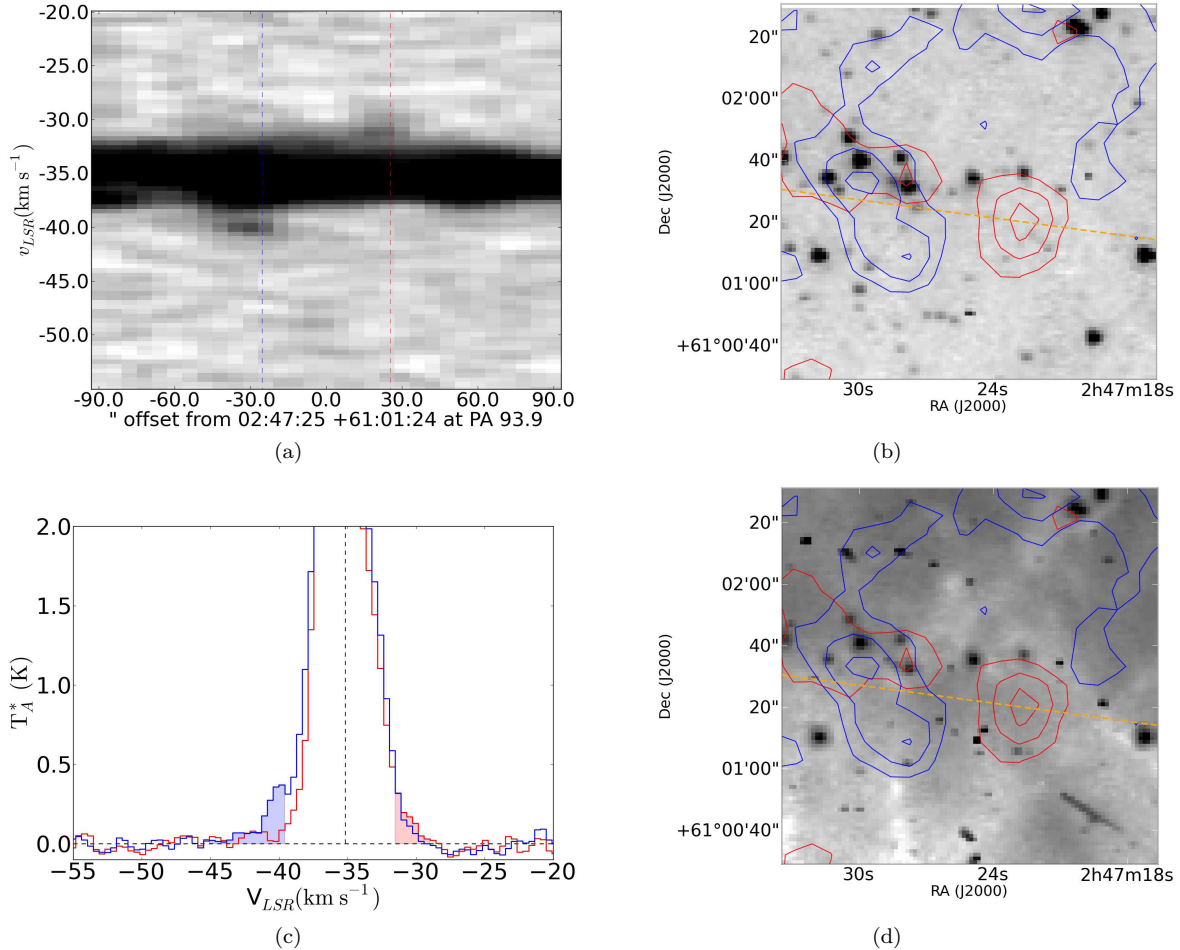


Figure 29. Position-velocity diagrams, spectra, and contour overlays of Outflow 5. The bipolar identification may be confused with Outflow 4.

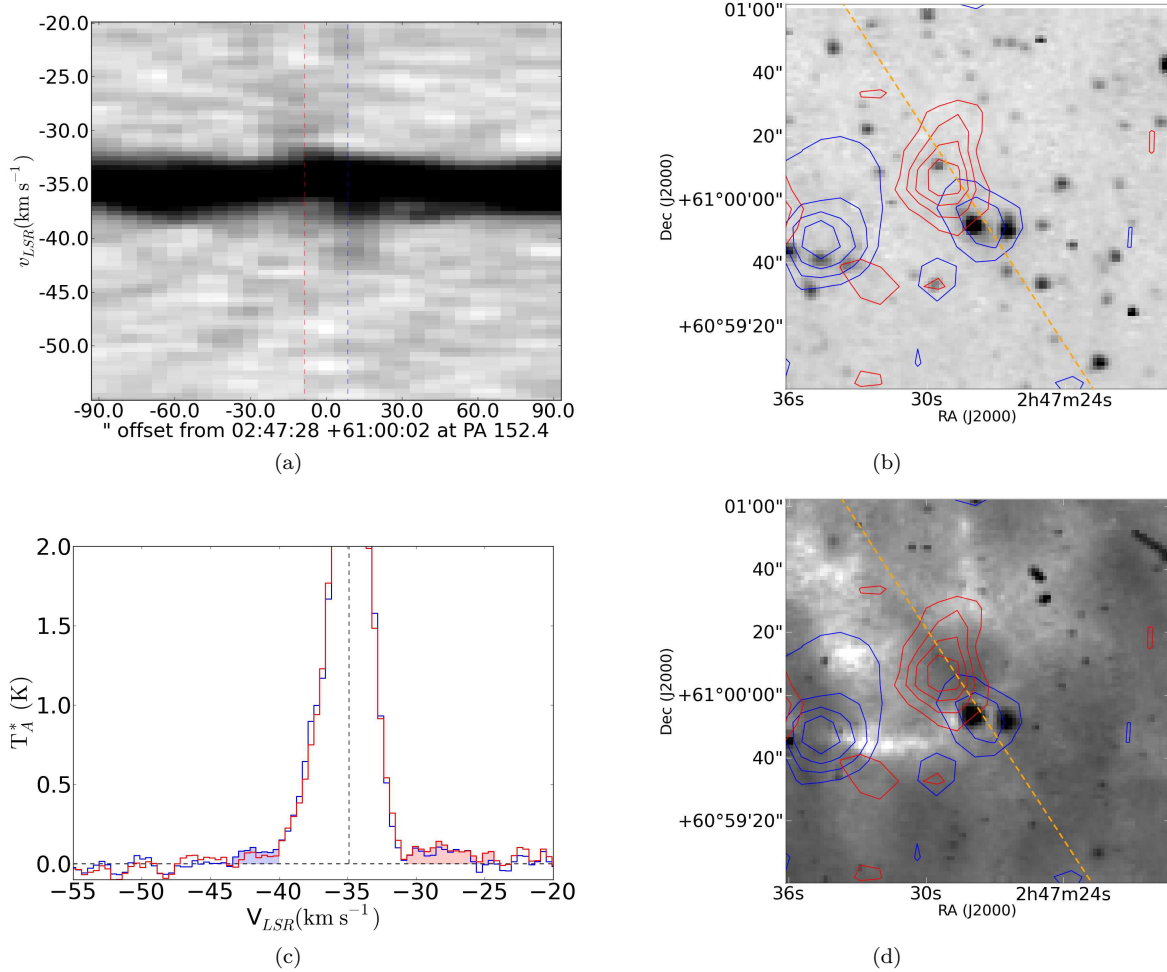


Figure 30. Position-velocity diagrams, spectra, and contour overlays of Outflow 6.

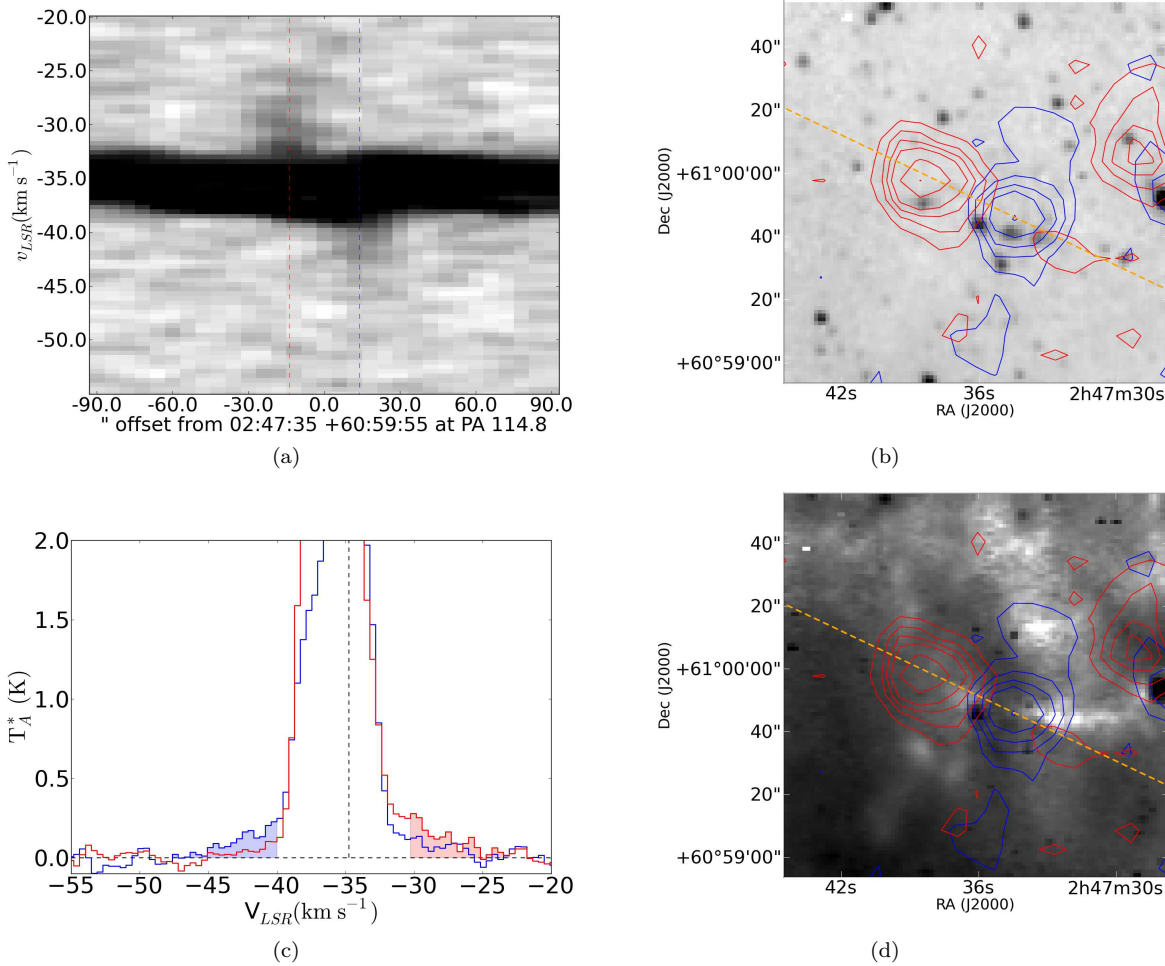


Figure 31. Position-velocity diagrams, spectra, and contour overlays of Outflow 7.

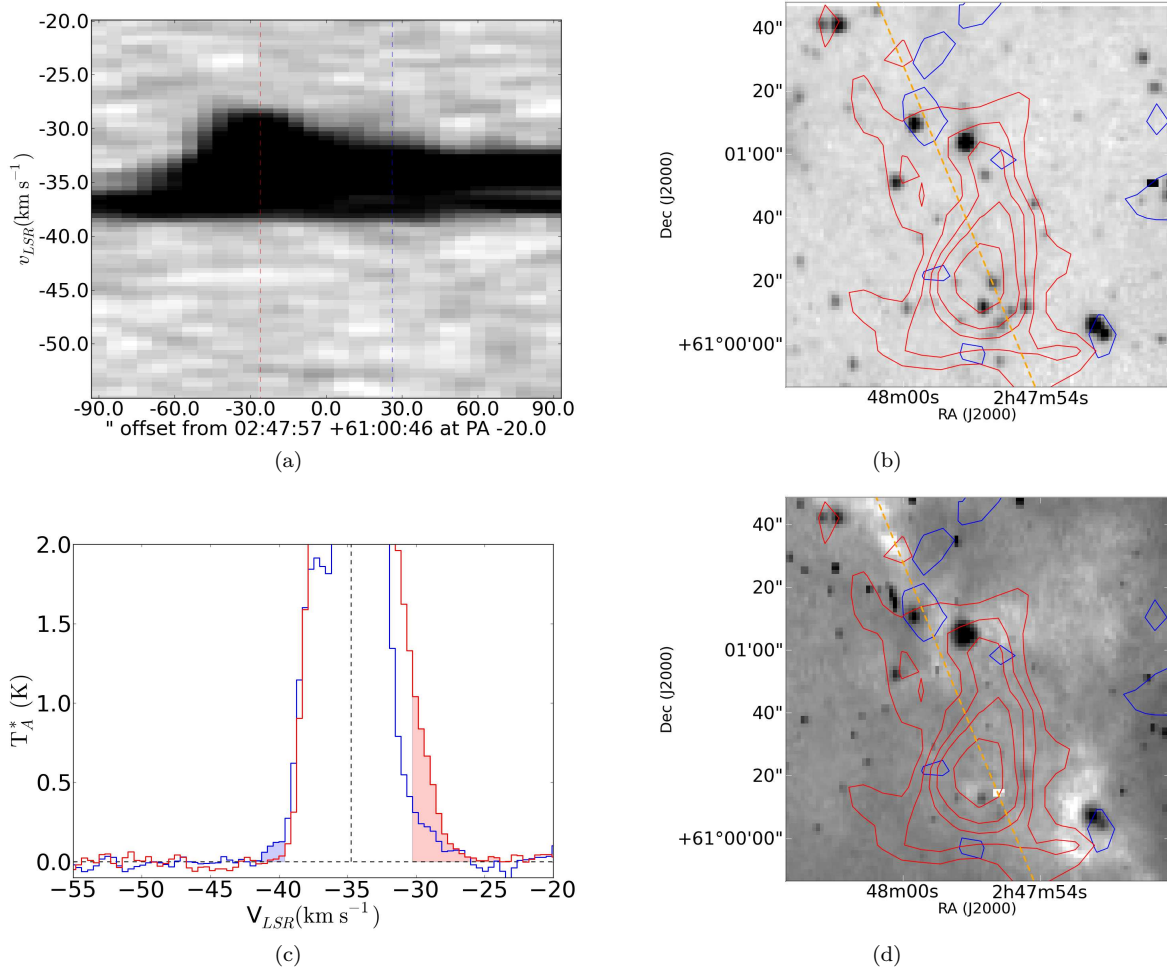


Figure 32. Position-velocity diagrams, spectra, and contour overlays of Outflow 8. While a red high-velocity line wing is quite clear, it is not obvious whether the tail is truly distinct from the molecular cloud. The blue line wing is more easily separated from the cloud, but is very faint. The reliability of the detection is reinforced by the faint $4.5\mu\text{m}$ wisp seen near the source at $2:47:57 +61:01:04$, which is suggestive of an H_2 outflow (Cyganowski et al. 2009). Contours are displayed at levels $0.25, 0.5, 1, 1.5, 2, 3, 4, 5, 6 \text{ K km s}^{-1}$ (blue) and $0.5, 1, 1.5, 2, 3, 4, 5, 6 \text{ K km s}^{-1}$ (red).

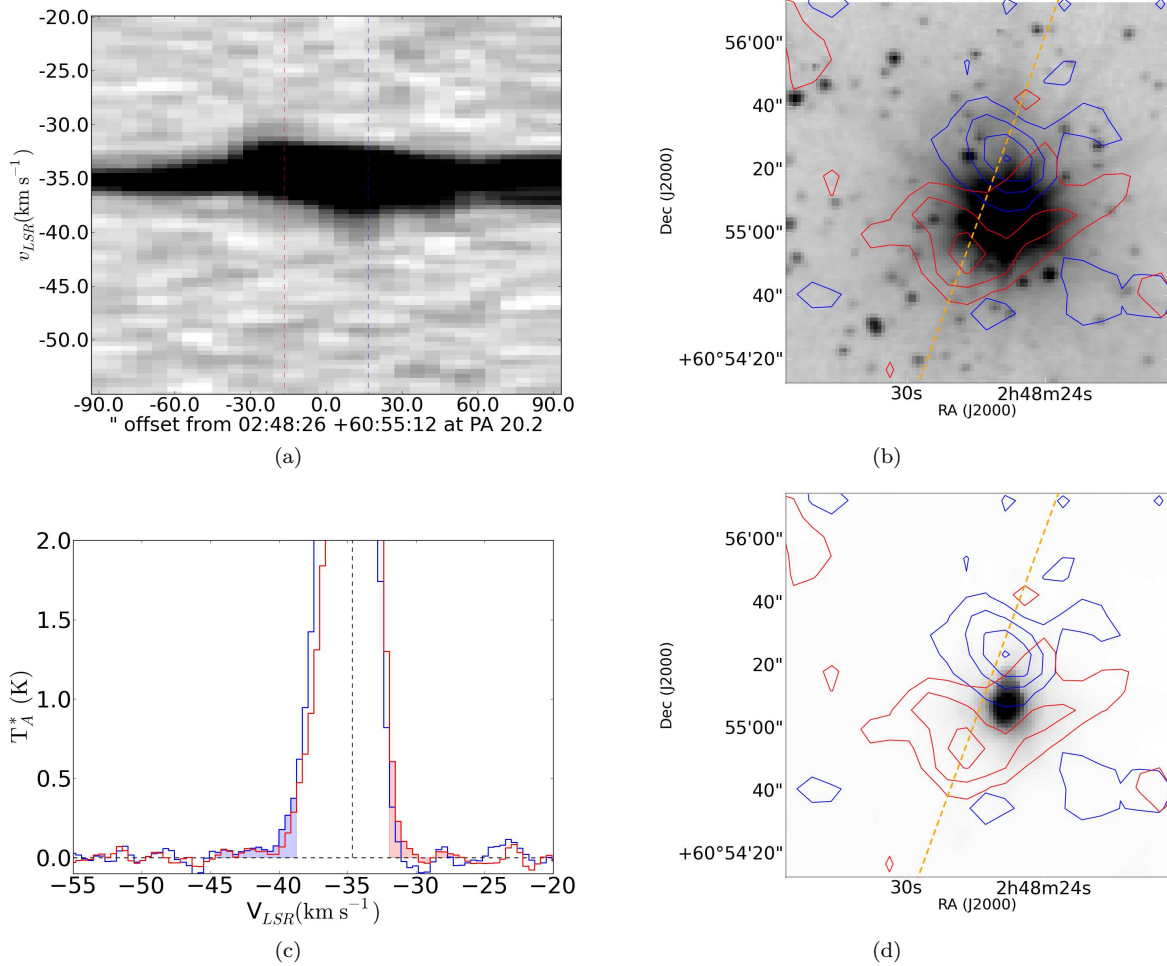


Figure 33. Position-velocity diagrams, spectra, and contour overlays of Outflow 9.

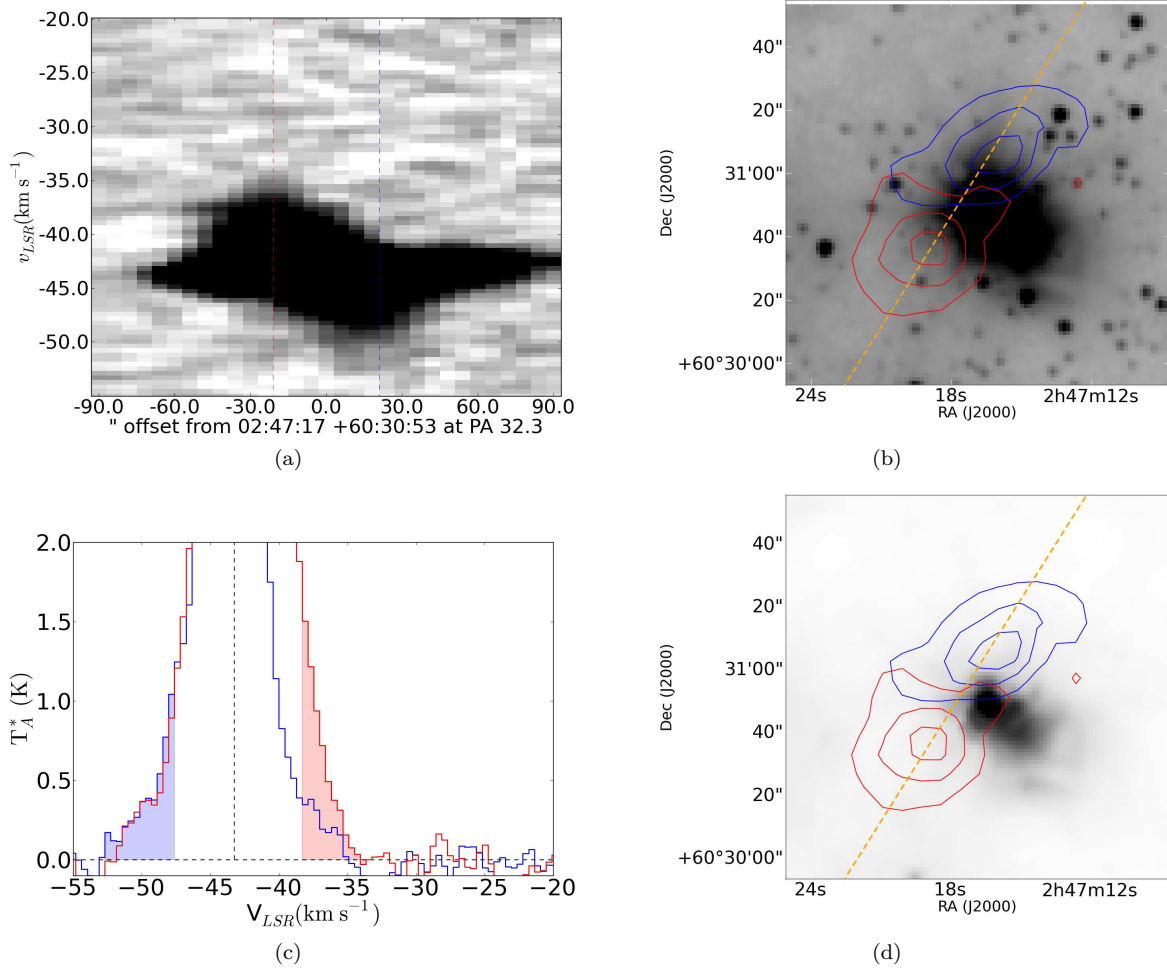


Figure 34. Position-velocity diagrams, spectra, and contour overlays of Outflow 10. This flow is isolated and bright, but has somewhat low-velocity wings, suggesting that it may have a low inclination angle. Contours are displayed at levels 2,4,6 K km s $^{-1}$.

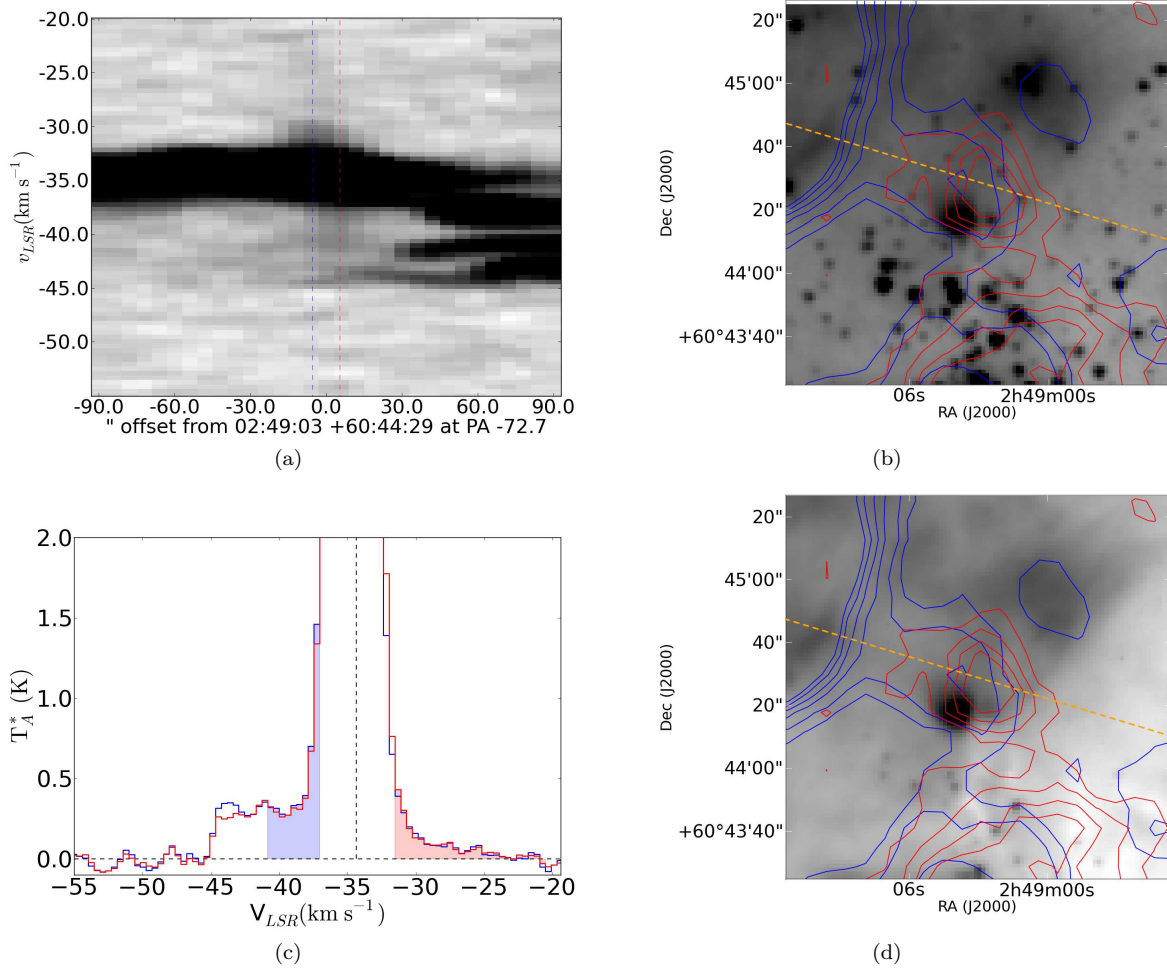


Figure 35. Position-velocity diagrams, spectra, and contour overlays of Outflow 11. The blue lobe is integrated over a limited range of velocities because of the extremely complex velocity distribution in the W5W complex that can be seen in the PV diagram (panel *a*). Nonetheless, the bipolar nature of the outflow is reasonably clear. Contours are displayed at levels $1.5, 2, 3, 4, 5, 6 \text{ K km s}^{-1}$ (blue) and $0.5, 1, 1.5, 2, 3, 4, 5, 6 \text{ K km s}^{-1}$ (red).

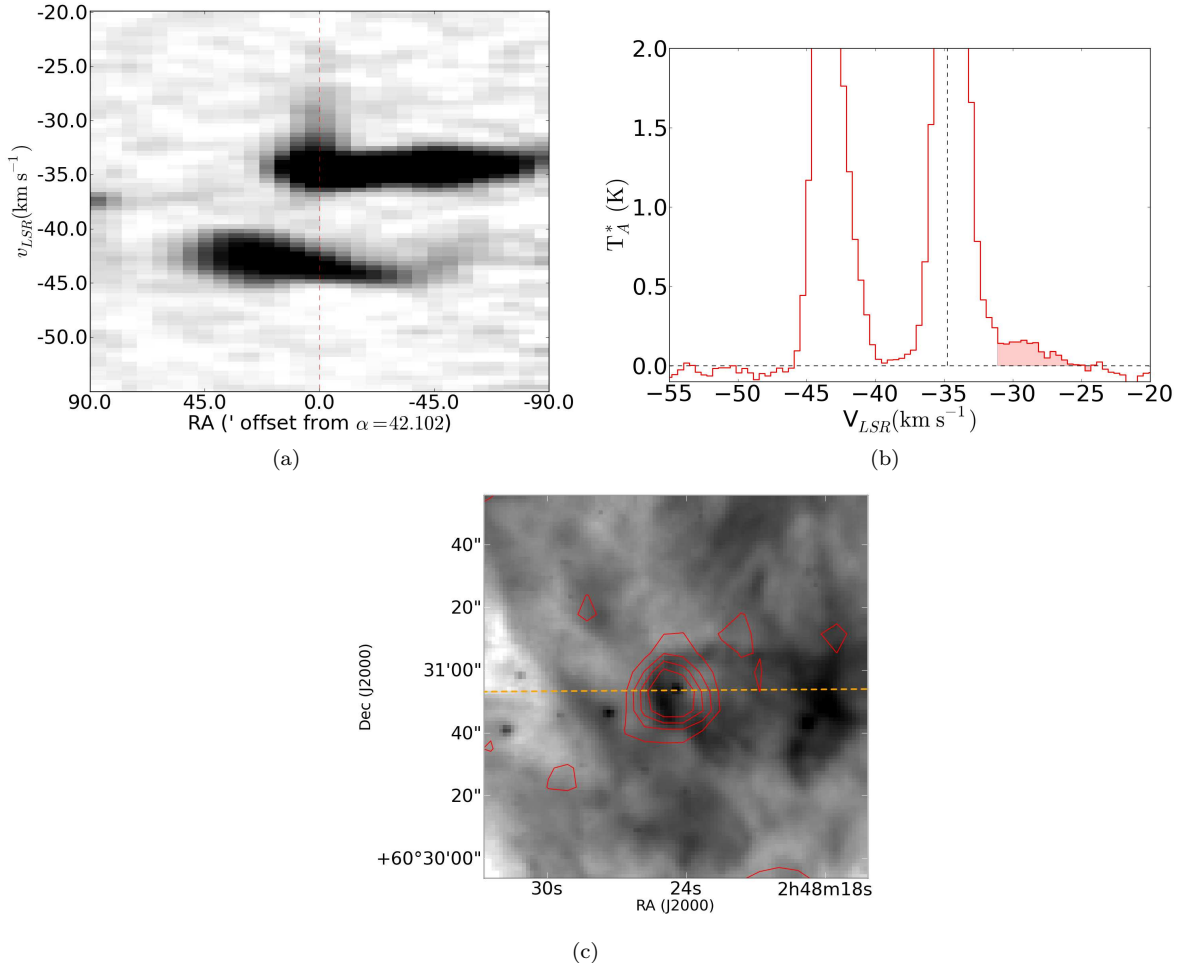


Figure 36. Position-velocity diagrams, spectra, and contour overlays of Outflow 13. The velocity distribution of gas in Outflow 13 is explored in more detail in Figure 23. No blueshifted counterflow could be detected, possibly because of confusion with the cloud at ~ -45 km s $^{-1}$ along the same line of sight.

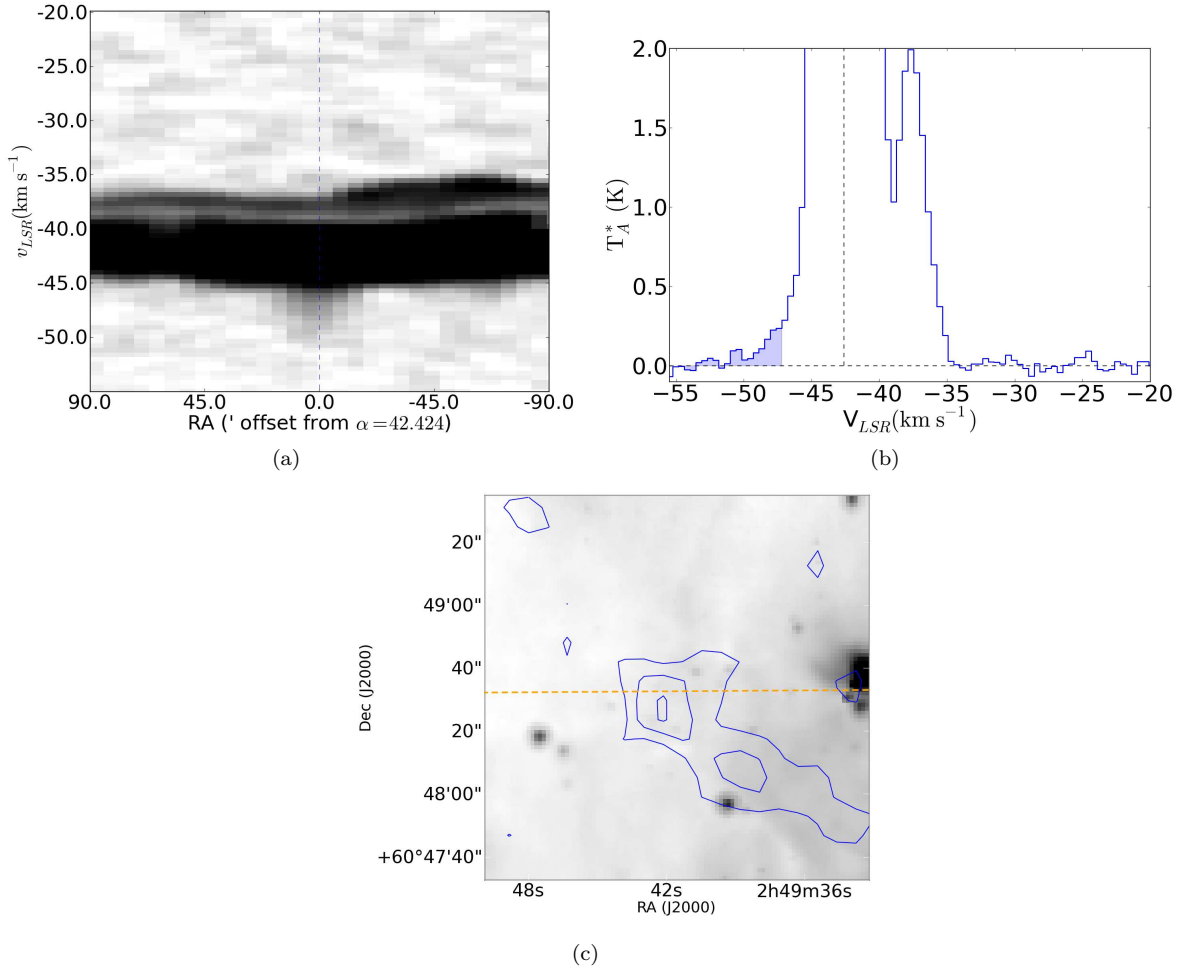


Figure 37. Position-velocity diagrams, spectra, and contour overlays of Outflow 14. No redshifted counterpart was detected, most likely because of confusion with the local cloud.

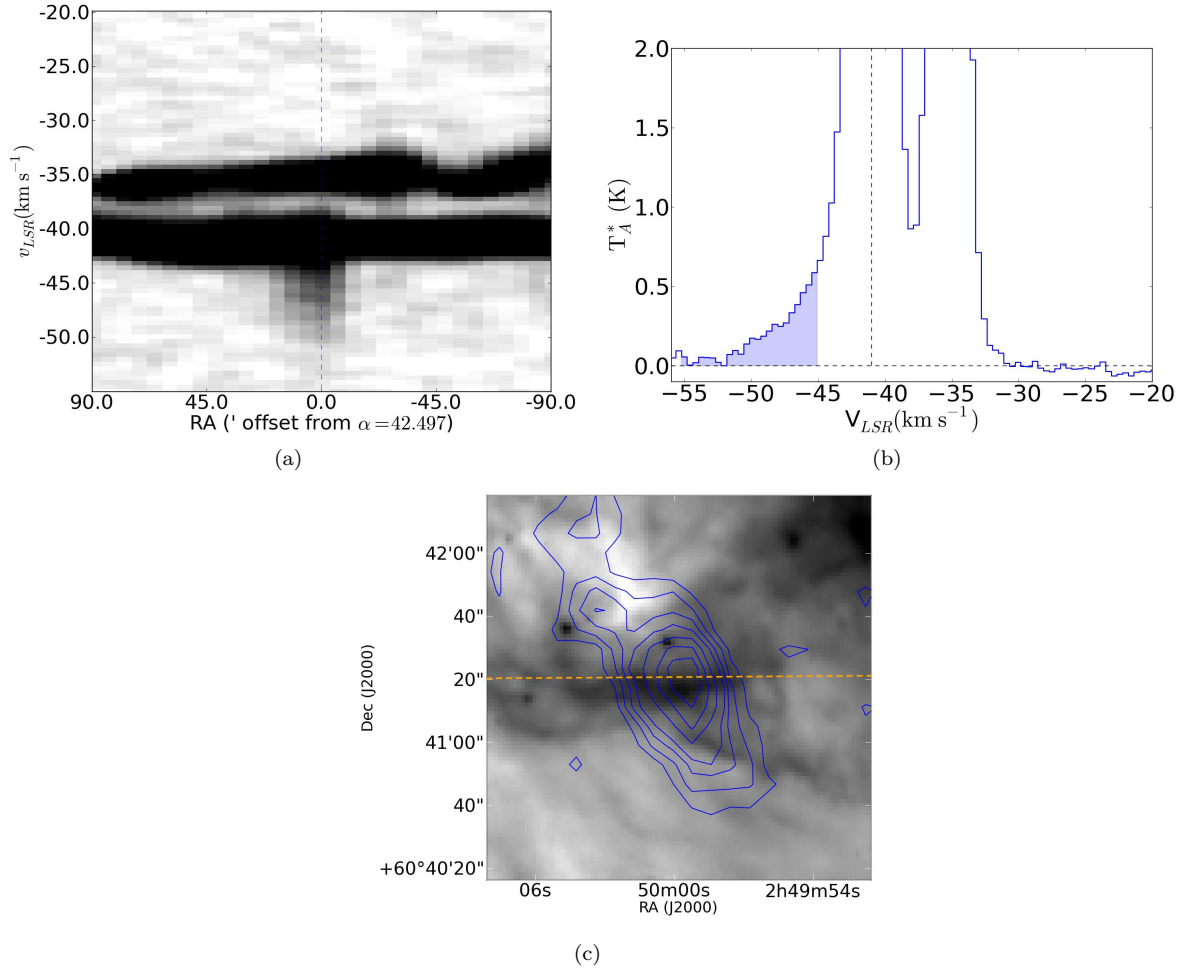


Figure 38. Position-velocity diagrams, spectra, and contour overlays of Outflow 15. No redshifted counterpart was detected, most likely because of confusion with the local cloud.

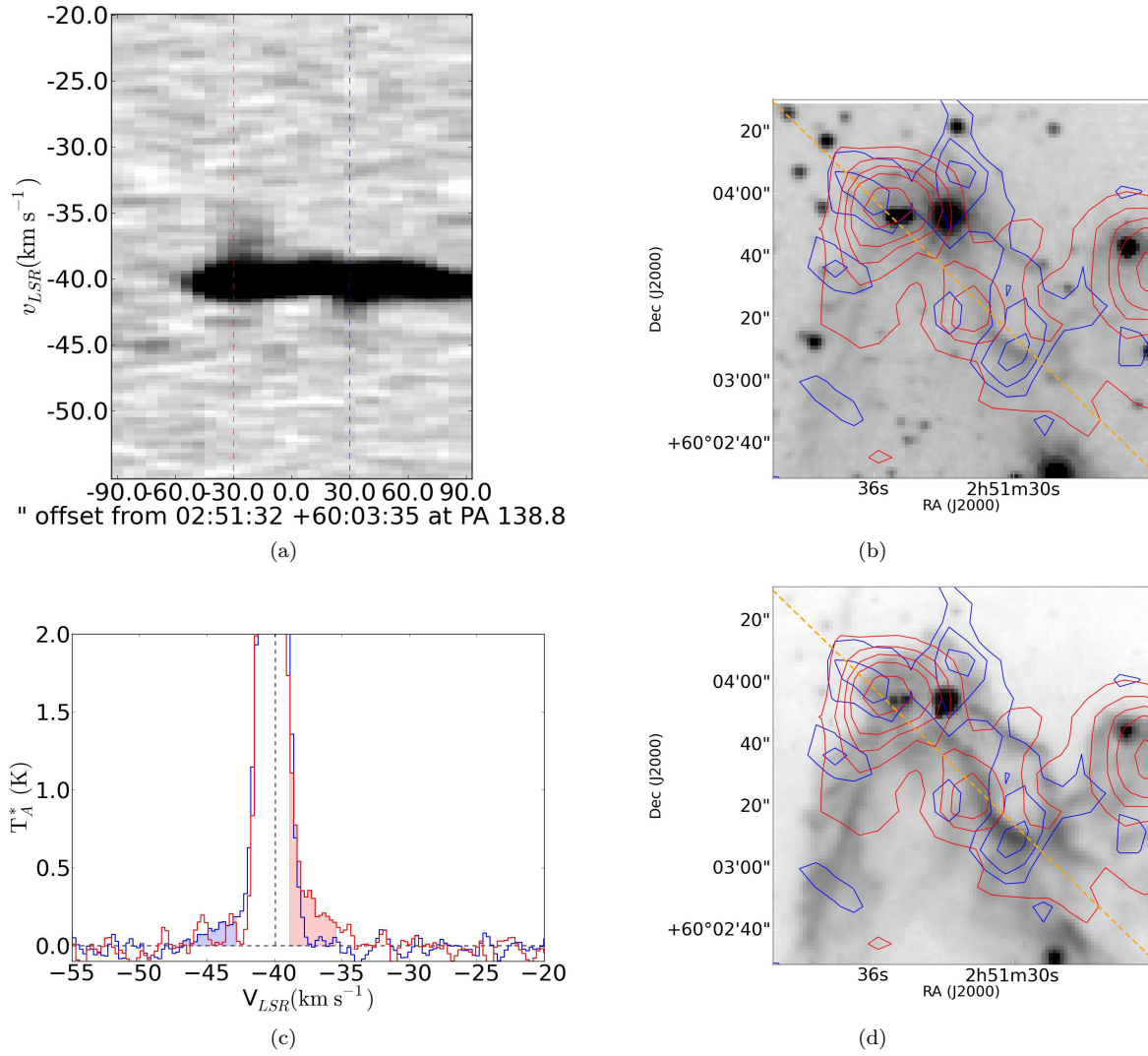


Figure 39. Position-velocity diagrams, spectra, and contour overlays of Outflow 16. Outflow 16 may actually be two distinct outflows; unfortunately it is nearly impossible to distinguish the two possibilities in position-velocity space. Contours are displayed at levels 0.3, 0.5, 0.75, 1.5, 2, 3, 4, 5, 6 K km s⁻¹ (blue) and 0.5, 1, 1.5, 2, 3, 4, 5, 6 K km s⁻¹ (red).

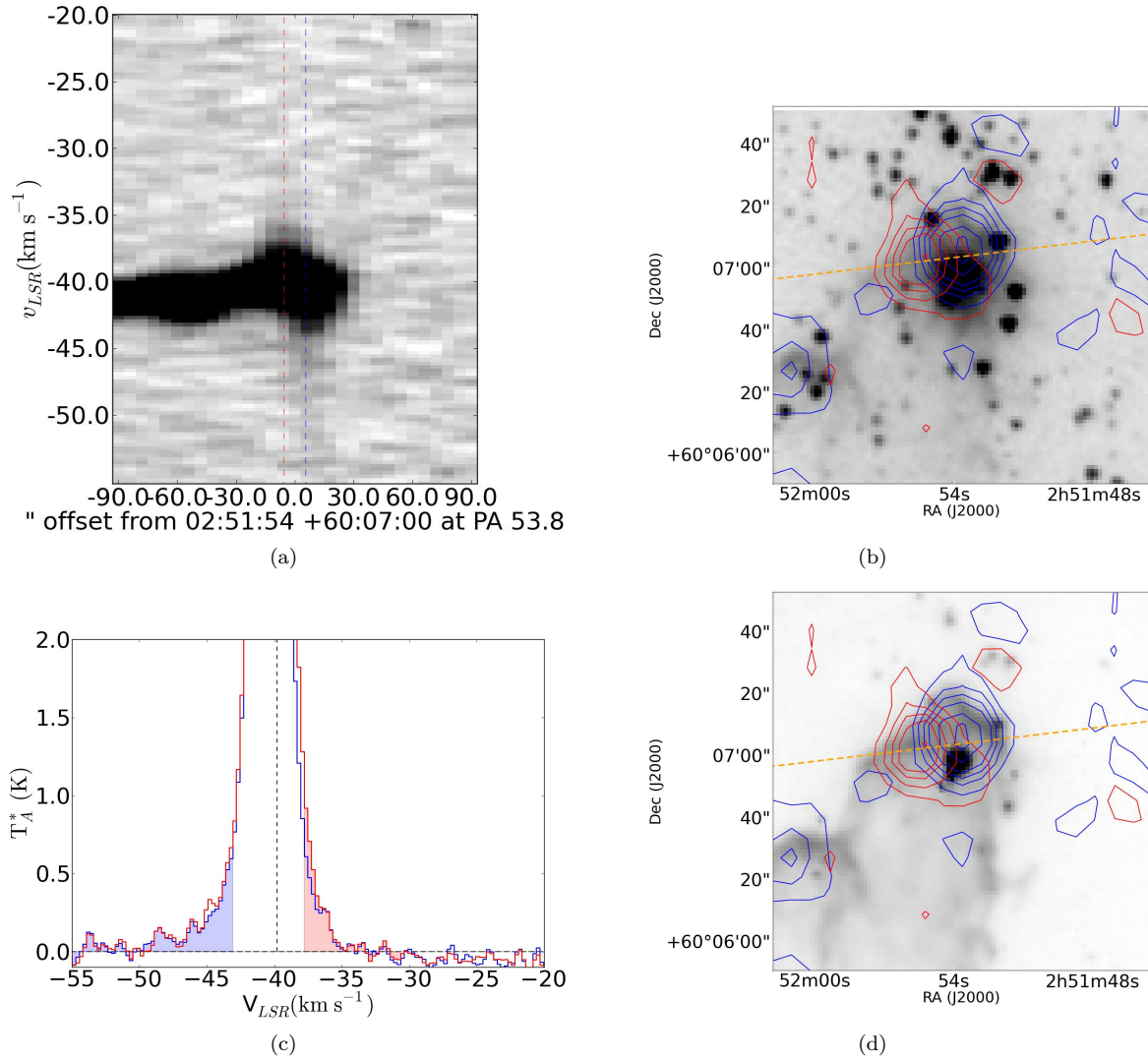


Figure 40. Position-velocity diagrams, spectra, and contour overlays of Outflow 17. This outflow pair is clear and isolated.

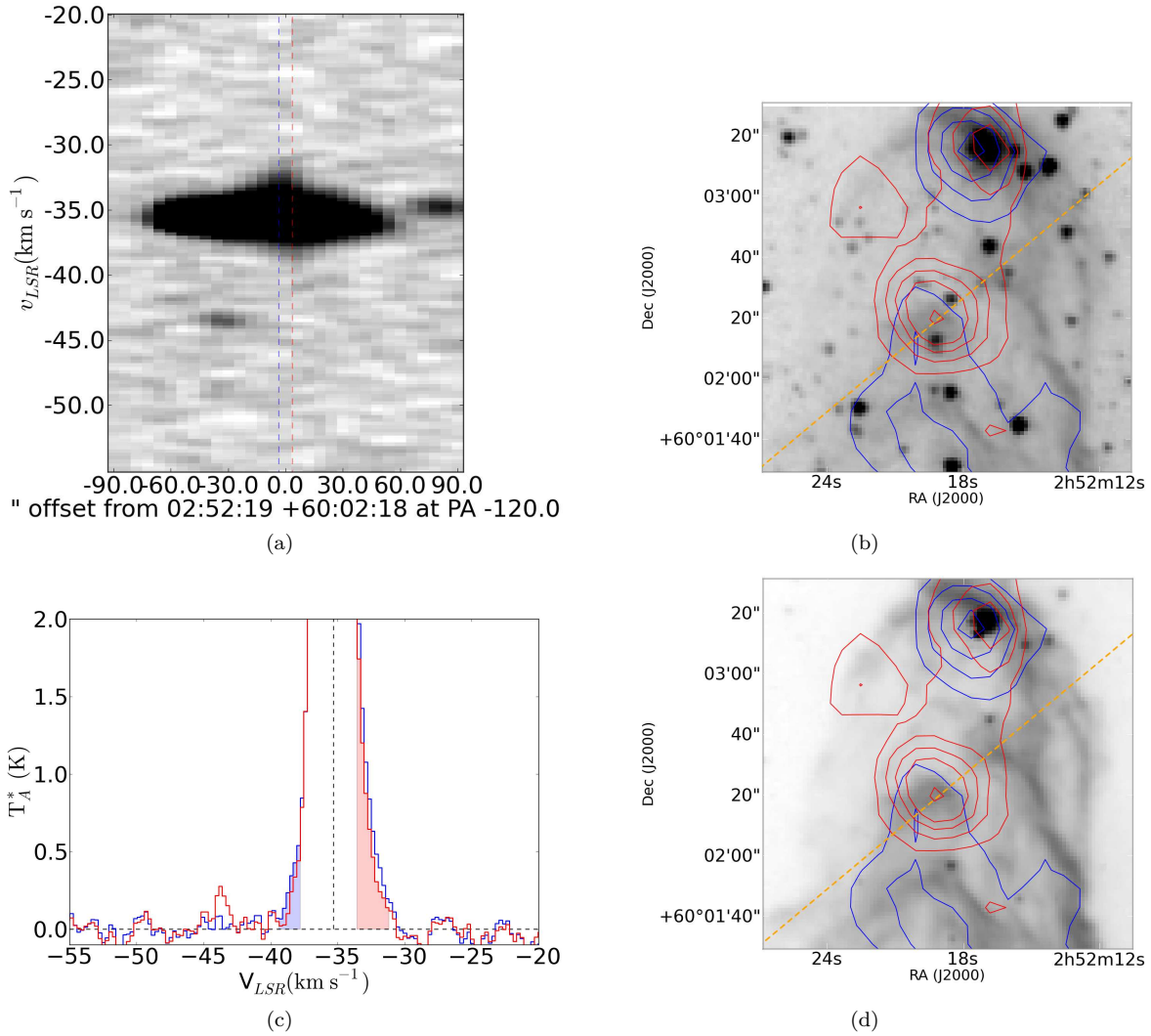


Figure 41. Position-velocity diagrams, spectra, and contour overlays of Outflow 18. Similar to Outflow 16, there are many confusing lobes nearby, but since there is a clear counterpart to Outflow 19 (the lobes in the north half of panels (b) and (d)) and a weak but nonetheless apparent flow in position- velocity space, we regard this as a reliable pair detection. The velocity structure of these flows is explored in more detail in Figure 20.

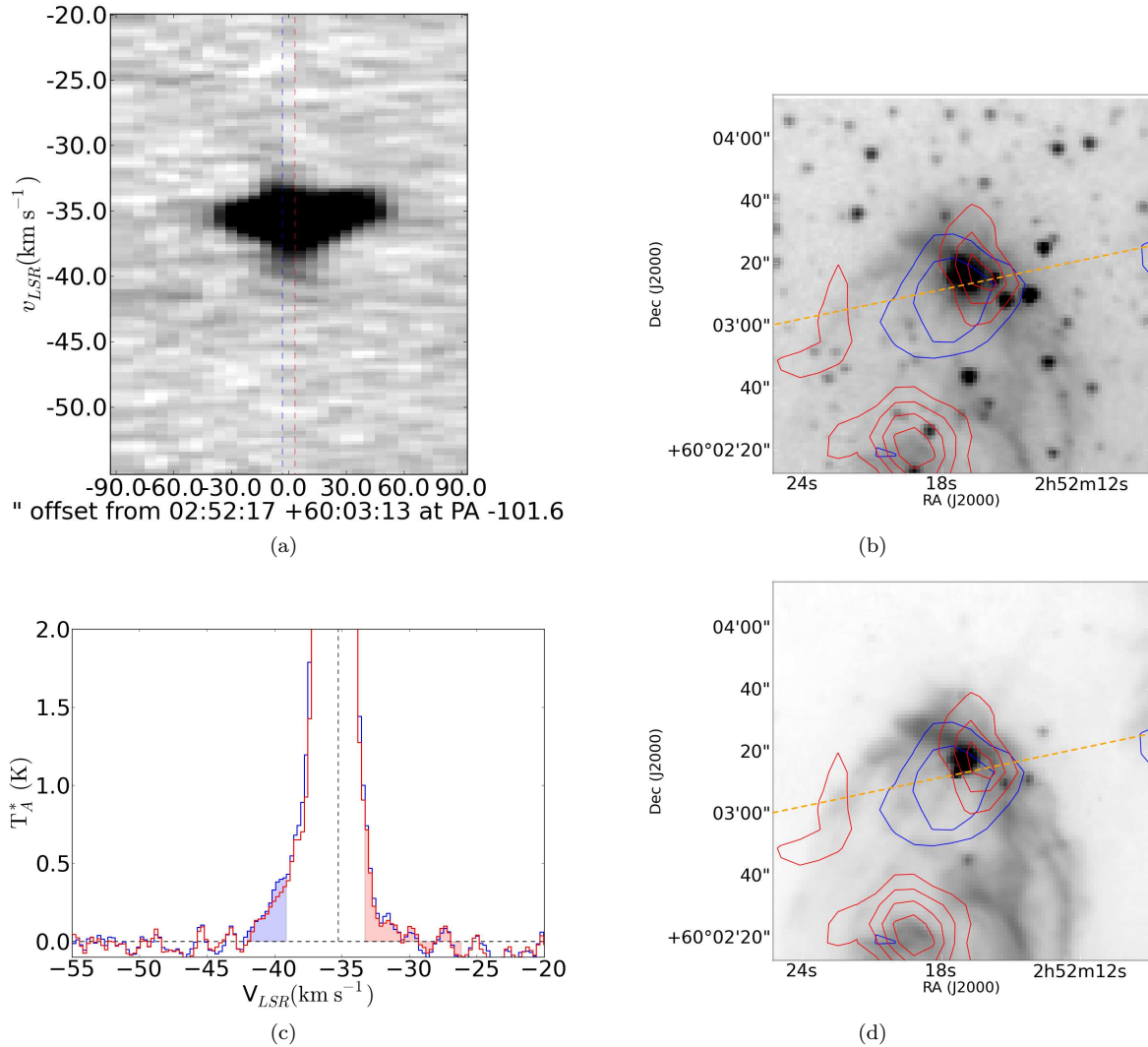


Figure 42. Position-velocity diagrams, spectra, and contour overlays of Outflow 19. The velocity structure of these flows is explored in more detail in Figure 20.

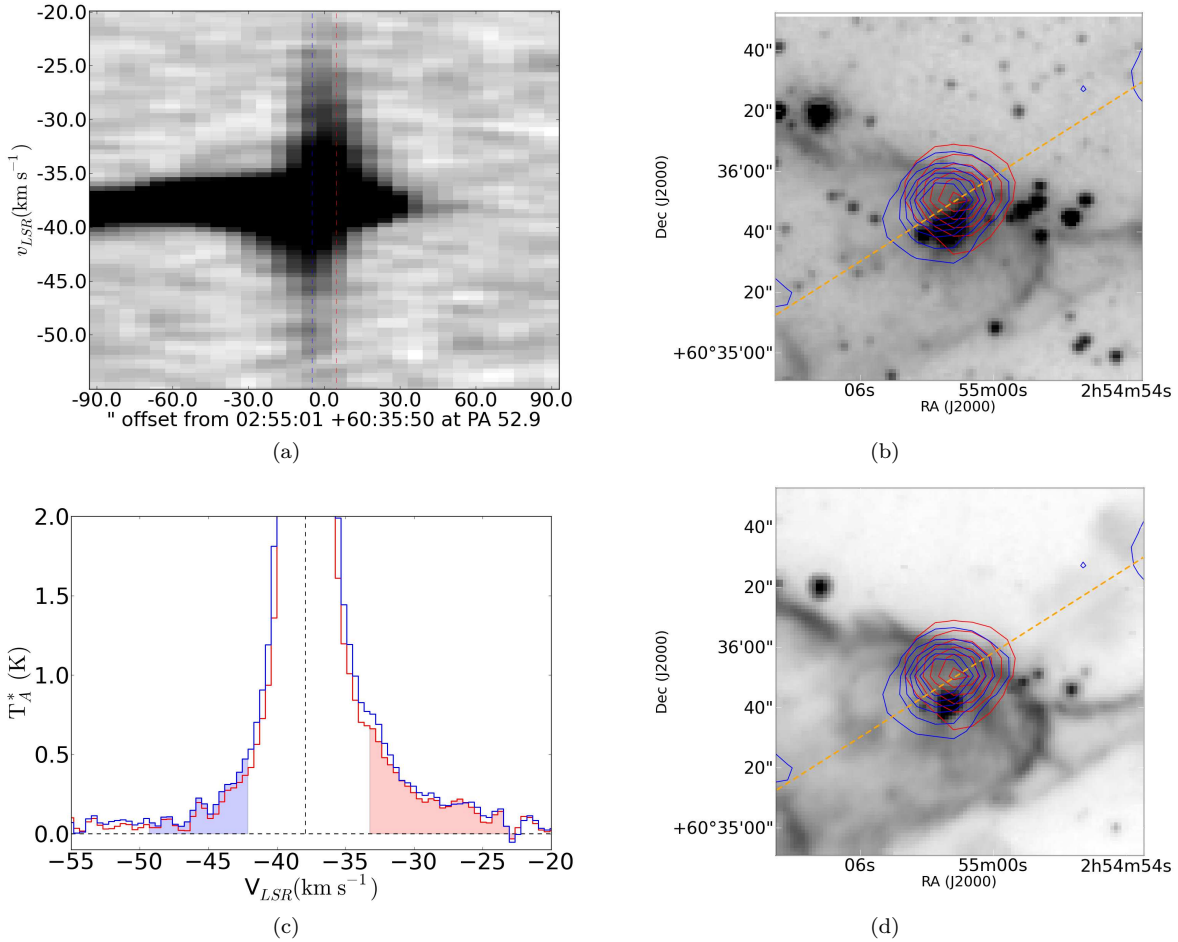


Figure 43. Position-velocity diagrams, spectra, and contour overlays of Outflow 20. The outflow is clearly detected in both red and blue. Contours are displayed at levels 1,2,3,4,5 ,6 K km s⁻¹ (blue) and 2,4,6,8,10,12 K km s⁻¹ (red).

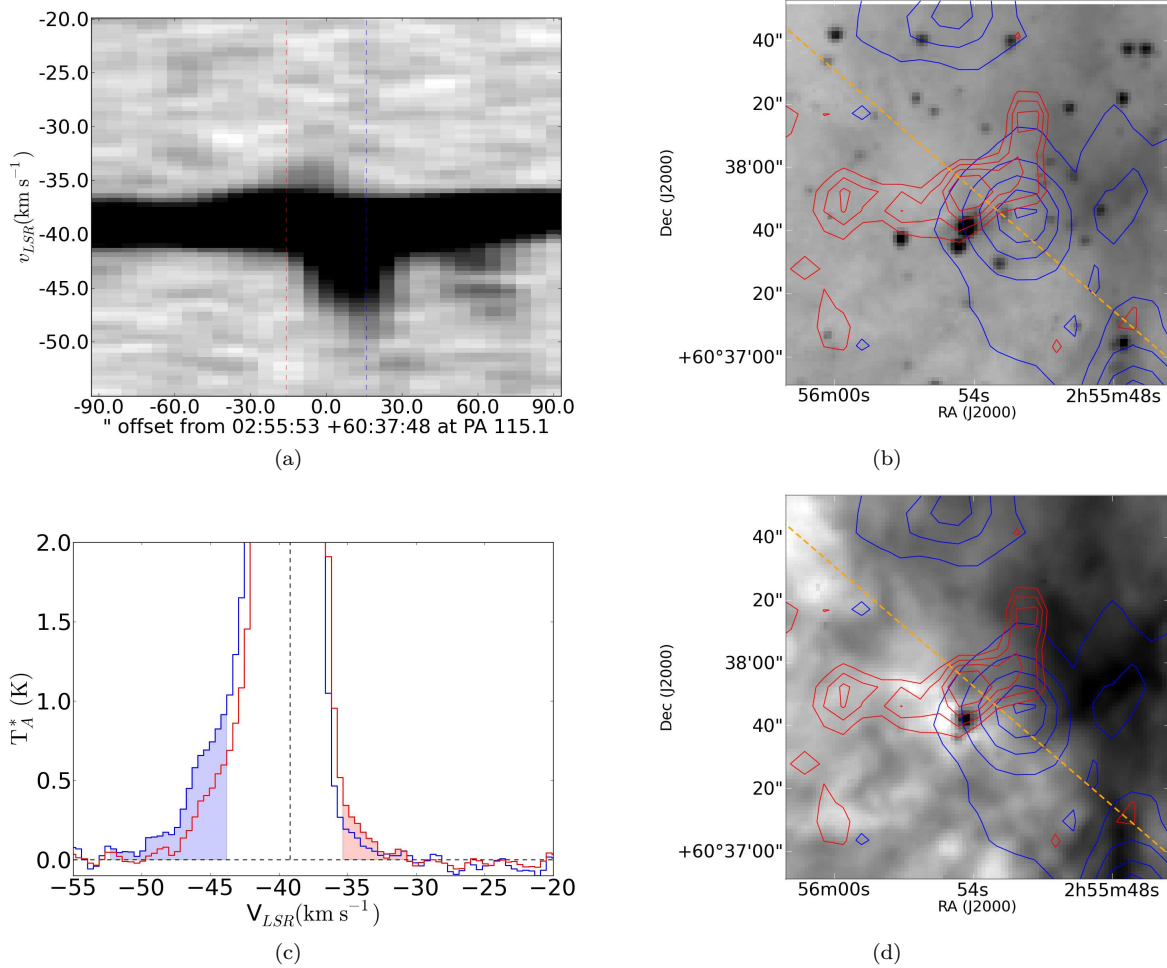


Figure 44. Position-velocity diagrams, spectra, and contour overlays of Outflow 21. Contours are displayed at levels 1,3,5,7,9 K km s $^{-1}$ (blue) and 0.75,1,1.25,1.5,2 K km s $^{-1}$ (red).

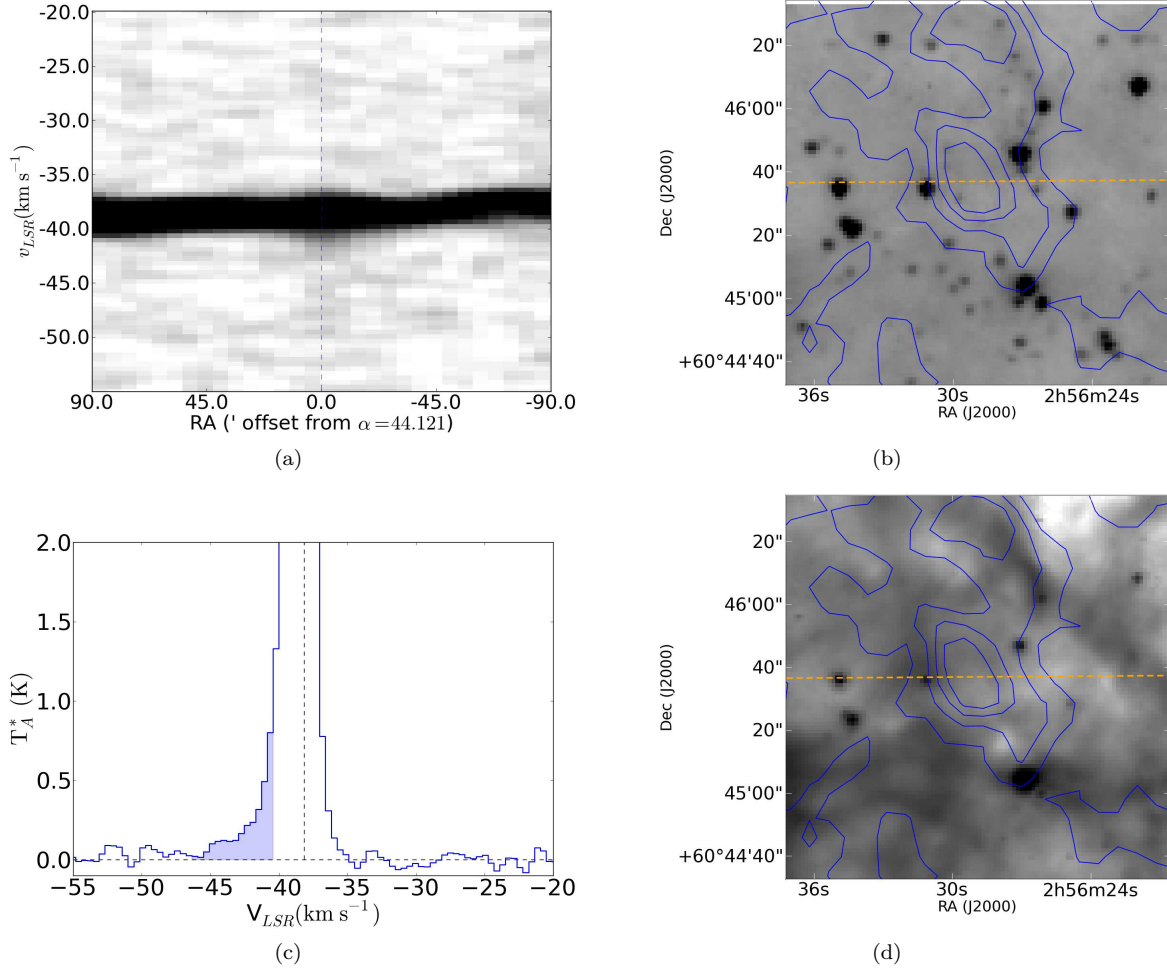


Figure 45. Position-velocity diagrams, spectra, and contour overlays of Outflow 22. A red outflow signature may be present, but it is not significant at > 1 channel from the cloud and therefore could not be clearly identified.

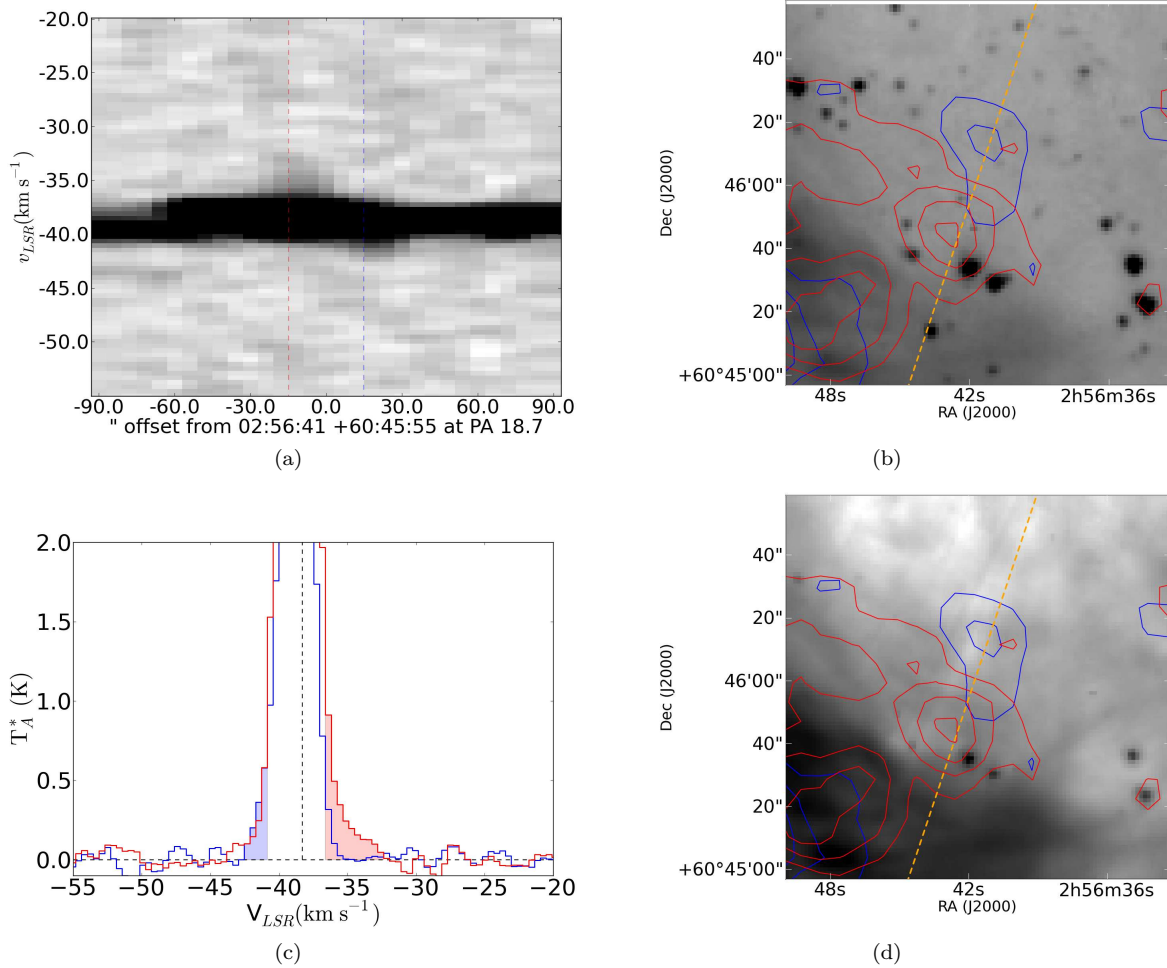


Figure 46. Position-velocity diagrams, spectra, and contour overlays of Outflow 23.

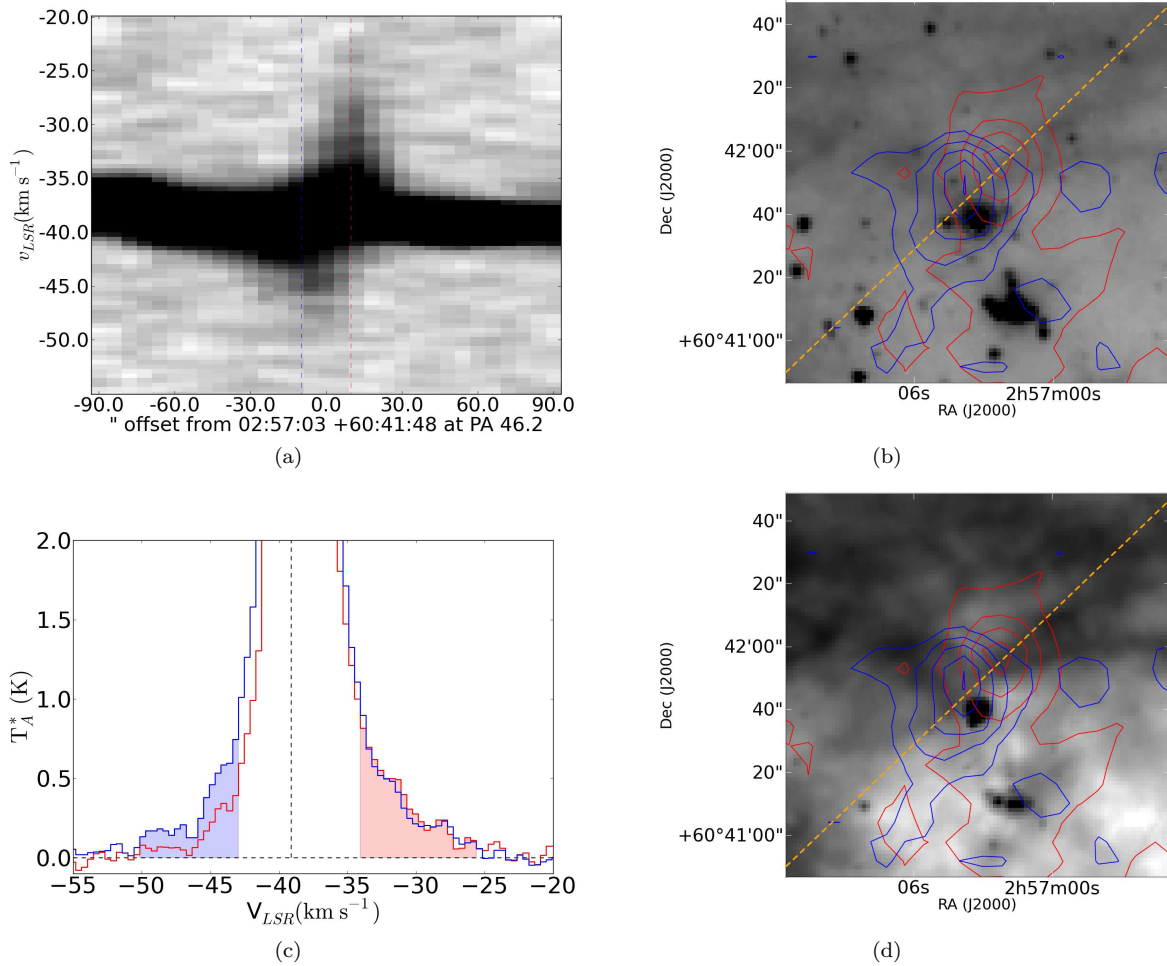


Figure 47. Position-velocity diagrams, spectra, and contour overlays of Outflow 24. Contours are displayed at levels 1,3,5,7 K km s $^{-1}$ (blue) and 1,2,3,4,5 K km s $^{-1}$ (red).

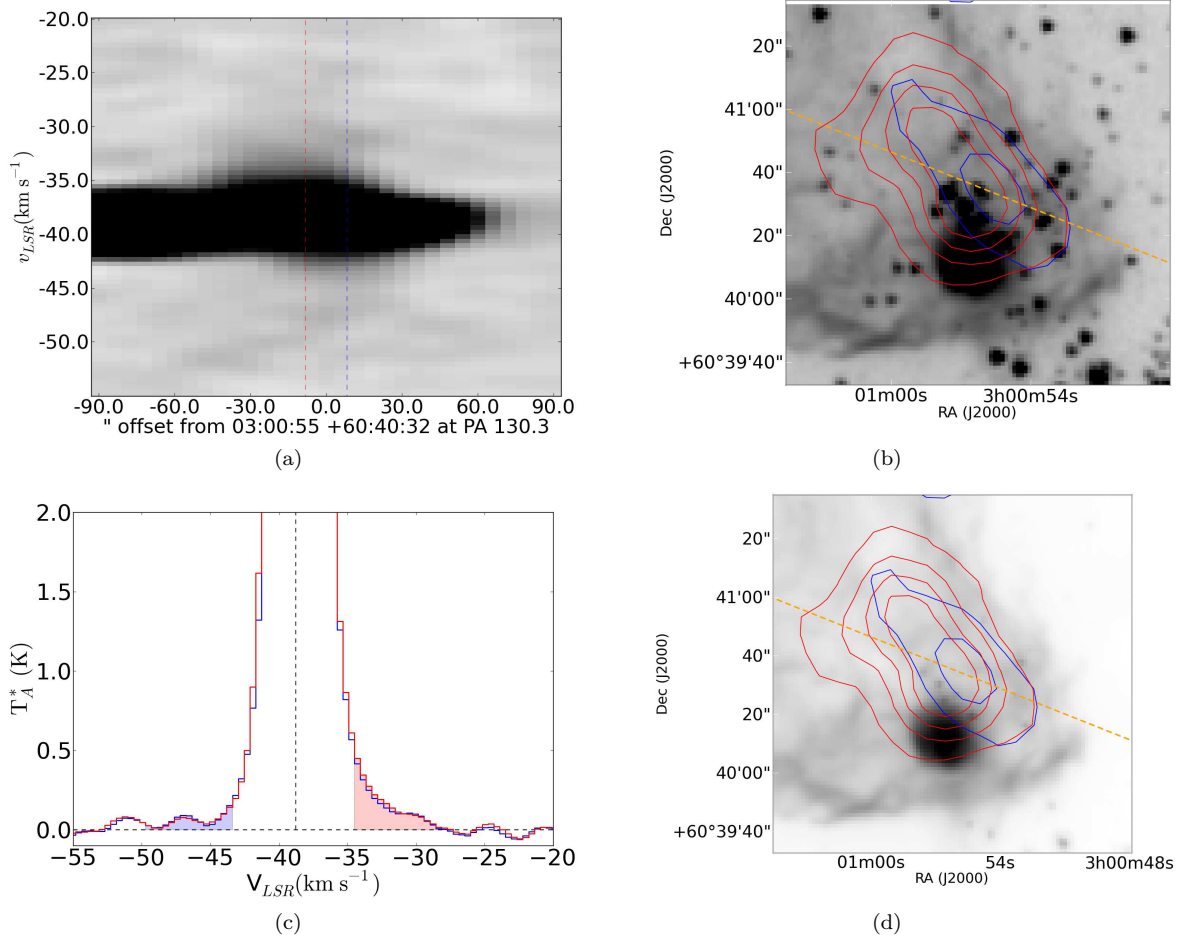


Figure 48. Position-velocity diagrams, spectra, and contour overlays of Outflow 25. The kinematics of the cometary cloud that hosts this outflow are explored in Figure 17.

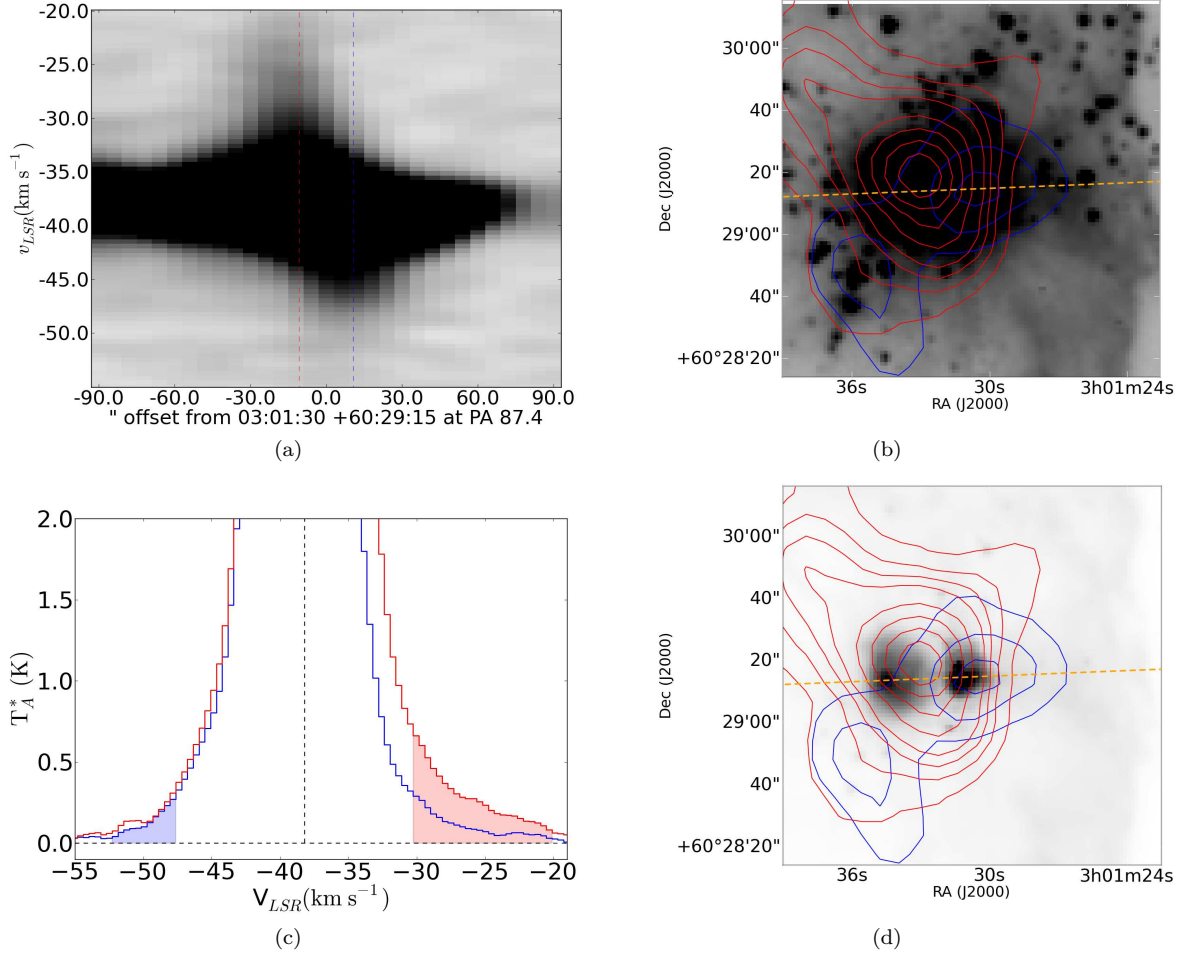


Figure 49. Position-velocity diagrams, spectra, and contour overlays of Outflow 26. This is the main outflow in AFGL 4029, and a firm association is made between the two lobes because of their proximity and strength compared to the other flows (27-32) nearby.

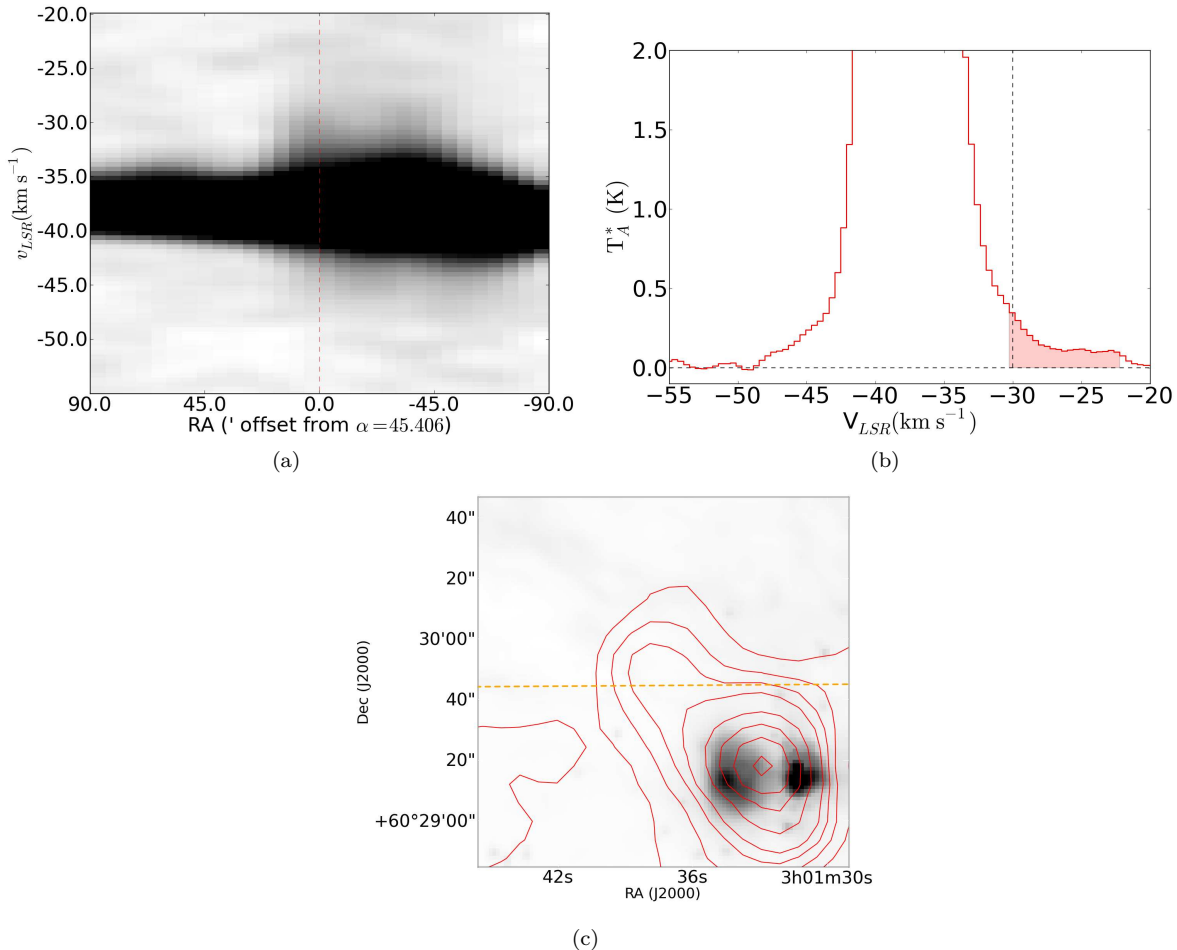


Figure 50. Position-velocity diagrams, spectra, and contour overlays of Outflow 27. Because of confusion in the AFGL 4029 region, no counterflow could be identified.

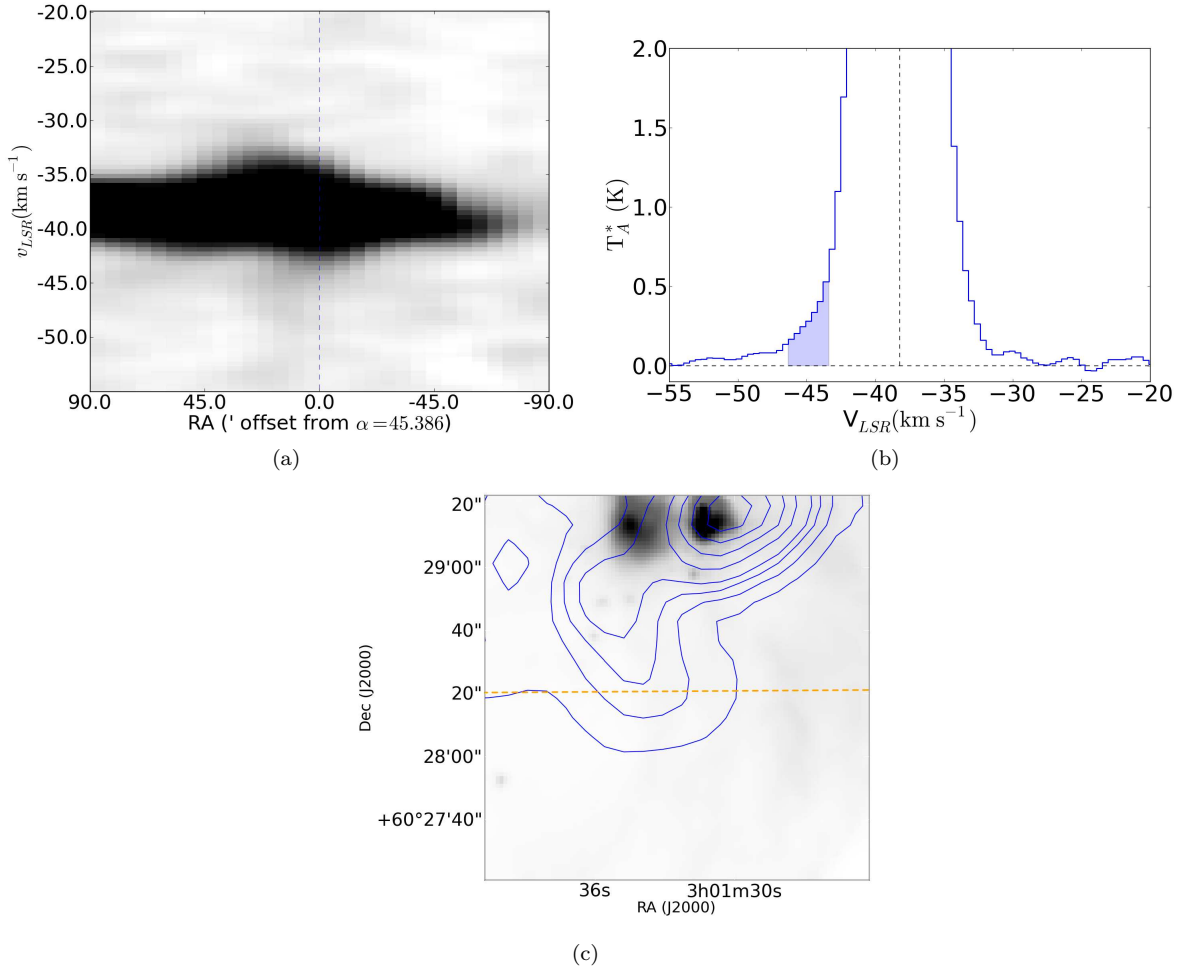


Figure 51. Position-velocity diagrams, spectra, and contour overlays of Outflow 28. Because of confusion in the AFGL 4029 region, no counterflow could be identified.

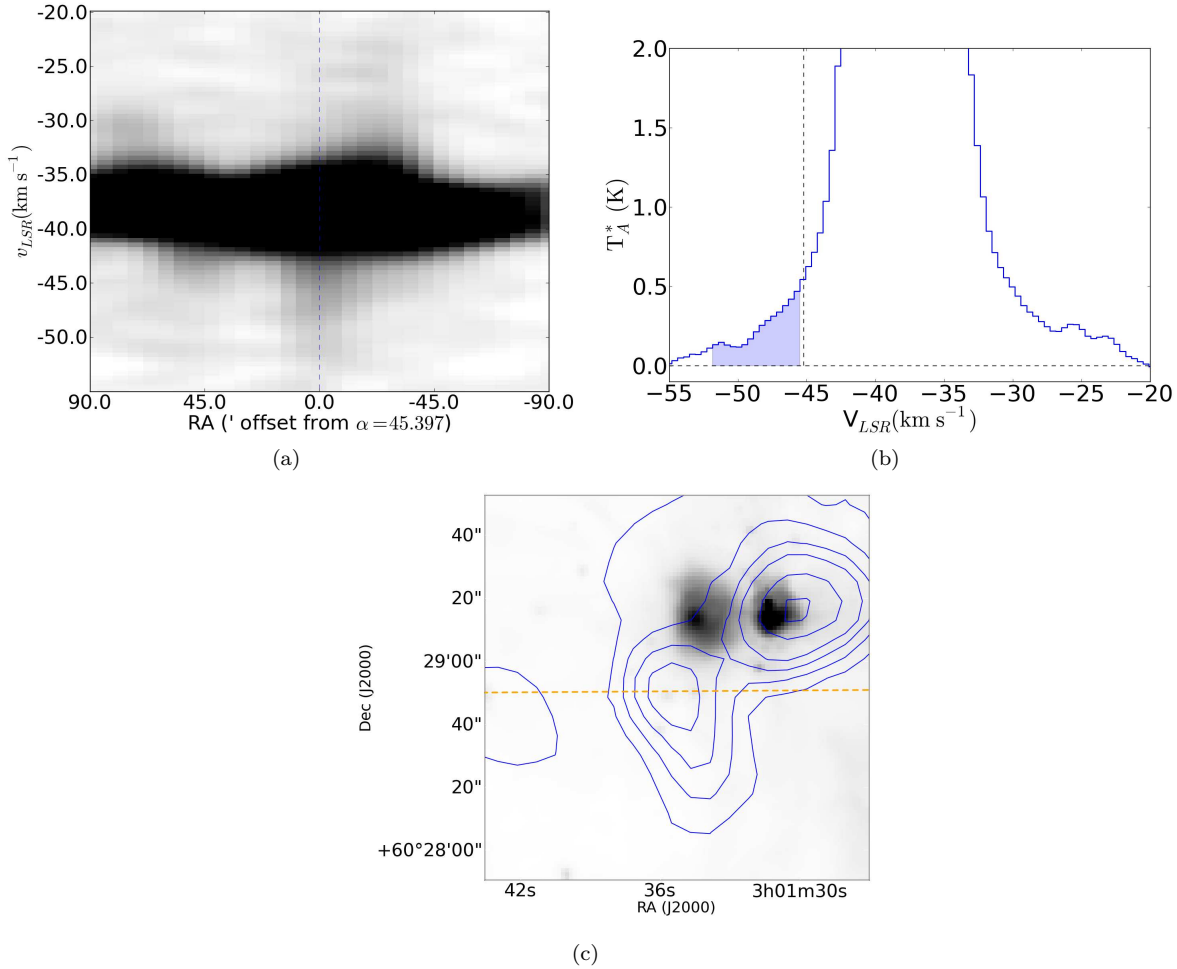


Figure 52. Position-velocity diagrams, spectra, and contour overlays of Outflow 29. Because of confusion in the AFGL 4029 region, no counterflow could be identified.

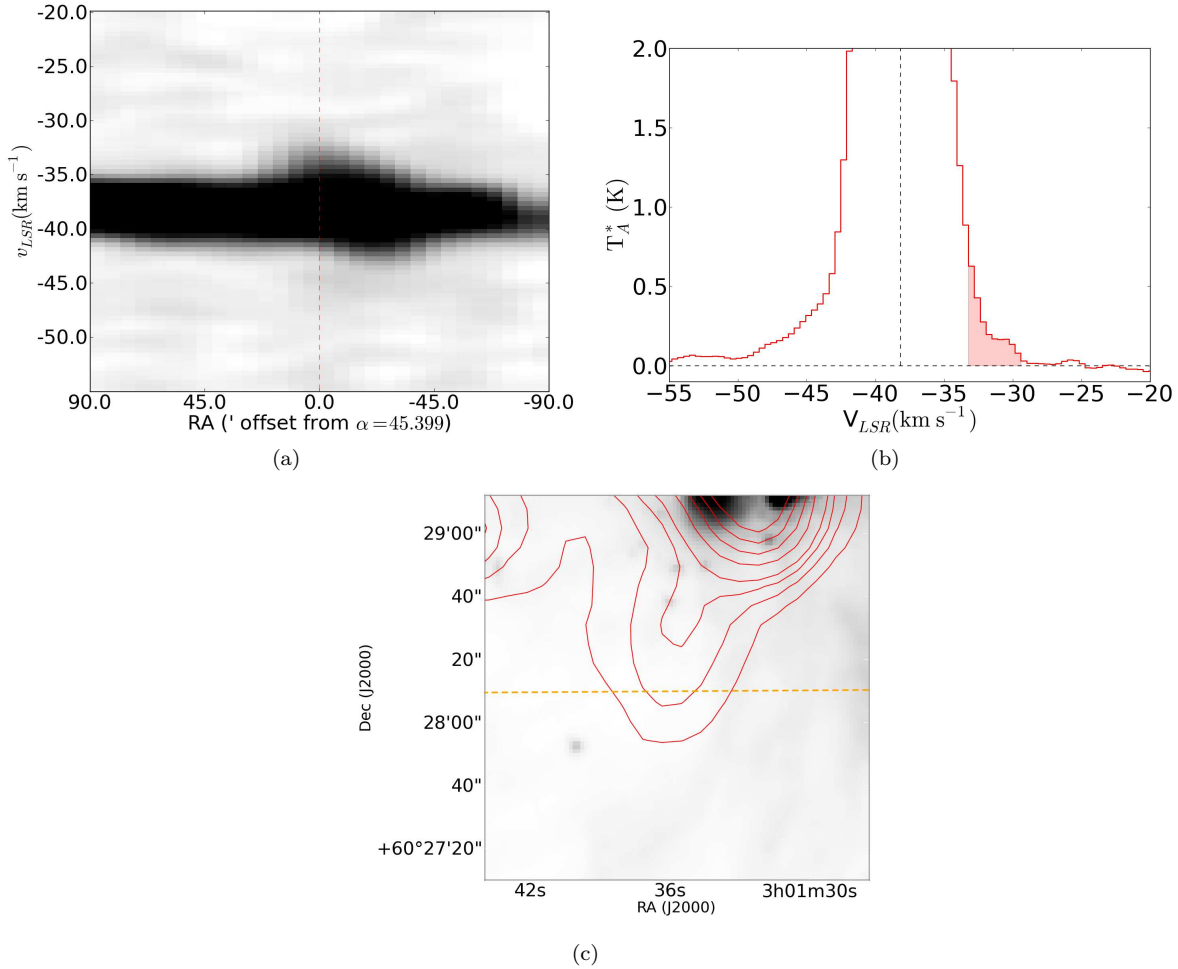


Figure 53. Position-velocity diagrams, spectra, and contour overlays of Outflow 30. Because of confusion in the AFGL 4029 region, no counterflow could be identified.

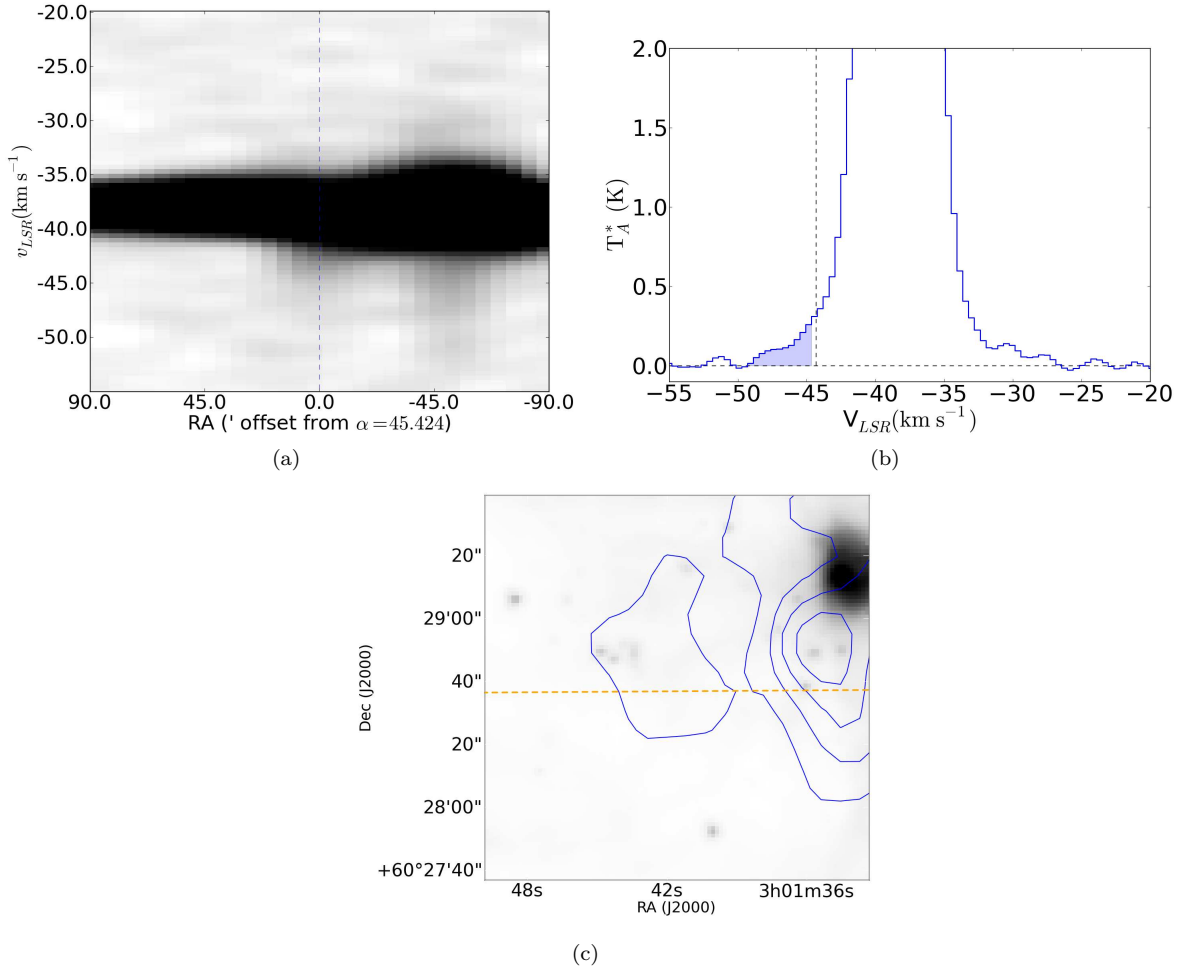


Figure 54. Position-velocity diagrams, spectra, and contour overlays of Outflow 31. Because of confusion in the AFGL 4029 region, no counterflow could be identified.

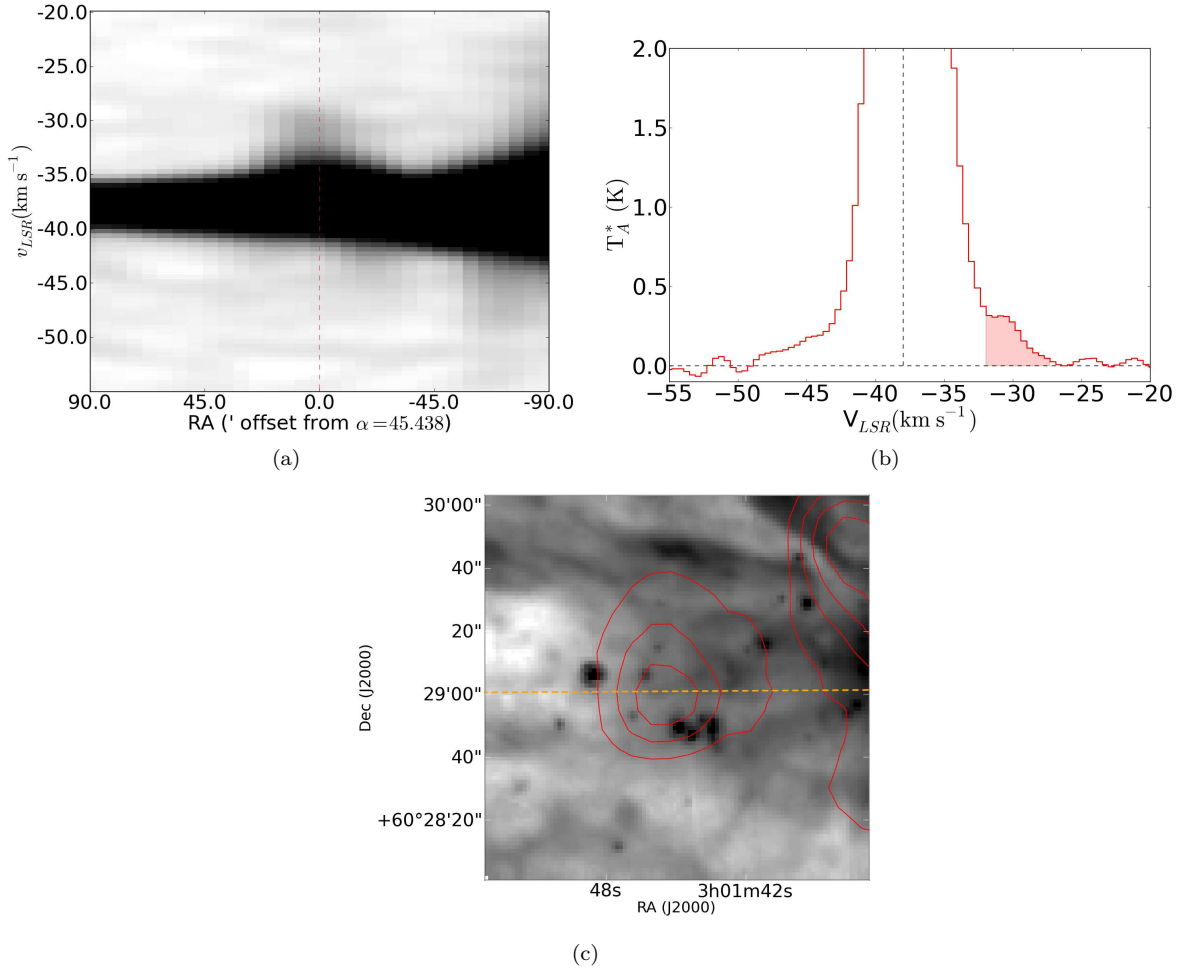


Figure 55. Position-velocity diagrams, spectra, and contour overlays of Outflow 32. Because of confusion in the AFGL 4029 region, no counterflow could be identified.

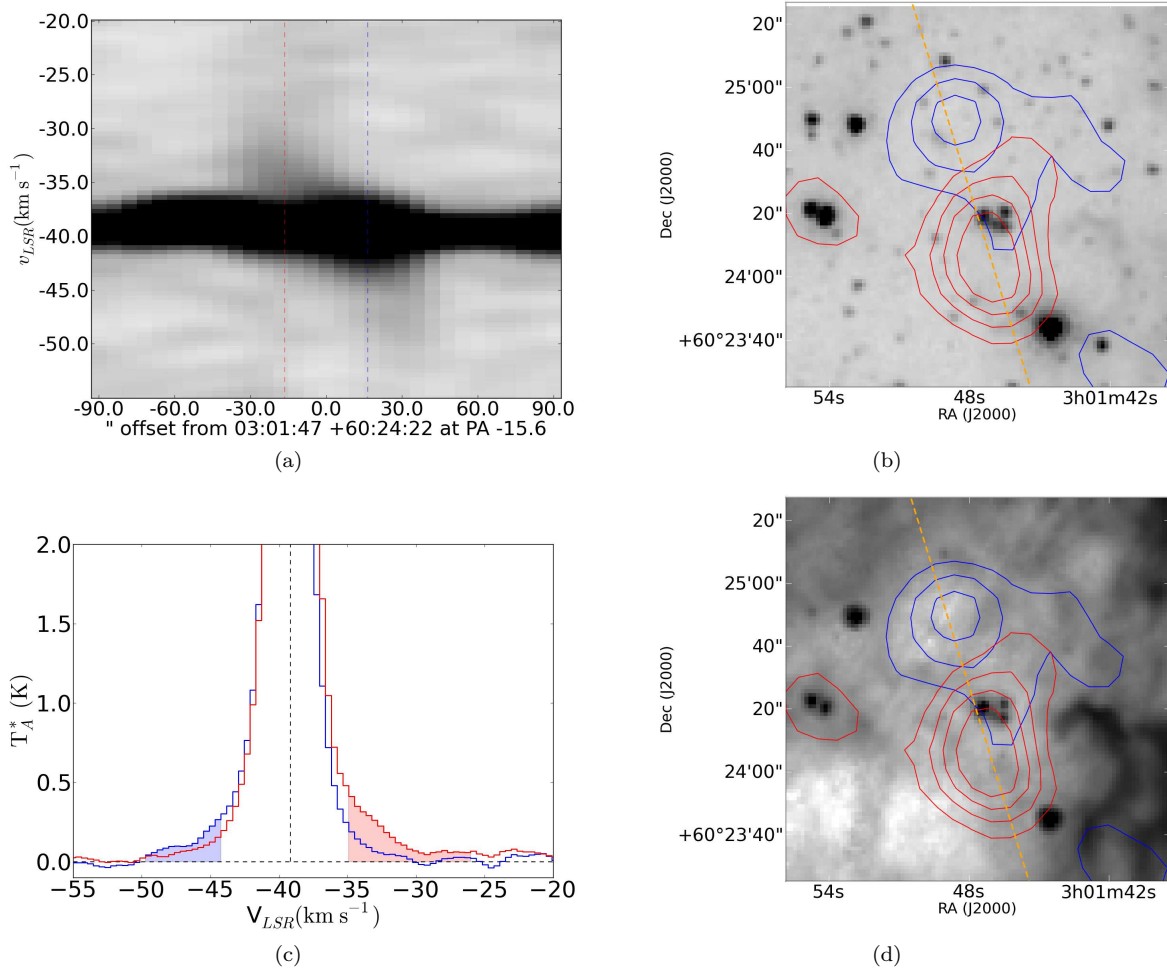


Figure 56. Position-velocity diagrams, spectra, and contour overlays of Outflow 33. The bipolar outflow is clear in both the position-velocity diagram as a gradient and the contour plots.

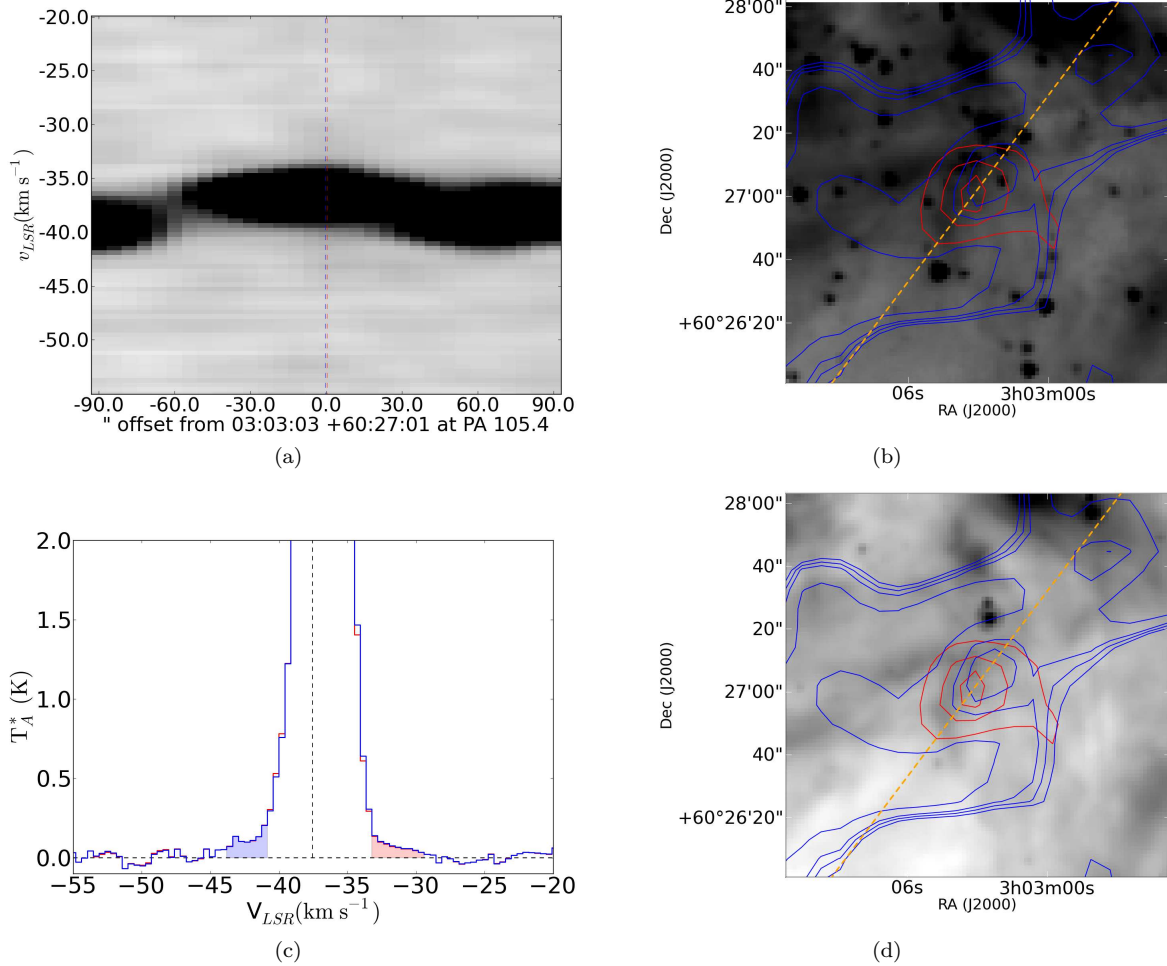


Figure 57. Position-velocity diagrams, spectra, and contour overlays of Outflow 34. The outflow is very faint, but apparently bipolar. Contour levels are 0.25, 0.4, 0.5 K km s $^{-1}$ (red) and 0.25, 0.4, 0.45, 0.5 K km s $^{-1}$ (blue)

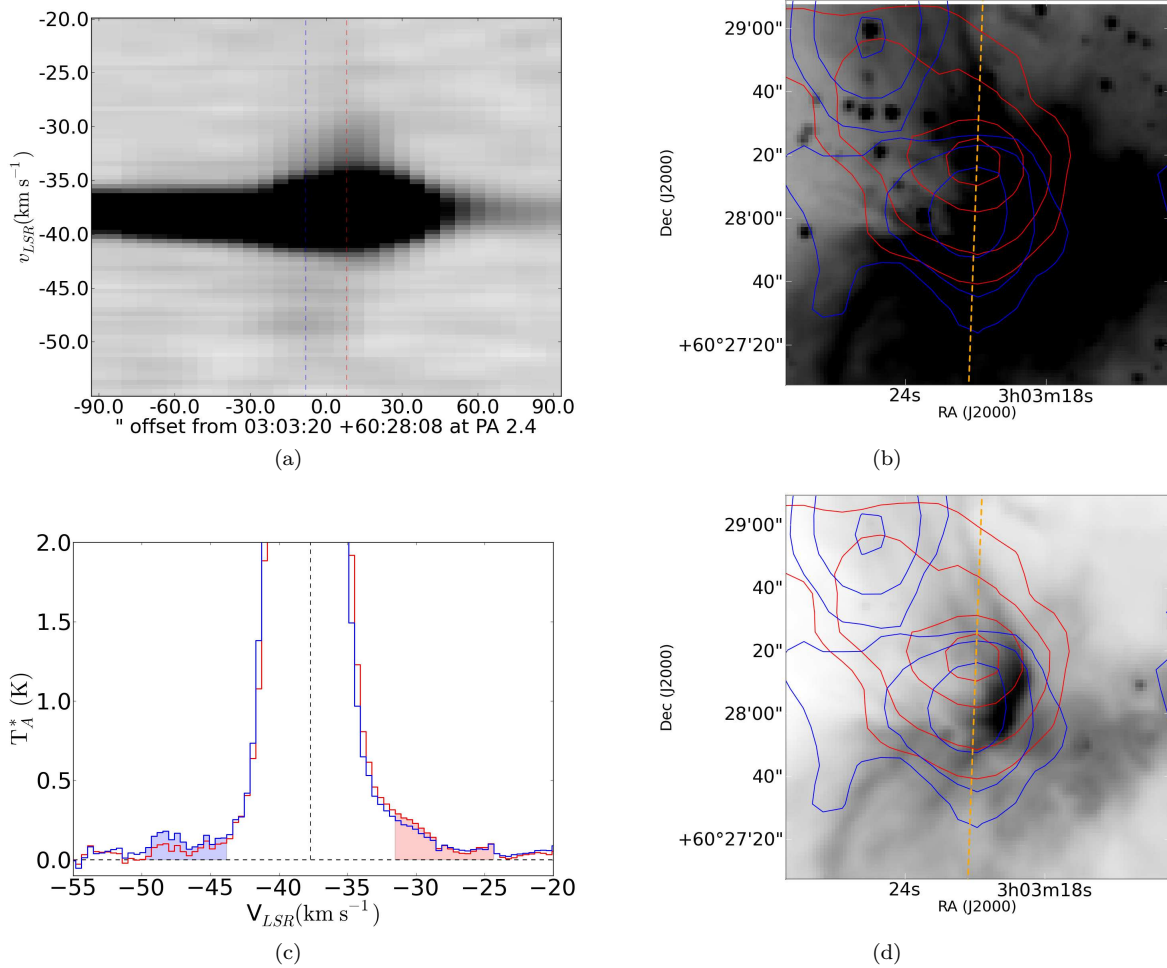


Figure 58. Position-velocity diagrams, spectra, and contour overlays of Outflow 35. Contours are displayed at levels $0.25, 0.5, 1, 1.5, 2, 3, 4, 5, 6 \text{ K km s}^{-1}$ (blue) and $0.25, 0.5, 1, 1.5, 2, 3, 4, 5, 6 \text{ K km s}^{-1}$ (red).

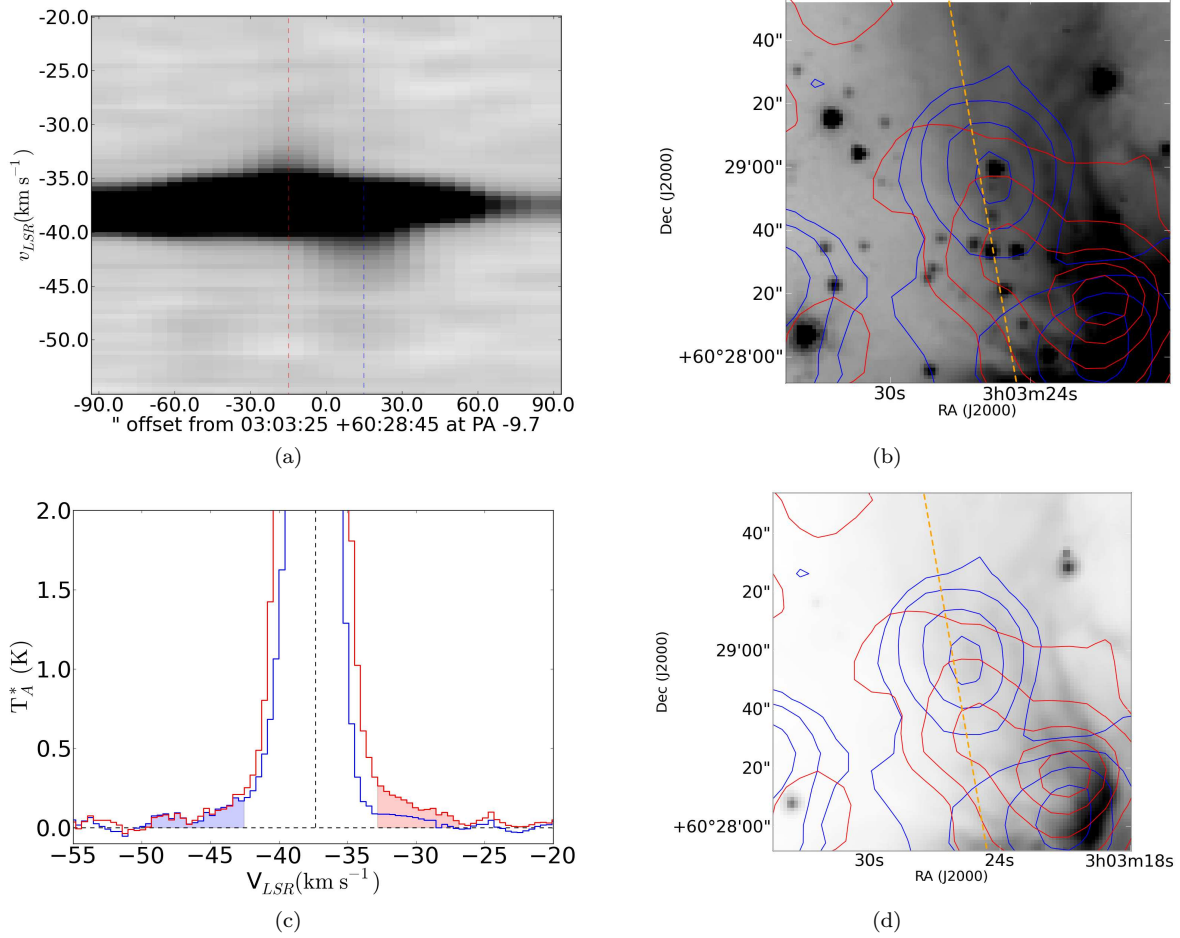


Figure 59. Position-velocity diagrams, spectra, and contour overlays of Outflow 36. Contours are displayed at levels $0.25, 0.5, 1, 1.5, 2, 3, 4, 5, 6 \text{ K km s}^{-1}$ (blue) and $0.25, 0.5, 1, 1.5, 2, 3, 4, 5, 6 \text{ K km s}^{-1}$ (red).

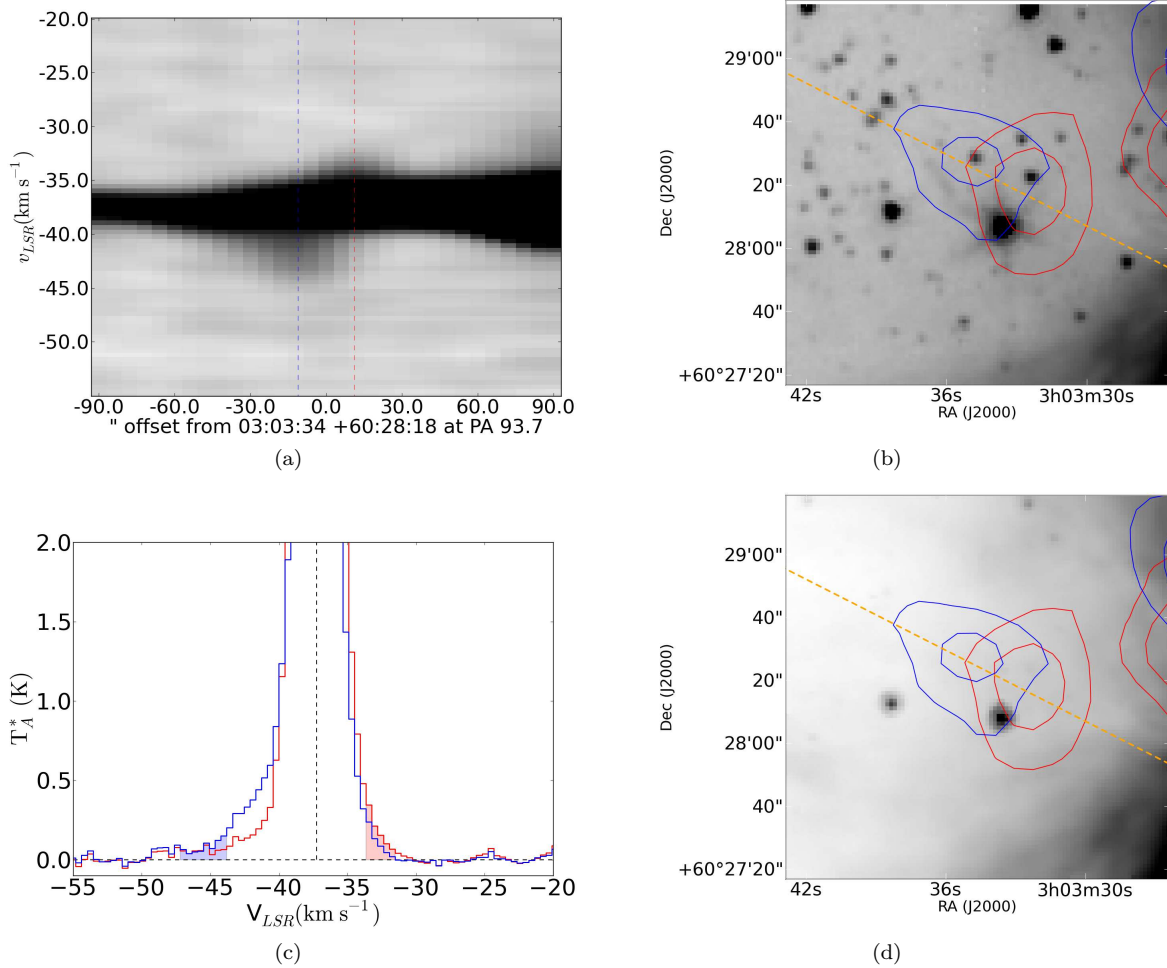


Figure 60. Position-velocity diagrams, spectra, and contour overlays of Outflow 37. There is a faint streak in the $4.5 \mu\text{m}$ image at $03:03:36.3 +60:28:22$ that may be an H_2 jet. Contours are displayed at levels $0.25, 0.5, 1.0 \text{ K km s}^{-1}$ (blue) and $0.25, 0.5, 1.0 \text{ K km s}^{-1}$ (red).

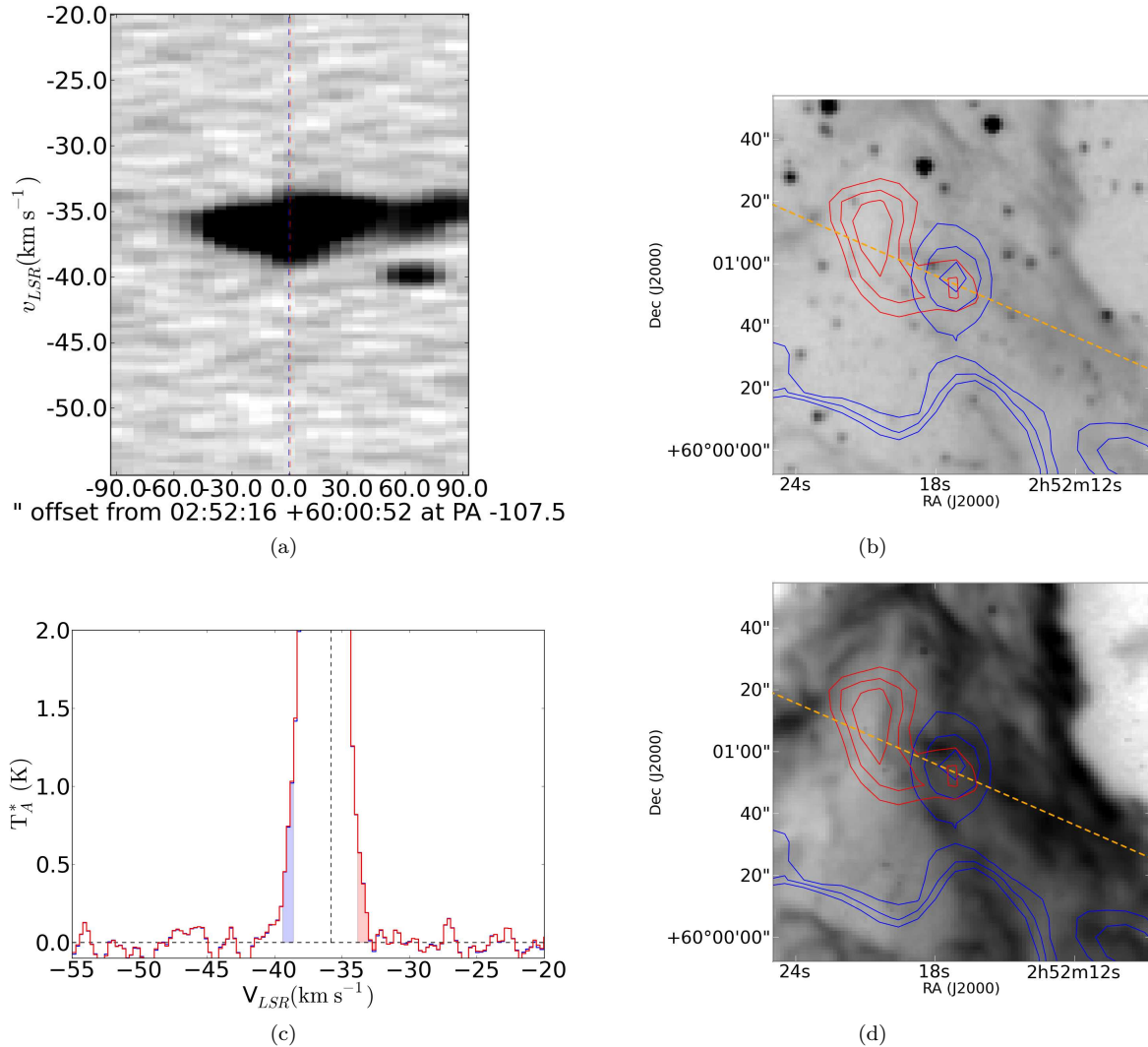


Figure 61. Position-velocity diagrams, spectra, and contour overlays of Outflow 38. The red contours to the left of center show a clump of gas at the same velocity as the redshifted flow, but this gas does not appear to be part of an outflow system as it has an approximately gaussian line profile. Contours are displayed at levels $0.5, 0.75, 1 \text{ K km s}^{-1}$ (blue) and $0.5, 0.75, 1 \text{ K km s}^{-1}$ (red).

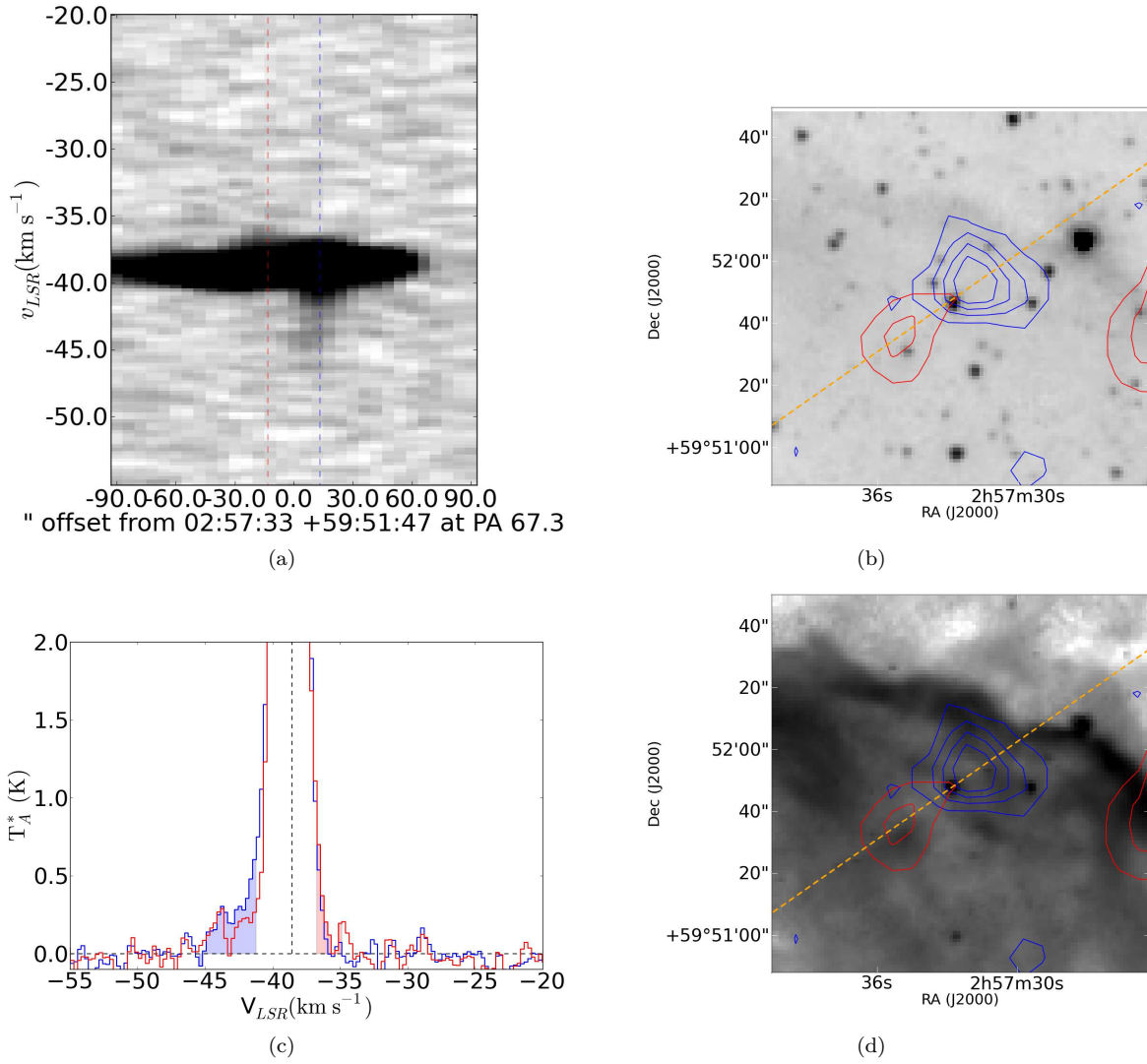


Figure 62. Position-velocity diagrams, spectra, and contour overlays of Outflow 39.

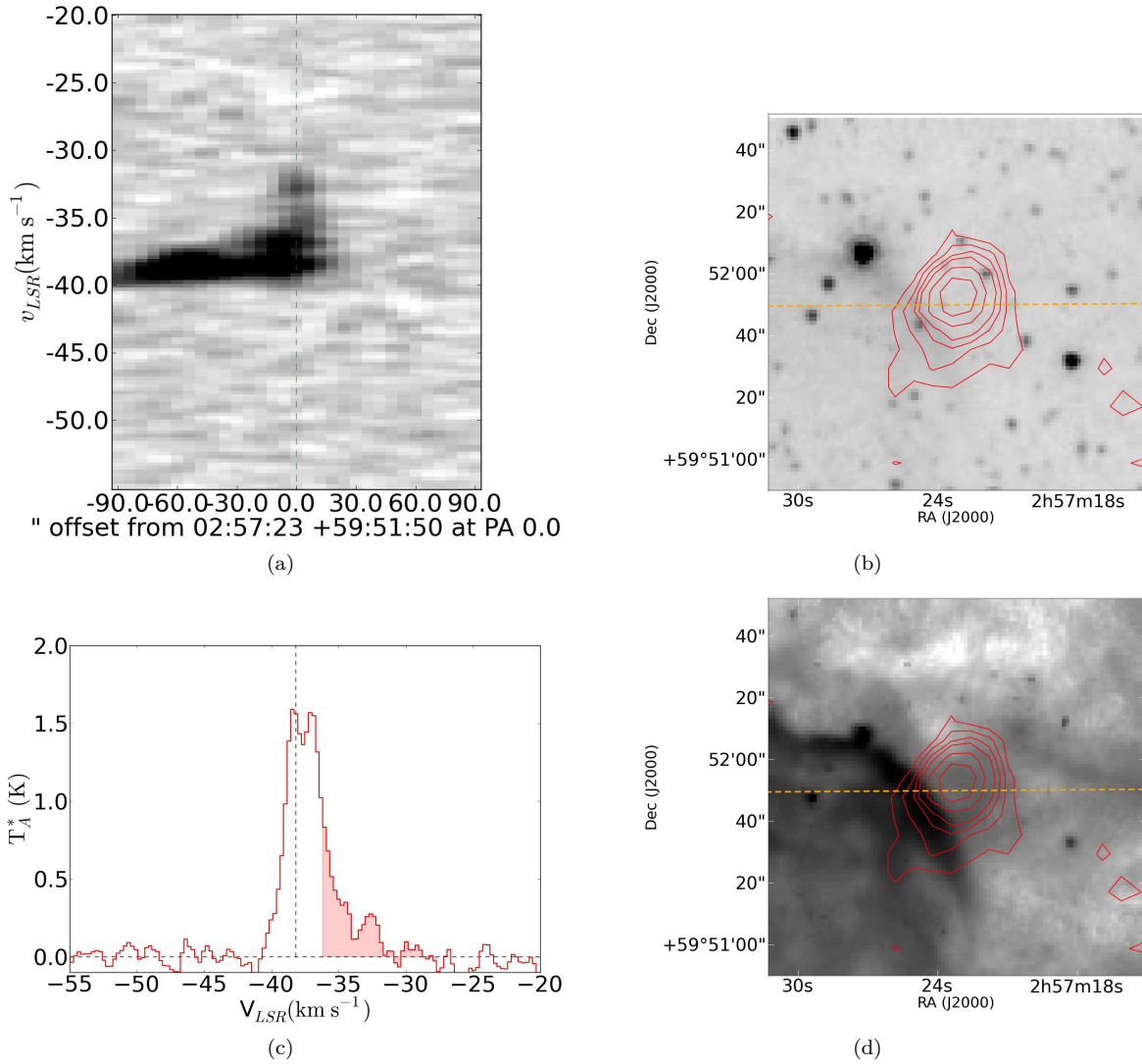


Figure 63. Position-velocity diagrams, spectra, and contour overlays of Outflow 40. The morphology of the high-velocity components in the PV diagram appear to be independent clouds, but the coincidence of three independent clouds along the same line of sight is somewhat unlikely, so we believe it is a reasonable outflow candidate. The lobes to the west are from Outflow 39.

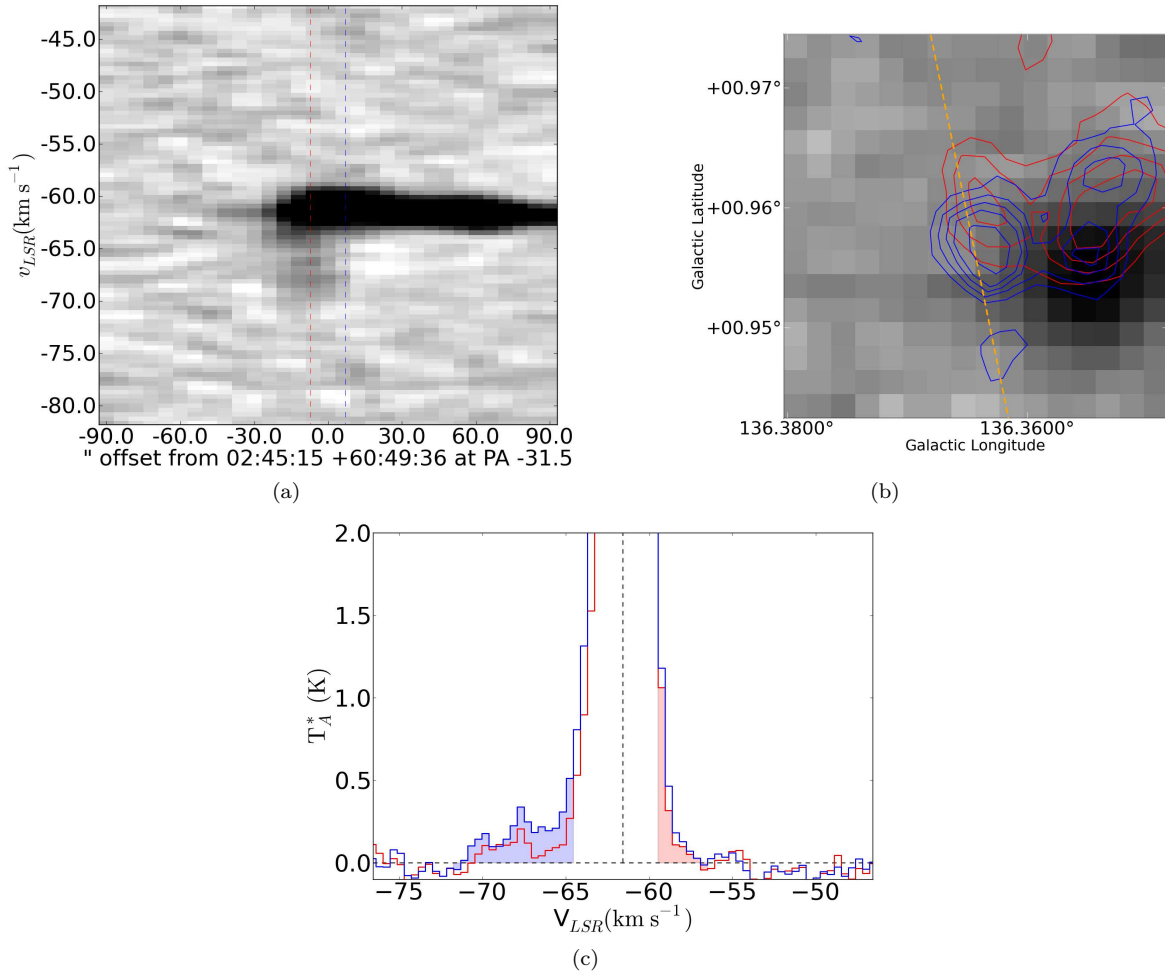


Figure 64. Position-velocity diagrams, spectra, and contour overlays of Outflow 41. Because the Spitzer survey of W5 did not extend to this region, the MSX band-A 8 μm map is used instead.

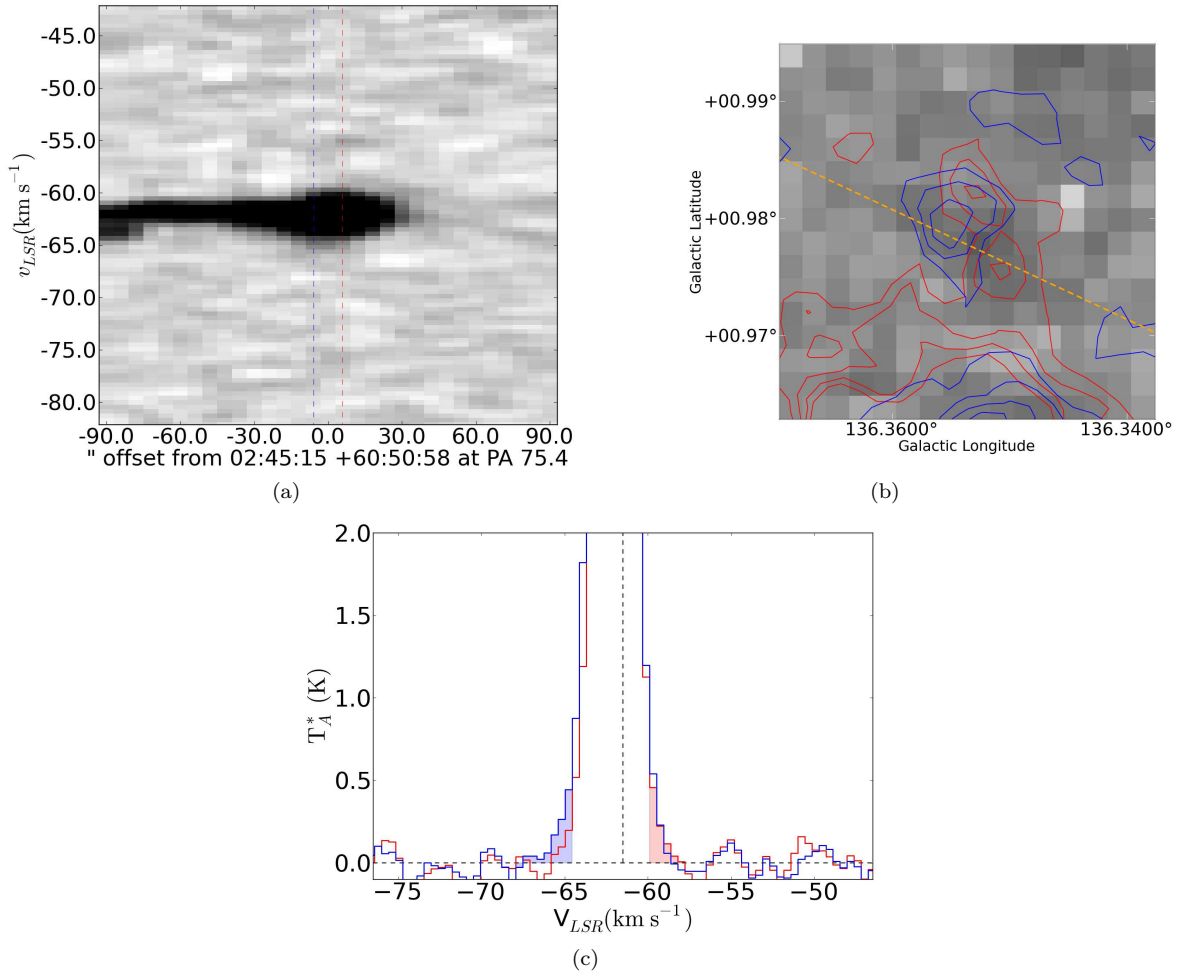


Figure 65. Position-velocity diagrams, spectra, and contour overlays of Outflow 42. It is not clear which of the two redshifted lobes is associated with the blueshifted flow. Contours are displayed at levels 0.25, 0.5, 0.75, 1 K km s $^{-1}$ (blue) and 0.25, 0.5, 0.75, 1 K km s $^{-1}$ (red). Because the Spitzer survey of W5 did not extend to this region, the MSX band-A 8 μ m map is used instead.

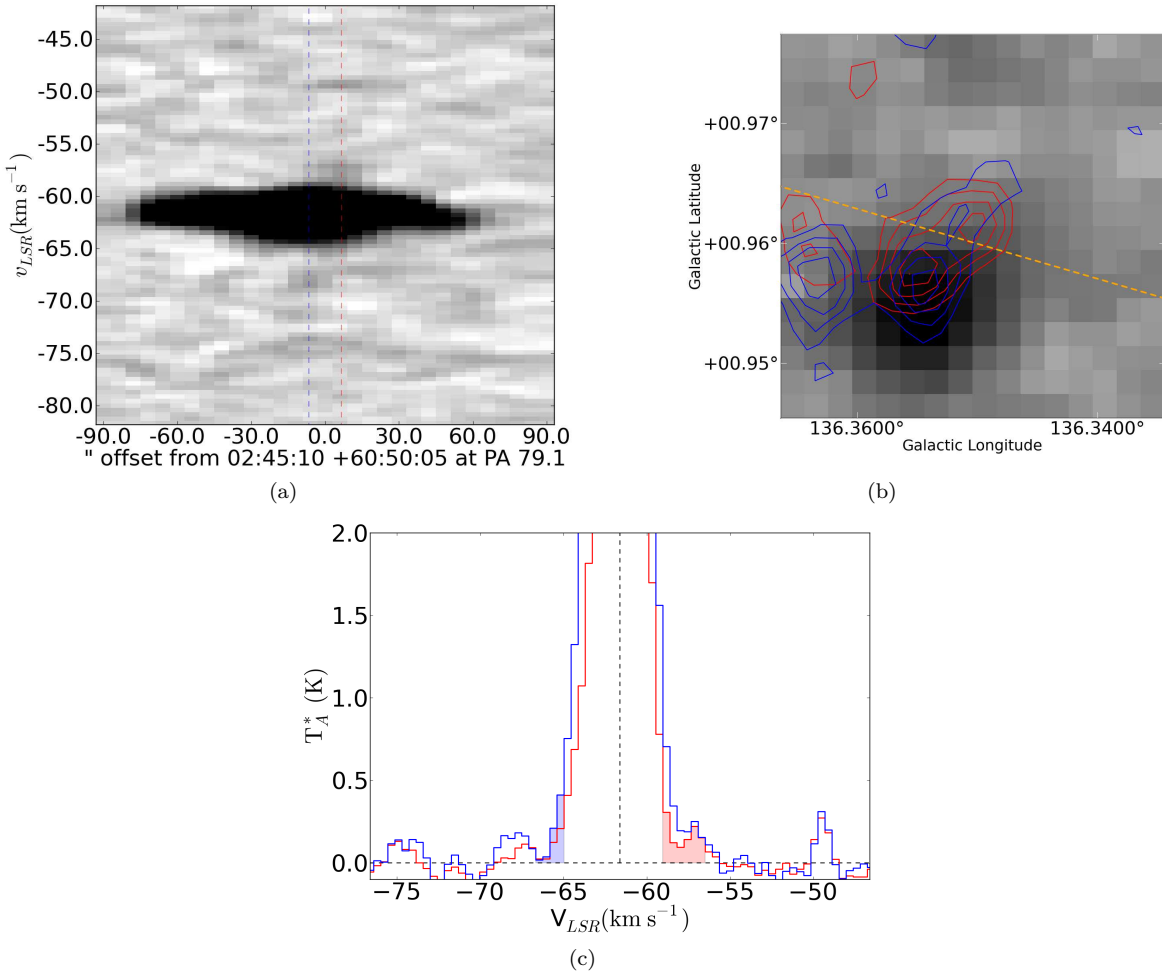


Figure 66. Position-velocity diagrams, spectra, and contour overlays of Outflow 43. Contours are displayed at levels 0.5, 0.75, 1, 1.25, 1.5, 2 K km s $^{-1}$ (blue) and 0.25, 0.5, 0.75, 1, 1.5, 2, 3, 4, 5, 6 K km s $^{-1}$ (red). Because the Spitzer survey of W5 did not extend to this region, the MSX band-A 8 μ m map is used instead.

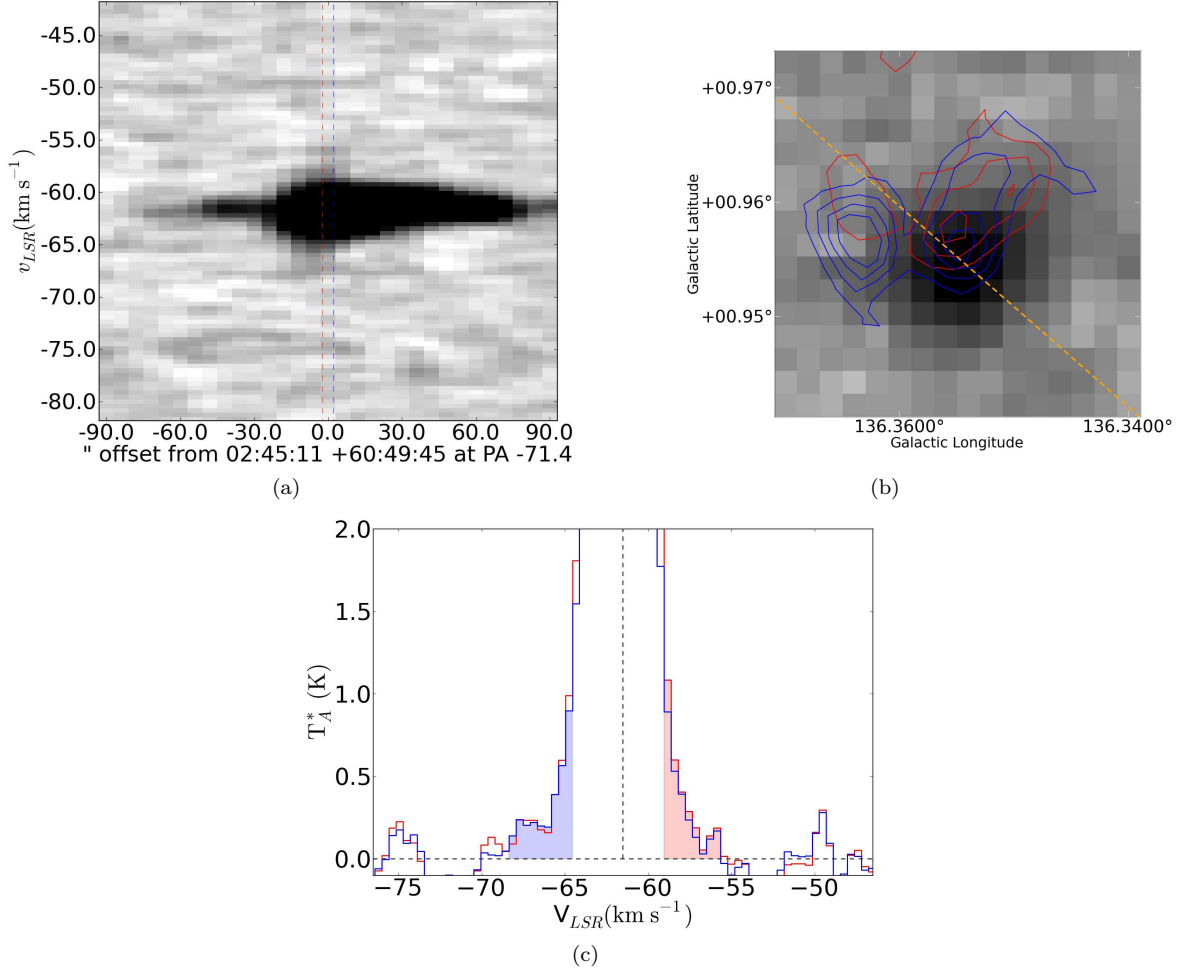


Figure 67. Position-velocity diagrams, spectra, and contour overlays of Outflow 44. Because the Spitzer survey of W5 did not extend to this region, the MSX band-A 8 μm map is used instead.

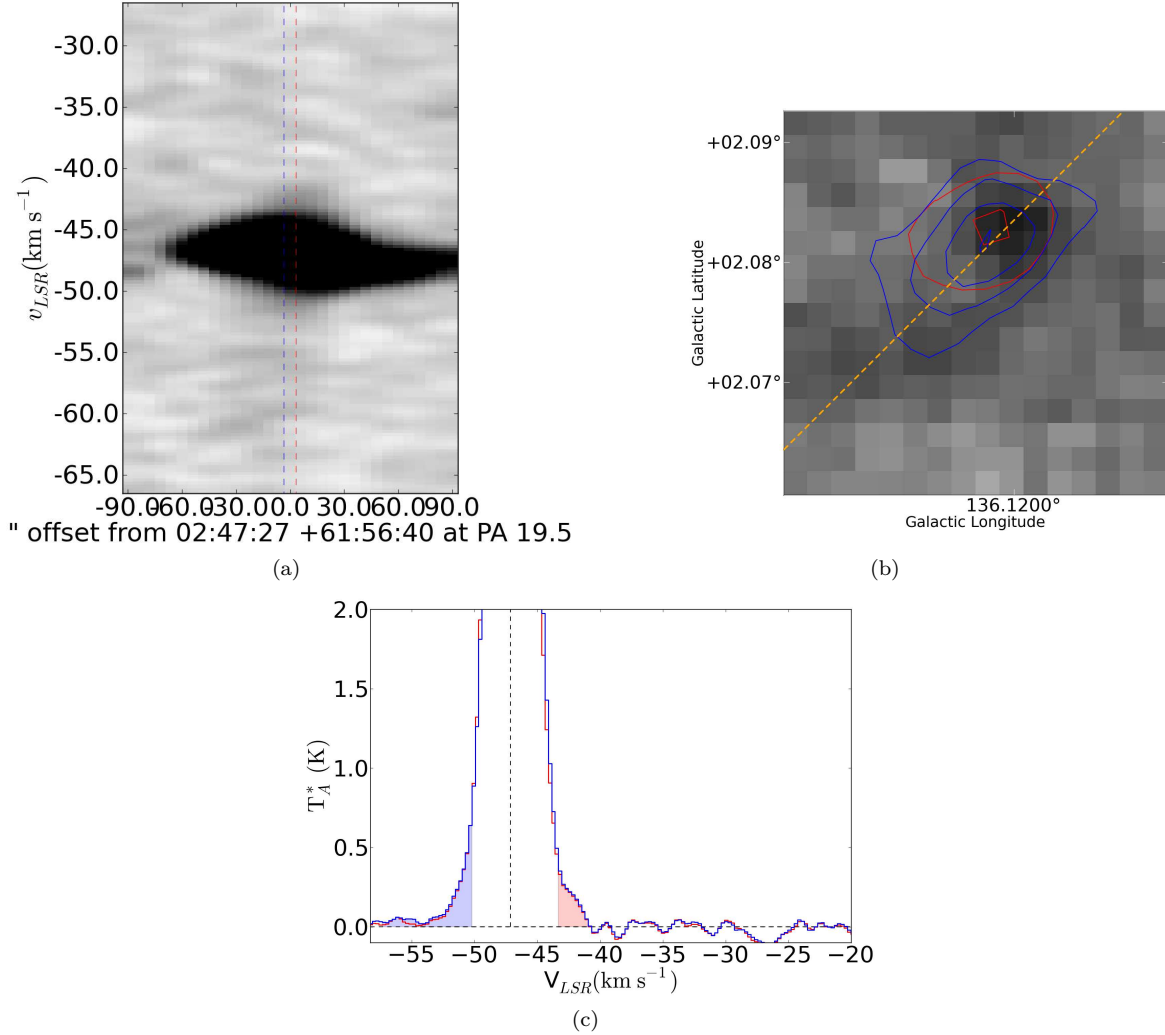


Figure 68. Position-velocity diagrams, spectra, and contour overlays of Outflow 45. Because the Spitzer survey of W5 did not extend to this region, the MSX band-A 8 μm map is used instead.

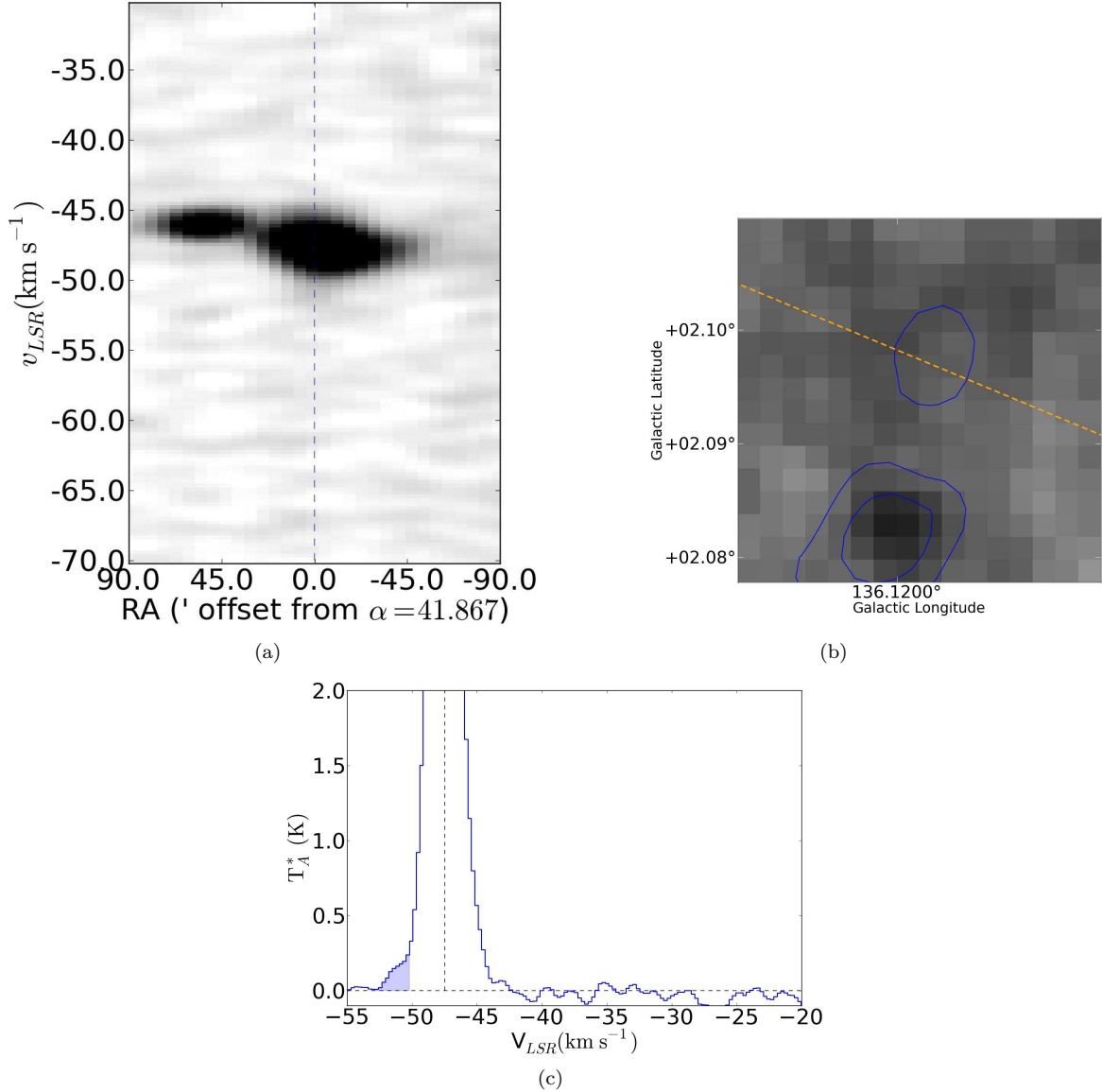


Figure 69. Position-velocity diagrams, spectra, and contour overlays of Outflow 46. Because the Spitzer survey of W5 did not extend to this region, the MSX band-A 8 μm map is used instead.

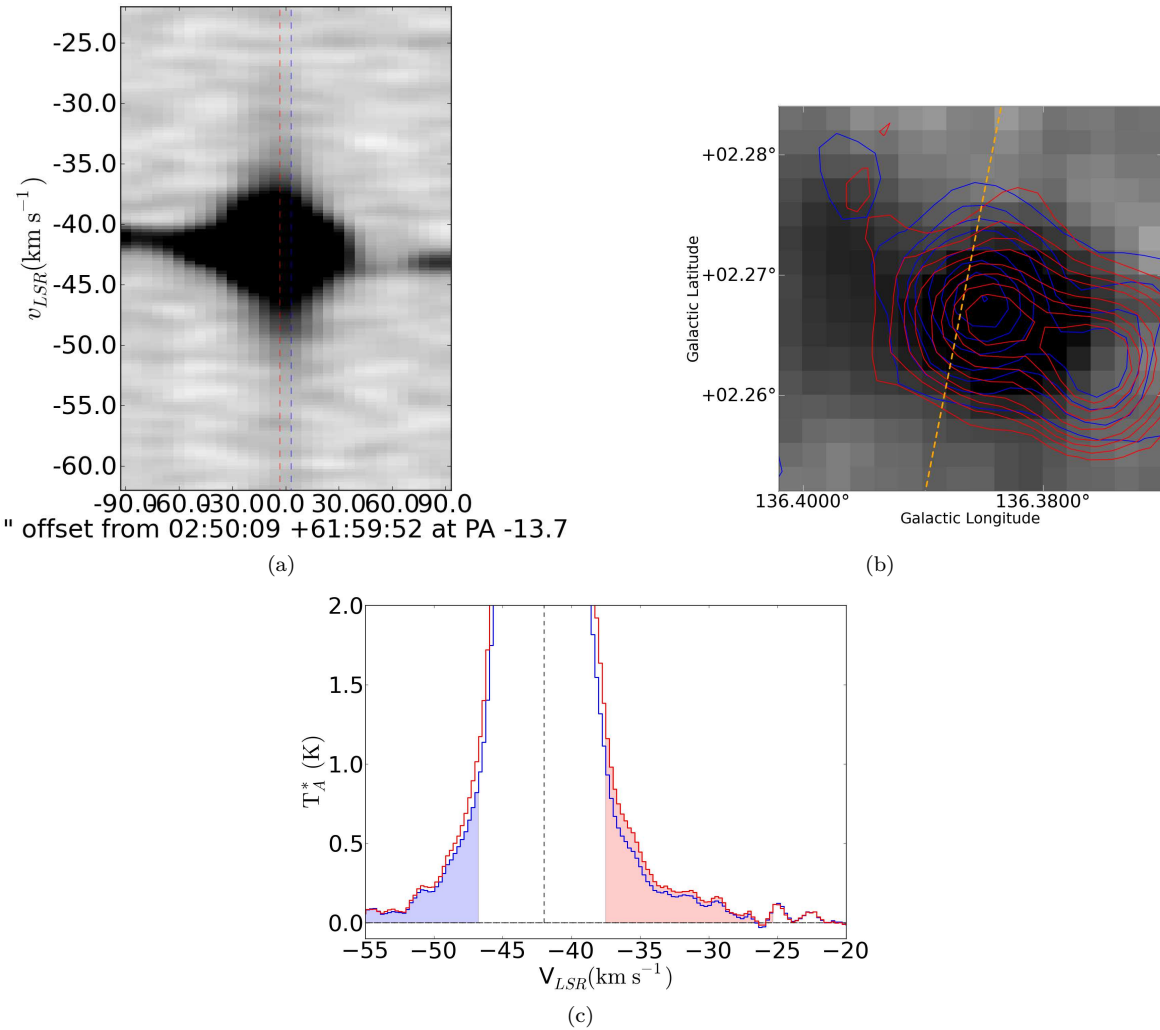


Figure 70. Position-velocity diagrams, spectra, and contour overlays of Outflow 47. Because the Spitzer survey of W5 did not extend to this region, the MSX band-A 8 μm map is used instead.

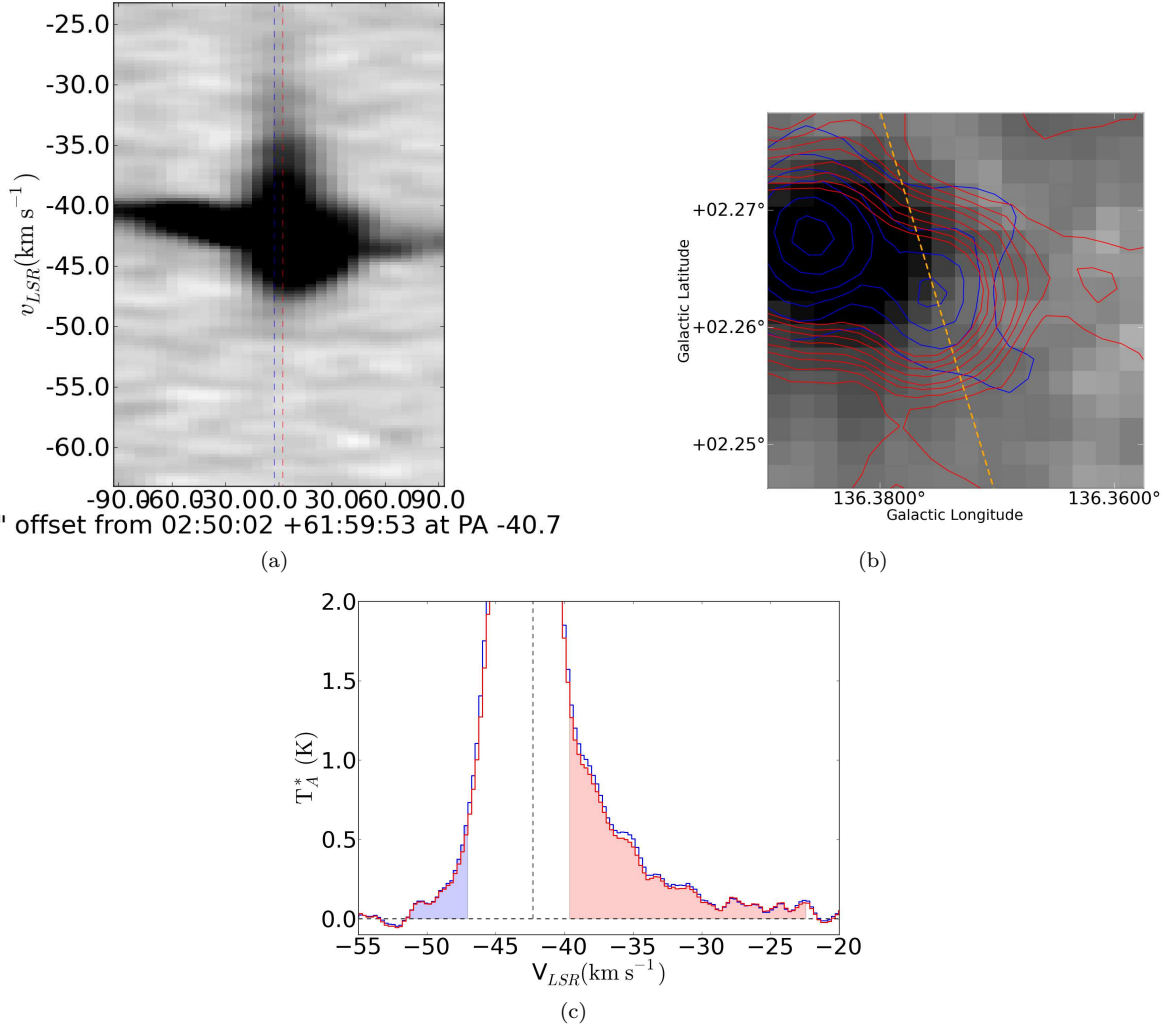


Figure 71. Position-velocity diagrams, spectra, and contour overlays of Outflow 48. Because the Spitzer survey of W5 did not extend to this region, the MSX band-A 8 μm map is used instead.

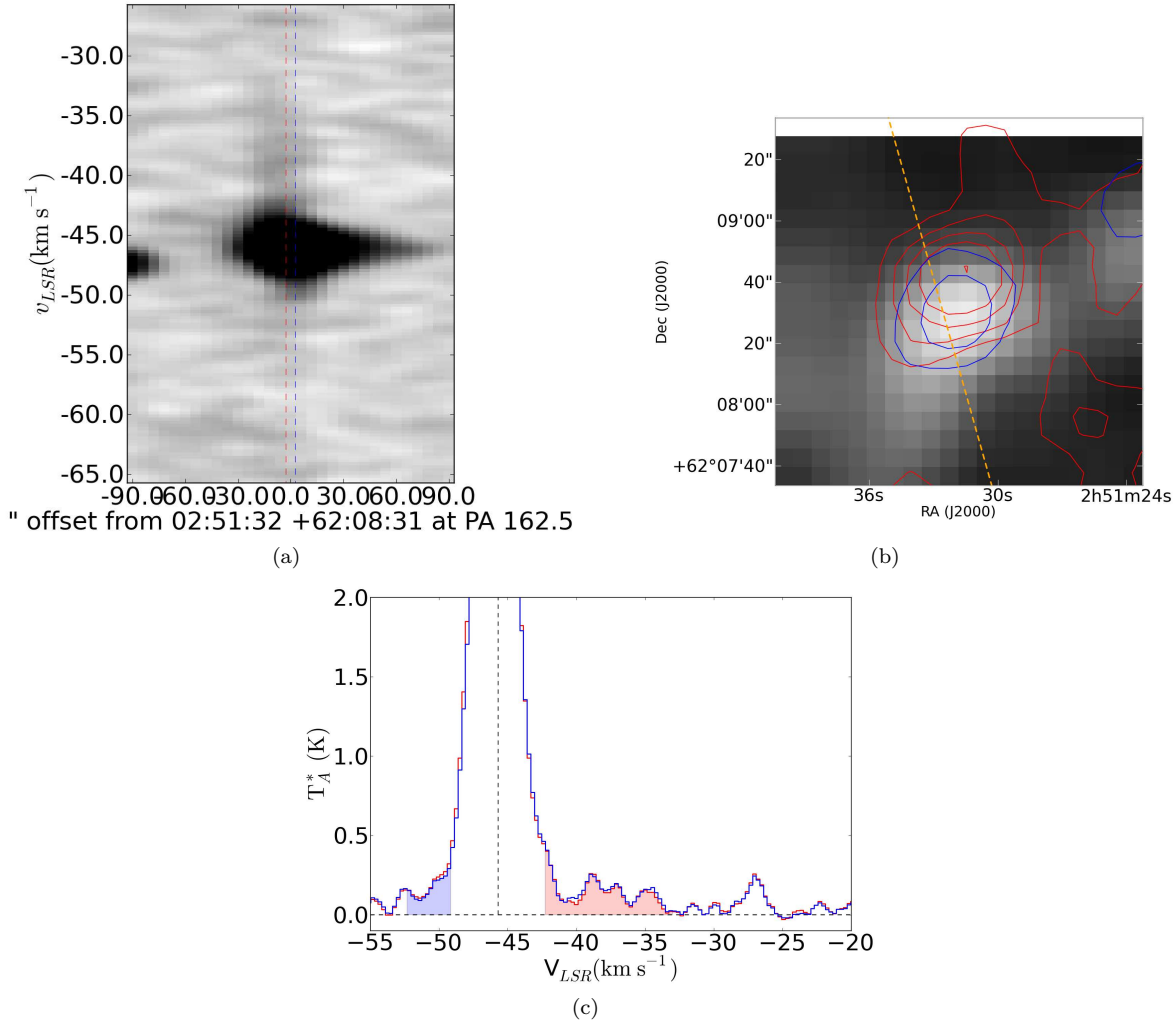


Figure 72. Position-velocity diagrams, spectra, and contour overlays of Outflow 49. Because the Spitzer survey of W5 did not extend to this region, and the MSX survey also did not extend this far, the CO 3-2 integrated map is used as the background.

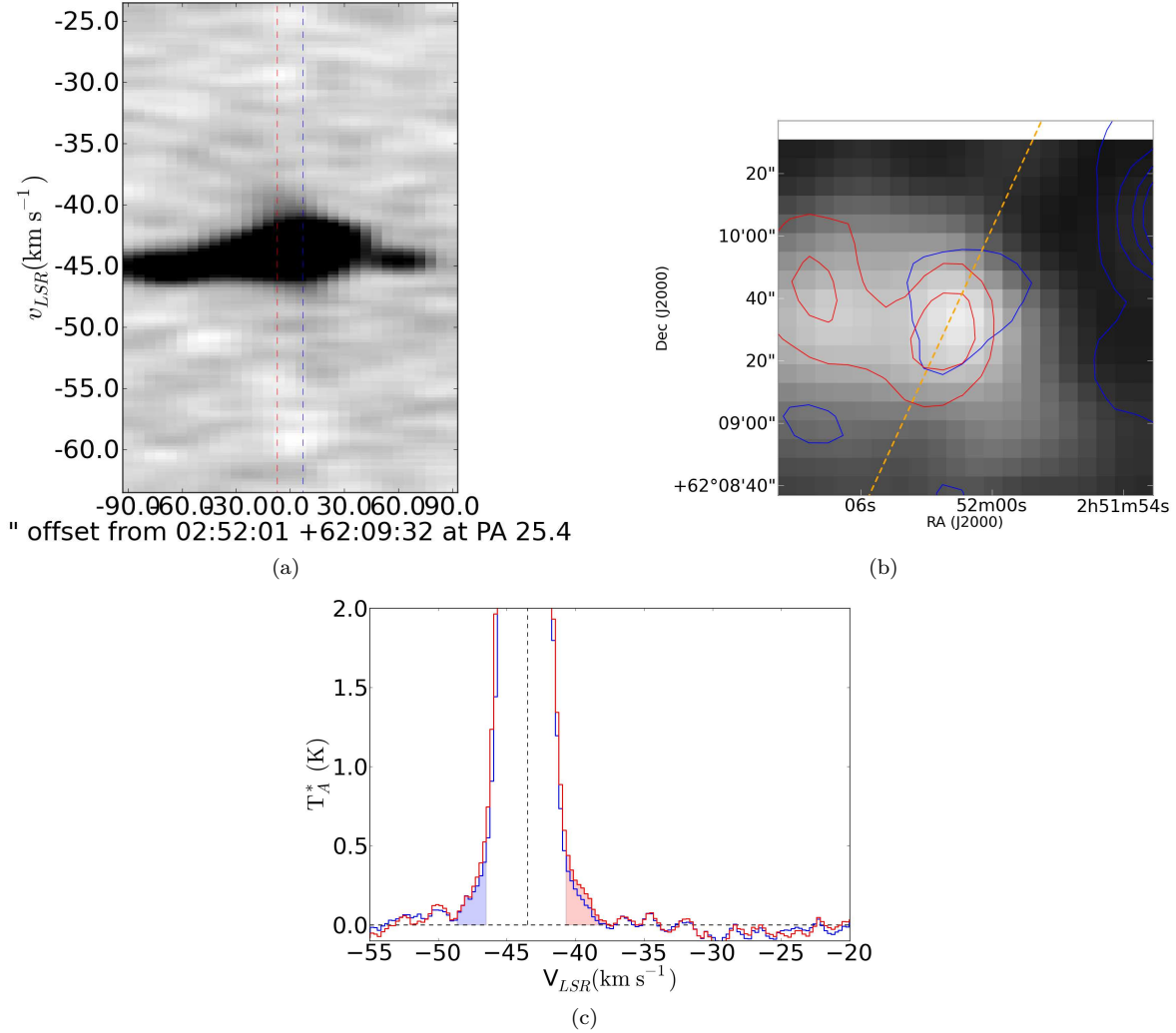


Figure 73. Position-velocity diagrams, spectra, and contour overlays of Outflow 50. Because the Spitzer survey of W5 did not extend to this region, and the MSX survey also did not extend this far, the CO 3-2 integrated map is used as the background.

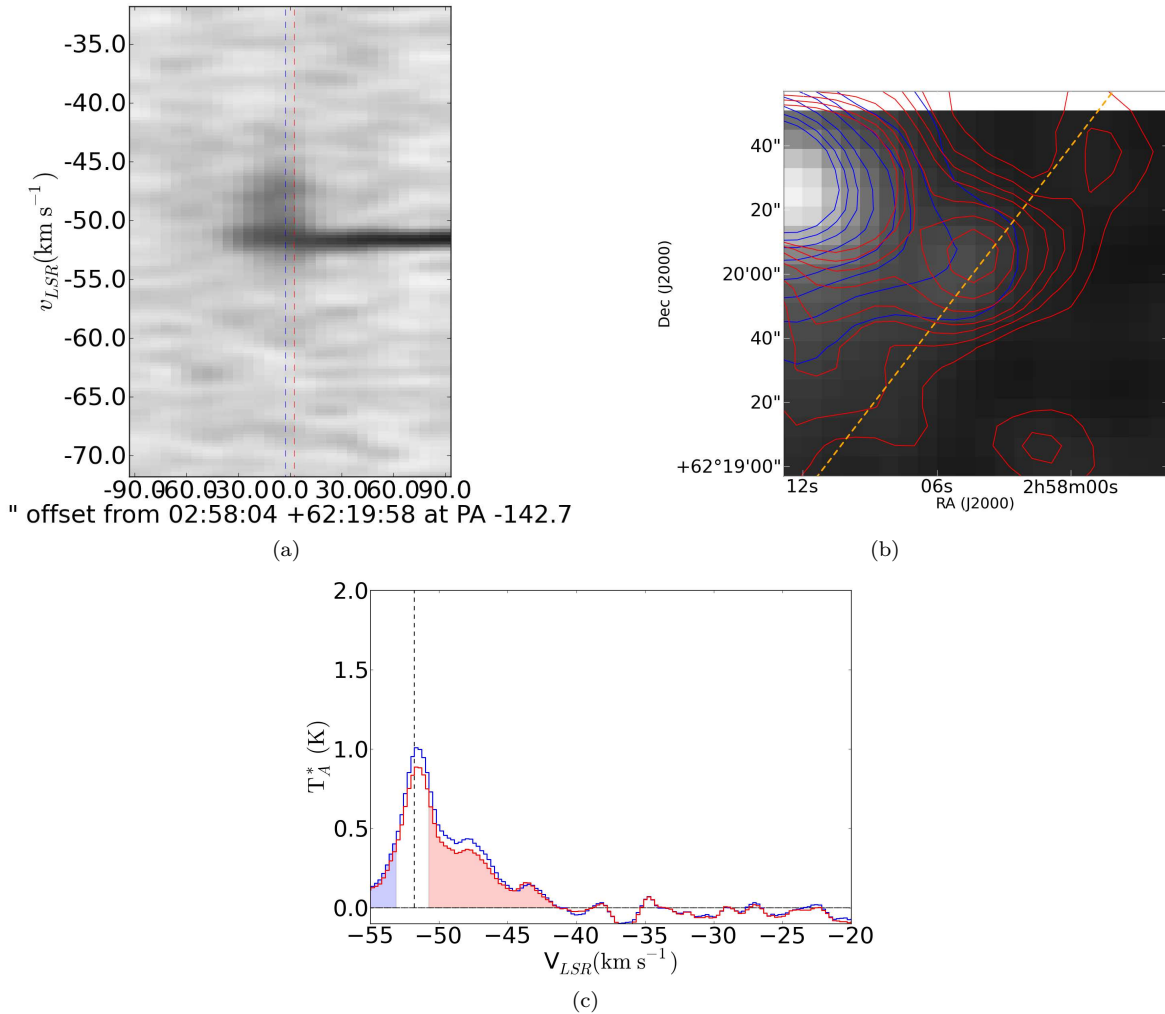


Figure 74. Position-velocity diagrams, spectra, and contour overlays of Outflow 51. Because the Spitzer survey of W5 did not extend to this region, and the MSX survey also did not extend this far, the CO 3-2 integrated map is used as the background.

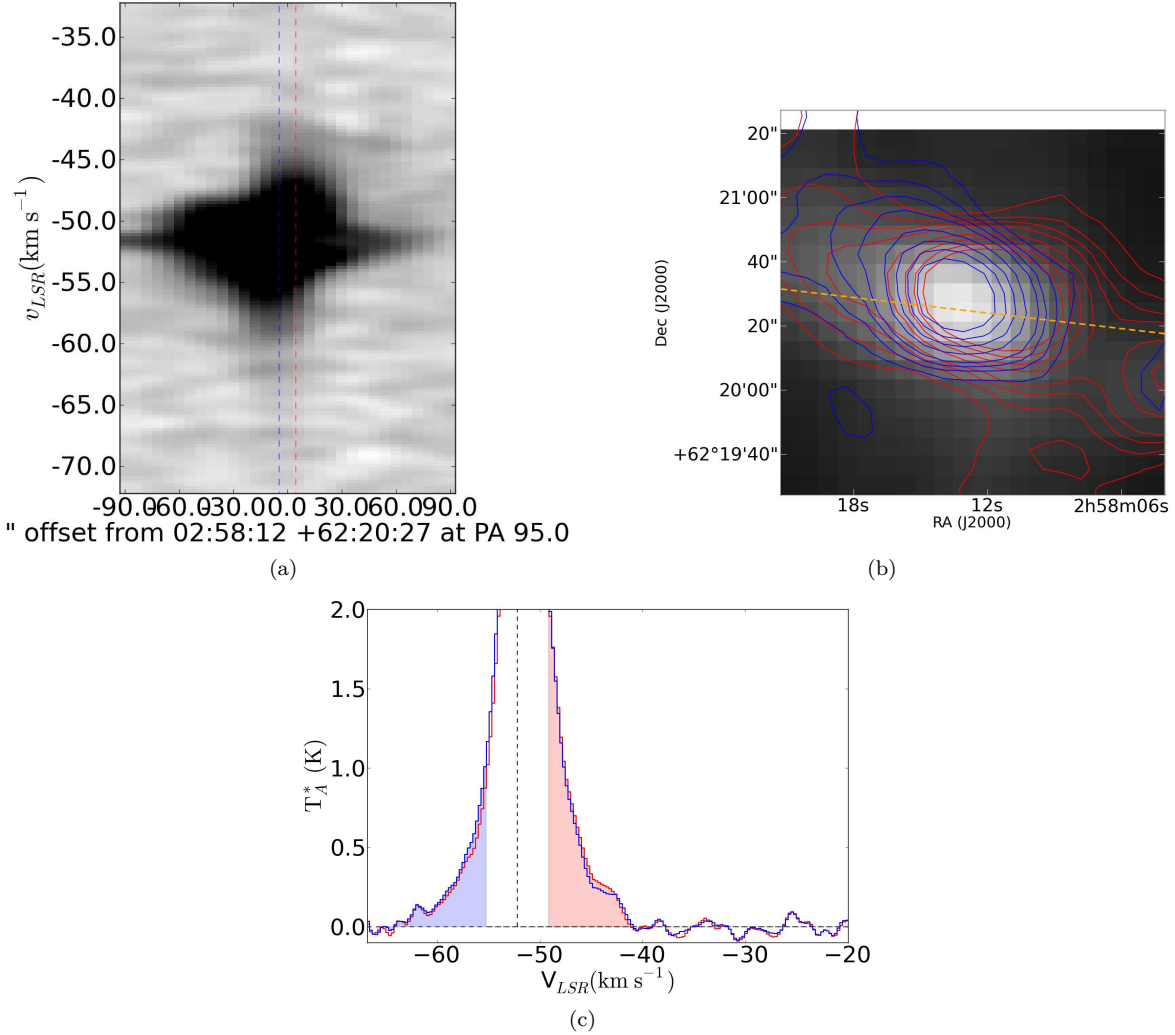


Figure 75. Position-velocity diagrams, spectra, and contour overlays of Outflow 52. Because the Spitzer survey of W5 did not extend to this region, and the MSX survey also did not extend this far, the CO 3-2 integrated map is used as the background.

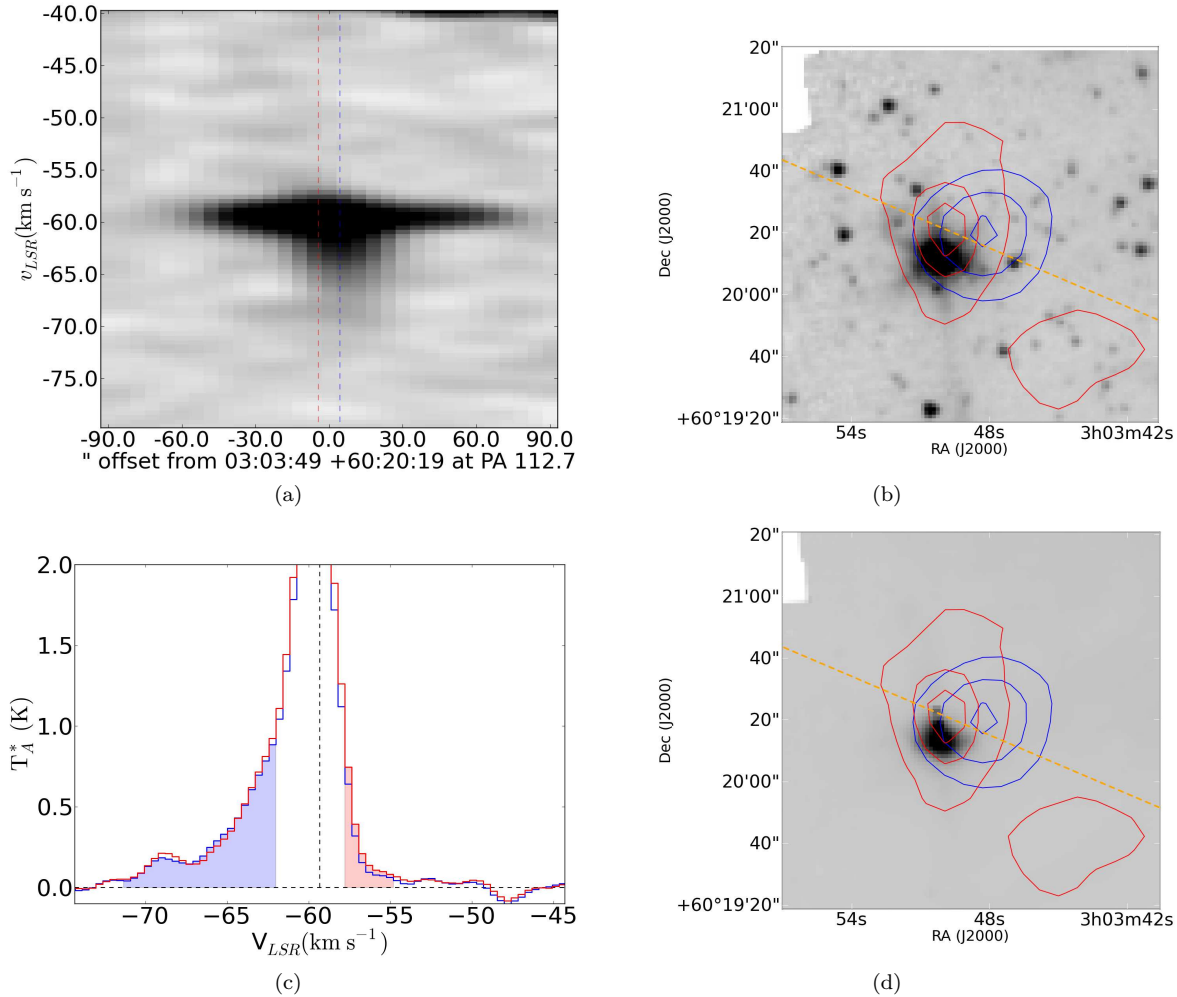


Figure 76. Position-velocity diagrams, spectra, and contour overlays of Outflow 53. Contours are displayed at levels $2, 4, 6 \text{ K km s}^{-1}$ (blue) and $0.5, 1, 1.25 \text{ K km s}^{-1}$ (red).

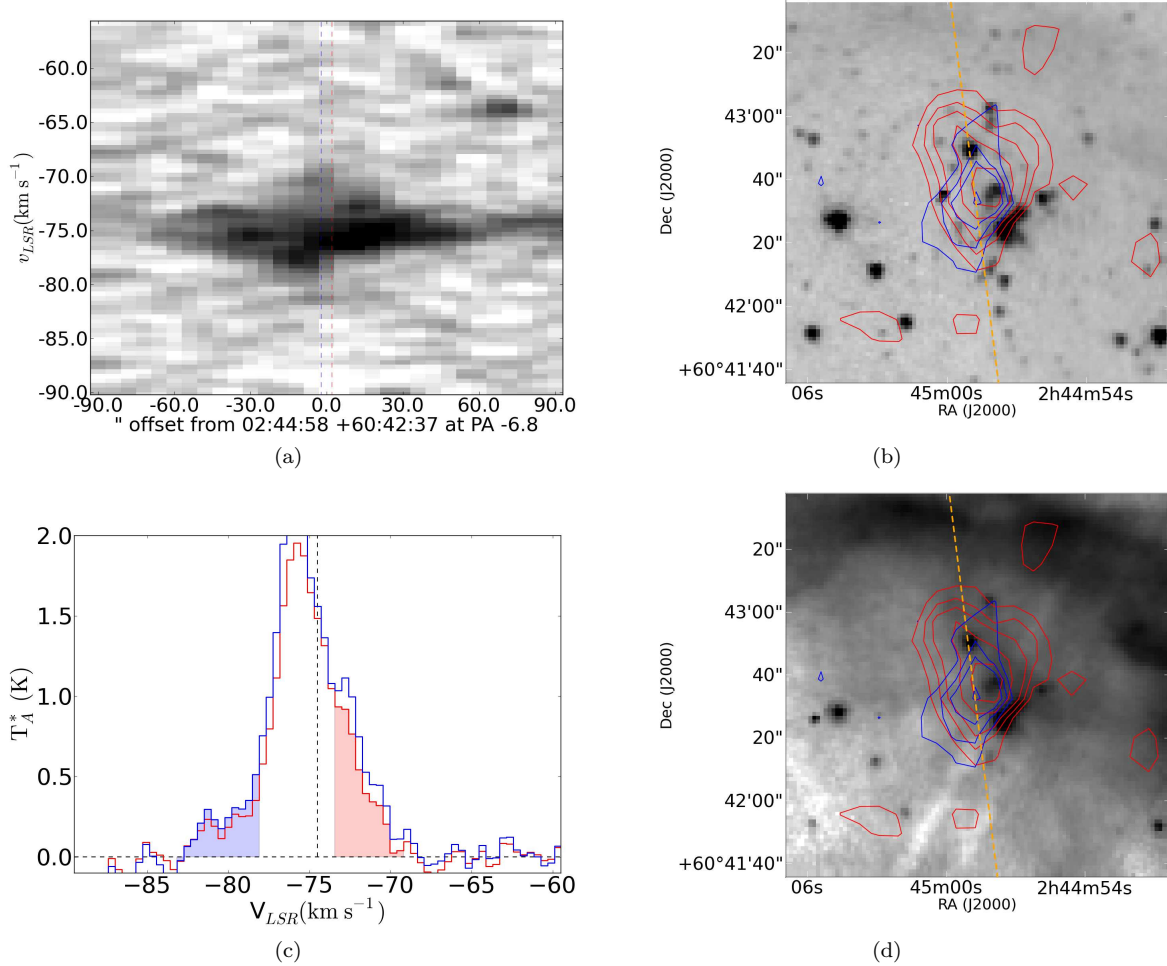


Figure 77. Position-velocity diagrams, spectra, and contour overlays of Outflow 54. Contours are displayed at levels $1, 1.5, 2, 3, 4, 5, 6 \text{ km s}^{-1}$ (blue) and $1, 1.5, 2, 3, 4, 5, 6 \text{ K km s}^{-1}$ (red).

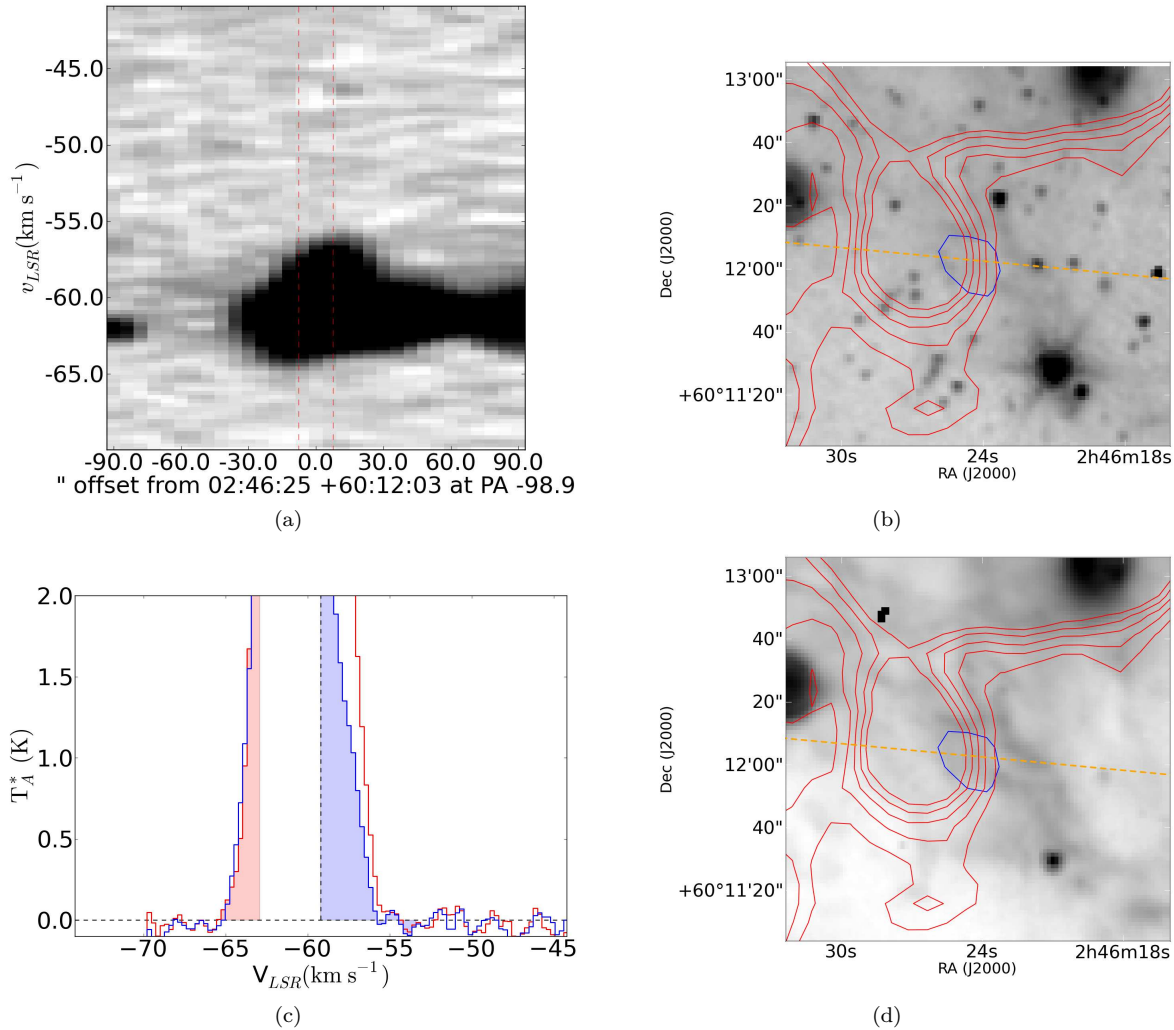


Figure 78. Position-velocity diagrams, spectra, and contour overlays of Outflow 55. Contours are displayed at levels 4,6,8,10,12 K km s $^{-1}$ (blue) and 2,3,4,5,6 K km s $^{-1}$ (red).

APPENDIX A: OPTICALLY THIN, LTE DIPOLE MOLECULE

While many authors have solved the problem of converting CO 1-0 beam temperatures to H₂ column densities (Garden et al. 1991; Bourke et al. 1997; Cabrit & Bertout 1990; Lada & Fich 1996), there are no examples in the literature of a full derivation of the LTE, optically thin CO-to-H₂ conversion process for higher rotational states. We present the full derivation here, and quantify the systematic errors generated by various assumptions.

We begin with the assumption of an optically thin cloud such that the radiative transfer equation (Wilson et al. 2009, eqn 1.9) simplifies to

$$\frac{dI_\nu}{ds} = -\kappa_\nu I_\nu \quad (\text{A1})$$

The absorption and stimulated emission terms yield

$$\kappa_\nu = \frac{h\nu_{ul}B_{ul}n_u}{c}\varphi(\nu) - \frac{h\nu_{ul}B_{lu}n_l}{c}\varphi(\nu) \quad (\text{A2})$$

where $\varphi(\nu)$ is the line shape function ($\int \varphi(\nu)d\nu \equiv 1$), n is the density in the given state, ν is the frequency of the transition, B is the Einstein B coefficient, and h is Planck's constant.

By assuming LTE (the Boltzmann distribution) and using Kirchoff's Law and the definition of the Einstein A and B values, we can derive a more useful version of this equation

$$\kappa_\nu = \frac{c^2}{8\pi\nu_{ul}^2}n_uA_{ul}\left[\exp\left(\frac{h\nu_{ul}}{k_BT_{ex}}\right) - 1\right]\varphi(\nu) \quad (\text{A3})$$

where k_B is Boltzmann's constant.

The observable T_B can be related to the optical depth, which is given by

$$\int \tau_\nu d\nu = \frac{c^2}{8\pi\nu_{ul}^2}A_{ul}\left[\exp\left(\frac{h\nu_{ul}}{k_BT_{ex}}\right) - 1\right] \int \varphi(\nu)d\nu \int n_u ds \quad (\text{A4})$$

Rearranging and converting from density to column ($\int nds = N$) gives an equation for the column density of the molecule in the upper energy state of the transition:

$$N_u = \frac{8\pi\nu_{ul}^2}{c^2A_{ul}}\left[\exp\left(\frac{h\nu_{ul}}{k_BT_{ex}}\right) - 1\right]^{-1} \int \tau_\nu d\nu \quad (\text{A5})$$

In order to relate the brightness temperature to the optical depth, at CO transition frequencies the full blackbody formula must be used and the CMB must also be taken into account. Wilson et al. (2009) equation 15.29

$$T_B(\nu) = \frac{h\nu}{k_B}\left(\left[e^{h\nu/k_BT_{ex}} - 1\right]^{-1} - \left[e^{h\nu/k_BT_{CMB}} - 1\right]^{-1}\right)(1 - e^{-\tau_\nu}) \quad (\text{A6})$$

is rearranged to solve for τ_ν :

$$\tau_\nu = -\ln\left[1 - \frac{k_BT_B}{h\nu}\left(\left[e^{h\nu/k_BT_{ex}} - 1\right]^{-1} - \left[e^{h\nu/k_BT_{CMB}} - 1\right]^{-1}\right)^{-1}\right] \quad (\text{A7})$$

We convert from frequency to velocity units with $d\nu = \nu/cdv$, and plug (A7) into (A5) to get

$$N_u = \frac{8\pi\nu_{ul}^3}{c^3A_{ul}}\left[\exp\left(\frac{h\nu_{ul}}{k_BT_{ex}}\right) - 1\right]^{-1} \int -\ln\left[1 - \frac{k_BT_B}{h\nu_{ul}}\left(\left[e^{h\nu_{ul}/k_BT_{ex}} - 1\right]^{-1} - \left[e^{h\nu_{ul}/k_BT_{CMB}} - 1\right]^{-1}\right)^{-1}\right] dv \quad (\text{A8})$$

which is the full LTE upper-level column density with no approximations applied.

The first term of the Taylor expansion is appropriate for $\tau << 1$ ($\ln[1+x] \approx x - \frac{x^2}{2} + \frac{x^3}{3} \dots$)

$$N_u = \frac{8\pi\nu_{ul}^3}{c^3A_{ul}}\left[\exp\left(\frac{h\nu_{ul}}{k_BT_{ex}}\right) - 1\right]^{-1} \int \frac{k_BT_B}{h\nu_{ul}}\left(\left[e^{h\nu_{ul}/k_BT_{ex}} - 1\right]^{-1} - \left[e^{h\nu_{ul}/k_BT_{CMB}} - 1\right]^{-1}\right)^{-1} dv \quad (\text{A9})$$

which simplifies to

$$N_u = \frac{8\pi\nu_{ul}^2 k_B}{c^3 A_{ul} h} \frac{e^{h\nu_{ul}/k_BT_{CMB}} - 1}{e^{h\nu_{ul}/k_BT_{CMB}} - e^{h\nu_{ul}/k_BT_{ex}}} \int T_B dv \quad (\text{A10})$$

This can be converted to use μ_e (0.1222 for ¹²CO; Muenter 1975), the electric dipole moment of the molecule, instead of A_{ul} , using Wilson et al. (2009) equation 15.20 ($(A_{ul} = (64\pi^4)/(3hc^3))\nu^3\mu_e^2$):

$$N_u = \frac{3}{8\pi^3\mu_e^2} \frac{k_B}{\nu_{ul}} \frac{2J_u + 1}{J_u} \frac{e^{h\nu_{ul}/k_BT_{CMB}} - 1}{e^{h\nu_{ul}/k_BT_{CMB}} - e^{h\nu_{ul}/k_BT_{ex}}} \int T_B dv \quad (\text{A11})$$

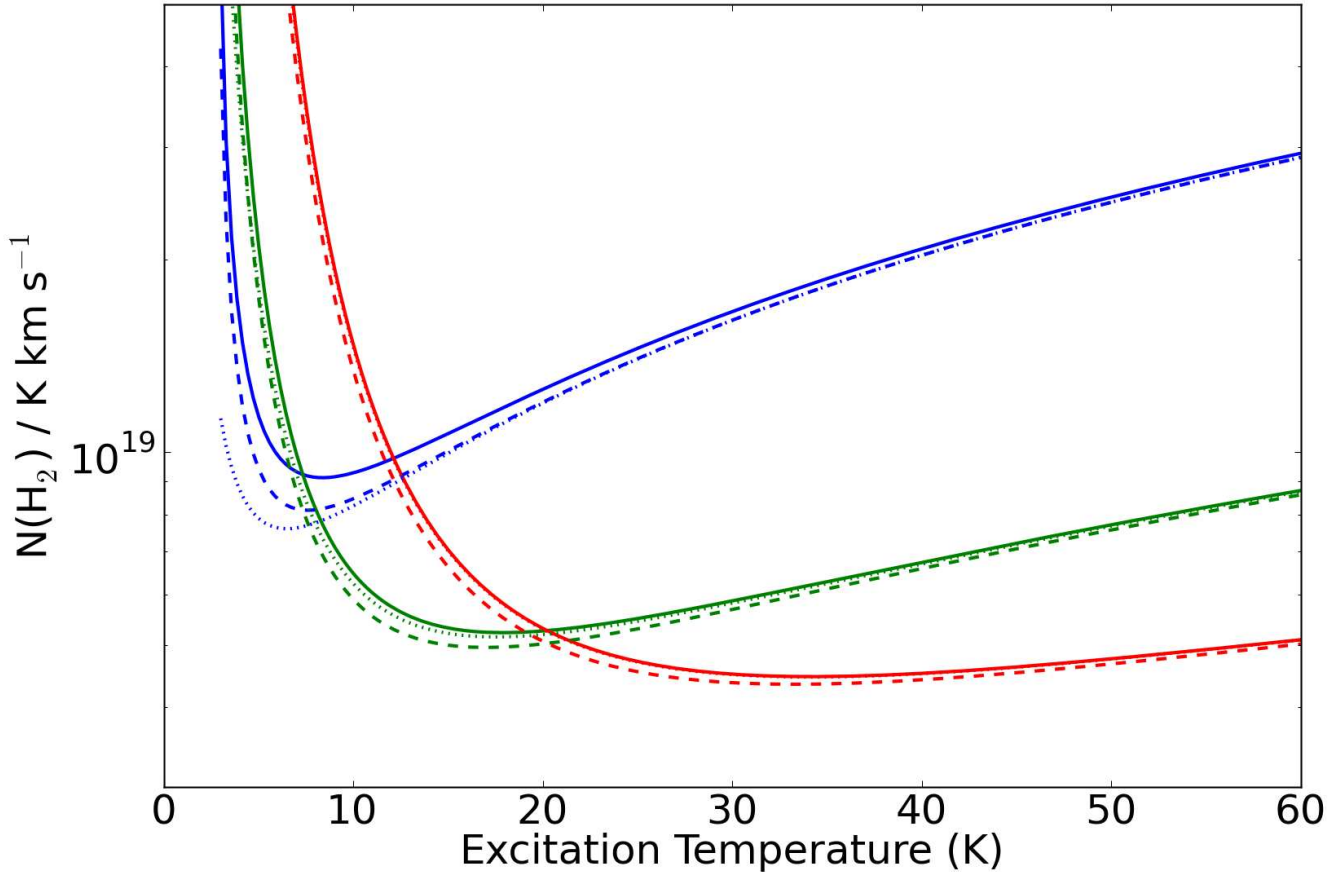


Figure A1. The LTE, optically thin conversion factor from T_B (K km s $^{-1}$) to $N(\text{H}_2)$ (cm $^{-2}$) assuming $X_{12\text{CO}} = 10^{-4}$ plotted against T_{ex} . The dashed line shows the effect of using the integral approximation of the partition function (e.g. Cabrit & Bertout 1990). It is a better approximation away from the critical point, and is a better approximation for higher transitions. The dotted line shows the effects of removing the CMB term from (A6); the CMB populates the lowest two excited states, but contributes nearly nothing to the $J = 3$ state. Top (blue): $J=1-0$, Middle (green): $J=2-1$, Bottom (red): $J=3-2$.

The total column can be derived from the column in the upper state using the partition function and the Boltzmann distribution

$$n_{tot} = \sum_{J=0}^{\infty} n_J = n_0 \sum_{J=0}^{\infty} (2J+1) \exp\left(-\frac{J(J+1)B_e h}{k_B T_{ex}}\right) \quad (\text{A12})$$

(A13)

This equation is frequently approximated using an integral (e.g. Cabrit & Bertout 1990), but a more accurate numerical solution using up to thousands of rotational states is easily computed

$$n_J = \left[\sum_{j=0}^{j_{max}} (2j+1) \exp\left(-\frac{j(j+1)B_e h}{k_B T_{ex}}\right) \right]^{-1} (2J+1) \exp\left(-\frac{J(J+1)B_e h}{k_B T_{ex}}\right) \quad (\text{A14})$$

The effects of using the approximation and the full numerical solution are shown in figure A1.

The CO 3-2 transition is also less likely to be in LTE than the 1-0 transition. The critical density ($n_{cr} \equiv A_{ul}/C_{ul}$) of ^{12}CO 3-2 is 27 times higher than that for 1-0. We have run RADEX (van der Tak et al. 2007) LVG models of CO to examine the impact of sub-thermal excitation on column derivation. The results of the RADEX models are shown in Figure A2. They illustrate that, while it is quite safe to assume the CO 1-0 transition is in LTE in most circumstances, a similar assumption is probably invalid for the CO 3-2 transition in typical molecular cloud environments.

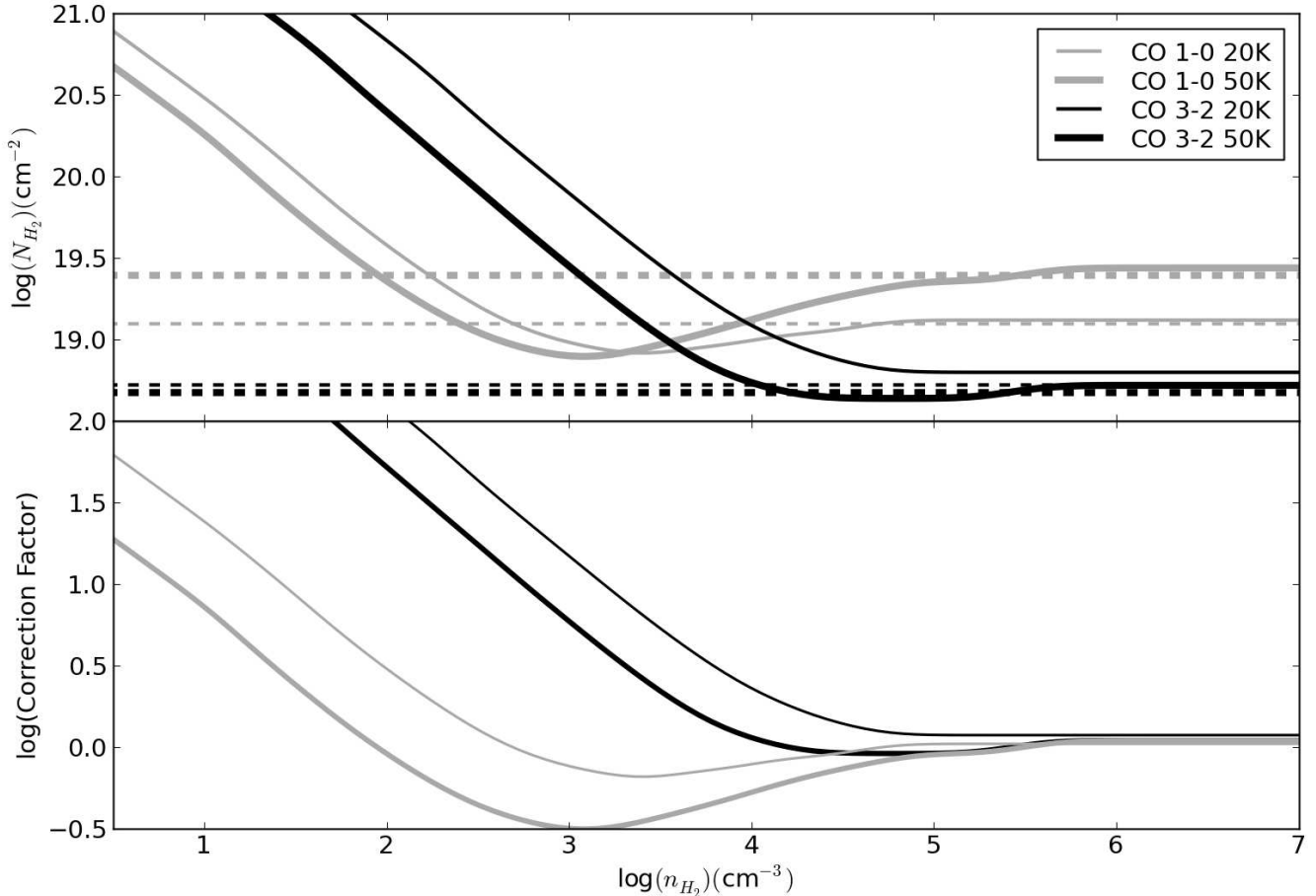


Figure A2. Top: The derived $N(H_2)$ as a function of n_{H_2} for $T_B = 1$ K. The dashed lines represent the LTE-derived $N(H_2)/T_B$ factor, which has no density dependence and, for CO 3-2, only a weak dependence on temperature. We assume an abundance of ^{12}CO relative to H_2 $X_{CO} = 10^{-4}$. Bottom: The correction factor ($N(H_2)_{RADEX} / N(H_2)_{LTE}$) as a function of n_{H_2} . For $T_K = 20$ K, the “correction factor” at 10^3 cm^{-3} (typical GMC mean volume densities) is ~ 15 , while at 10^4 cm^{-3} (closer to n_{crit} but perhaps substantially higher than GMC densities) it becomes negligible. The correction factor is also systematically lower for a higher gas kinetic temperature. For some densities, the “correction factor” dips below 1, particularly for CO 1-0. This effect is from a slight population inversion due to fast spontaneous decay rates from the higher levels and has been noted before (e.g. Goldsmith 1972).